Robust Controller Design for a Hybrid-Electric Marine Propulsion Plant

Konstantinos Bardis

Diploma Thesis

School of Naval Architecture and Marine Engineering
National Technical University of Athens

Thesis Supervisor: Assistant Professor G. Papalambrou
Committee Member: Professor N. Kyrtatos
Committee Member: Professor K. Kyriakopoulos

November 2015

Acknowledgements

This work has been carried out at the Laboratory of Marine Engineering (LME) at the School of Naval Architecture and Marine Engineering of the National Technical University of Athens, under the supervision of Assistant Professor George Papalambrou.

I would like to thank Professor Nikolaos Kyrtatos for providing the opportunity to work with the full-scale marine propulsion engine of LME. Being able to access the LME test bed facilities crucially contributed to examine theoretical concepts from a practical-engineering perspective and evaluate experimentally the designed control system.

I owe my greatest appreciation to my supervisor Assistant Professor George Papalambrou for giving me the chance to work on this thesis. In addition to his constant guidance, valuable comments and fruitful discussions, I have to thank him for his unceasing encouragement and support through this thesis.

I am deeply grateful to the PhD student Sotirios Topaloglou for handling the whole experimental setup of the CAT marine diesel engine test bench. His practical insights and our excellent collaboration was really precious during the experimental testing and validation of the virtual sensor model and the robust controller.

I would also like to thank Professor Konstantinos Kyriakopoulos for being a member of my supervisors committee.

I am also grateful to my family for their constant encouragement throughout my thesis.

Abstract

The main purpose of this thesis is the design of a robust controller for a hybrid-electric marine propulsion plant in order to reduce the main pollutant emissions of the internal combustion engine (ICE) during load transients. Precisely, the controlled physical variable is the value of lambda-λ of the exhaust gas produced by the ICE and the system's input is the command that is fed to the frequency inverter of the electric motor (EM) which manipulates the torque output of the EM. The type of robust controller chosen for the implementation was the μ-controller, mainly for its convenience in the modelling of uncertainty elements. The soundness of the modelling and of the developed controllers is evaluated in the experimental facilities of the Laboratory of Marine Engineering (LME).

Initially, a virtual λ-sensor was developed as an effective way to replace the measurements from the physical sensor installed in the exhaust duct of the ICE. The virtual sensor was tested on-line and the estimated values of λ were compared to the measured values of the physical sensor under both steady state and transient operation of the ICE. It should be noted that a phenomenological approach was adopted in the model derivation of the virtual sensor.

Furthermore, the non-linear dynamic uncertain model was derived using a mean value approach in order to simulate the value of λ during transient engine operation. The fundamental objective was to obtain a model of λ depending only on known physical variables of the hybrid-electric power-train. The model developed has to sufficiently capture the transient phenomena but, simultaneously, be as simple as possible in order to be suitable for the control application. For this reason, various simplifications were made and their validity were evaluated mostly from an engineering perspective.

A linear model was obtained, for control purposes, from the original non-linear uncertain plant at a certain operating point of the engine. For this reason, all the physical variables of the operating point, which are at steady state, were computed as a function of the known input variables; namely, the requested torque and the rotational speed of the engine. The non-linear algebraic constraint equations along with certain differential equations were also useful in deriving a second virtual sensor model which made use only of the turbocharger speed in order to estimate λ; thus, provides a promising and low cost solution for practical marine applications.

Furthermore, a low order λ-model of the internal combustion was obtained through singular perturbations order reduction technique. The model was linearised and, eventually, a first order transfer function connecting the fuel mass flow with the variations in the value of lambda was derived. The transfer function was parametrized and the parameters of it were presented in 2D maps as a function of the steady state fuel mass flow and the engine's rotational speed. In this way, insights were gained for the performance of the internal combustion engine in various operating points.

Additionally, the model of the disturbance transfer function and the plant transfer function were derived from the non-linear uncertain model. Both these models have as output the value of λ with the input of the former being the disturbance torque and the input of the latter being the frequency inverter command. The linear models were imported to the μ-synthesis algorithm in order to obtain the robust controller. The controller was analysed in terms of performance and stability in the presence of uncertainty in modelling.

Finally, the experimental validation of the controller performance was carried out at the experimental testbed of LME. The controllers functioned satisfactory and the results obtained from simulations closely matched those of the experiments.

Contents

Nomenclature

Abbreviations

LME	Laboratory of Marine Engineering
ICE	Internal Combustion Engine
PM	Particulate Matter
IMO	International Maritime Organization
AFR	Air/Fuel Ratio
AFR_{st}	The stoichiometric value of Air-to-Fuel Ratio for the given fuel
ECU	Electronic Control Unit
SSV	Structured Singular Value
DOF	Degree(s) of Freedom

Subscripts

a	air
ac	air-cooler
ad	air duct
amb	ambient conditions
av	average
B	bandwidth
c	compressor
coem	compressor and engine match
cyl	cylinder
d	disturbance
e	engine
elm	electric motor
em	exhaust manifold
exh	property immediately after the exhaust valve
f	fuel
fc	fresh charge
fd	derivative filter
fi	filter
fil	friction losses
g	exhaust gas mixture
hf	high frequency
i	incidence losses
ieg	induction to exhaust gas

im	intake manifold
$ind \rightarrow comp$	induction to compression cycle
$inj \rightarrow PC$	injection to power cycle
$inl \rightarrow ind$	inlet to induction cycle
is	is-entropic
LV	Lowest Calorific Value
ln	linear
lc	local
m	measured
mix	mixing losses
mloss	mean effective pressure friction losses
n	nominal
nl	non-linear
p	performance
r	radial
req	requested
res	exhaust gas of the previous cycle
seg	segment
sp	set-point
t	turbine
tn	tangential
tc	turbocharger
tcem	turbocharger and engine match
to	turbine outlet
u	input command
v	volumetric
vld	vane-less diffuser losses
w	cooling water
wb	water brake
0	stagnation property
1	compressor and impeller inlet
2	impeller outlet
3	compressor and diffuser outlet

Symbols

$\dot{m}$ $[kg/s]$	mass flow
$\dot{Q}$ $[\frac{J}{s}]$	heat flux
$\dot{W}$ $[J/s]$	power
A $[m^2]$	area
$A(t)$	time varying state matrix
$B(t)$	time varying input matrix
$C(t)$	time varying output matrix
c $[m/s]$	average flow velocity
c_p, c_p $[\frac{J}{kgK}]$	specific heat capacities under constant pressure/volume
D $[m]$	diameter

d	disturbance
e	error
ef [–]	air cooler efficiency
ew [–]	thermodynamic efficiency of the engine
f	mathematical function
G	transfer function model
H $[J]$	enthalpy
h $[J]$	specific enthalpy
J	Jacobian matrix
J	rotational inertia
K	controller
L $[m]$	length
M $[Nm]$	torque
m $[kg]$	mass
N $[RPM]$	rotational speed
P $[J/s]$	power
p $\frac{N}{m^2}$	pressure
R $[\frac{J}{kgK}]$	specific gas constant
r	reference
S	sensitivity function
T $[K]$	absolute temperature
t $[m]$	thickness
U $[m/s]$	velocity
u	controller command
V $[m^3]$	Volume
W	weight
z [–]	number of cylinders
β $[rad]$	angle
γ [–]	ratio of heat capacities
Δ	uncertain linear time invariant transfer function
Δh $[J]$	specific enthalpy change
δ	uncertain real parameter
ϵ	identification error
ζ	friction coefficient
η [–]	efficiency
θ	parameter vector
λ [–]	$\lambda = \frac{AFR}{AFR_{st}}$
μ	the structured singular value
Π [–]	pressure ratio
ρ $[\frac{m^3}{s}]$	density
σ [–]	slip factor
$\bar{\sigma}(\cdot)$	maximum singular value
τ $[sec]$	time constant
ϕ	observability regress-or
Ψ	turbine flow equation
ω $[rad/s]$	rotational speed

Chapter 1

Introduction

Turbocharged diesel engines constitute the most widely used propulsion system for marine applications. The domination of the diesel engine over all the other types of propulsion systems is directly connected to its high fuel efficiency, typically ranging from 40% to 50% for medium and high speed diesel engines [48].

On the grounds that the load profile of a typical vessels is relatively constant, the behaviour of marine diesel engines is usually examined in steady state conditions. However, this is not the sole case of load type that is encountered in sea-going vessels. For instance, special purpose ships like harbour tugs, ferries, ice breakers, yachts and dredgers have a load profile which displays short periods of steady load with many sharp variations in load demand over time. Moreover, all categories of vessels have time intervals with varying load demand during manoeuvring and transient operation, especially near harbours.

The nature of transient operation in diesel engine is fundamentally different from steady state conditions. During steady-state conditions the torque produced by the engine is equal to the requested torque, the crank shaft acceleration is close to zero and the physical variables associated with turbocharger are approximately constant. Unlike steady state operation, during load transients, all the variables, including engine speed, fuelling command and turbocharger shaft speed, change continuously. These phenomenon drastically affects the exhaust gas enthalpy and the air supplied to the cylinder through the turbocharger operation. Eventually, a mismatch between the air supply and the fuel burned appears due to the presence of thermal, dynamic and fluid delays in the manifolds and the turbocharger. The air-to-fuel ratio (AFR) inside the cylinder drops with a consequential drastic rise in the pollutant formations emitted from the diesel engine [33].

Nowadays, as mentioned in [43], many ports have imposed stricter emission requirements on commercial and recreational vessels and the adoption of the International Convention of Prevention of Pollution from Ships (MARPOL) Annex VI limits the main air pollutants contained in ships exhaust gas. Moreover, the International Maritime Organization (IMO) is in the process of strengthening the emission limits in the future. In view of this requirements, emission reduction is a key driven factor for the development of novel technologies in the field of marine propulsion.

Typically, a conventional marine propulsion plant consists of an internal combustion in direct connection with the propeller. This system has the advantage of offering high reliability and its performance is also satisfactory when the load is relatively constant. For ships that operate mostly at constant speed, like bulk-carriers, container-ships and

crude-oil tankers, the replacement of the conventional power plant with a hybrid-electric one may induce unnecessary conversion costs with very low benefit from emissions reduction. On the contrary, ships with a load profile that consists of relatively short periods of constant load demand the installation of hybrid propulsion may offer an effective way to reduce the pollutant emissions. An additional environmental benefit that is linked to the installation of hybrid-electric propulsion plant instead of a conventional one in special purpose vessels steams from the fact these type of vessels usually operate near ports or environmentally sensitive areas where green house emissions drastically influence the human population and stricter emission regulation are imposed by legislation authorities.

1.1 Diesel Engine Response to Load Transients

The diesel engine response to a load increase will be examined since it provides useful insights about the physical phenomena that take place in diesel engines during transient conditions.

Suppose that the engine is running at steady state and, as a result, engine acceleration is approximately zero, since the produced torque equals the requested torque and λ, which is the value of air-to-fuel ratio (AFR) divided by the stoichiometric value of air-to-fuel ratio (AFR_{st}) for the given fuel, is at acceptable levels. When the new higher load is applied, a substantial torque deficit appears, the engine is decelerated and the engine speed drops. The drop in engine speed is sensed from the speed governor which increases the fuel injected into the cylinder by an appropriate amount specified by the Engine Control Unit (typically derived from a map as a function of various physical variables).

The higher amount of fuel injected into the cylinder combined with the insufficient air supply, due to thermal and dynamic delays, leads to a drastic drop in the air-to-fuel ratio inside the cylinder and equivalently in the value of λ. The main reason for the mismatch between the air supply and the fuelling command steams from the fact that a certain time interval should elapse before the turbocharger has accelerated enough and the intake manifold pressure has increased adequately. Precisely, the increased exhaust gas temperature leads to an increase in the exhaust manifold enthalpy and, therefore, in the power supplied by the turbine. However, due to the turbocharger inertia, the compressor operation point swift slowly on its map from low air mass flow to higher boost pressure and mass flow.

The subject of transient operation of Diesel Engines is examined in [34].

1.2 Pollutant Emissions of Diesel Engines

The main pollutant formations that appear in diesel engines exhaust gases are nitrogen oxide NO_x and particulate matter PM.

1.2.1 Nitrogen Oxides

Nitrogen oxide (NO) and nitrogen dioxide (NO_2) are the main two chemical substances that constitute NO_x, with the former being the predominant pollutant formed in diesel engines. However, the relative importance of NO_2 is higher during lower engine loads [14].

The most critical factor affecting NO_x formation is the burned gas temperature. There is an exponential increase in NO_x formation rate with temperature rise. Moreover, since in diesel engines fuel distribution is not uniform, the formation of NO_x happens in high temperature regions. Another crucial parameter affecting NO_x generation is the availability of oxygen. Precisely, for a given mass of fuel, the higher the value of λ the higher the oxygen presence for combustion. Consequently, the burned gas temperature is cooler and NO_x generation process is weaker during combustion. Other factors affecting NO_x formation in diesel engines are the combustion duration, the injection timing and the in-cylinder pressure.

1.2.2 Particulate Matter

The particulate matter in diesel engines mainly consists of carbonaceous material, which is refereed as soot, with some organic compounds absorbed on it. Various metrics can be used to quantify soot, including the particles number, the total mass of particles, the size or light absorbing properties-opacity [37].

Particulate matter generation is primarily driven by the inhomogeneity of the air/fuel mixture in diesel engines. Even when engine is running in lean conditions overall, regions where the value of λ is below the stoichiometric value do exist and thus the combustion is incomplete.

Regarding the factors affecting the PM formation, it can be stated that no direct correlation can be found between PM emissions and other variables of combustion process. The reason for this lies in the fact that PM are formed during two separate phases, which are refereed as PM formation and PM oxidation, and the net difference between the PM formed and those oxidized are the PM that are emitted. On the grounds that both these number are large in magnitude and close to one another, PM cannot be accurately predicted [13]. However, experimental data illustrate that the in-cylinder temperature and the availability of oxygen greatly determine PM emissions [1].

1.3 Choice of Controlled Variable

The signal that is chosen to be fed into the robust controller is the value of λ. The main reasons that justify this choice are:

1. Even though λ is not a measure of emissions itself, it is still a reliable estimate of them. As illustrated in Fig. 1.1, there is a strong correlation between the value of λ and the main emissions formed in diesel engines. Particularly, the role of λ is even more crucial for diesel engines where load is primarily controlled with this parameter.

2. Lambda is a really suitable signal for control purposes since no significant noise is presented in this value and the dynamics of λ are neither very slow nor very fast [13]

3. Unlike λ which can be easily modelled from the air and fuel path dynamics, NO_x and PM are complex functions of many variables and, thus, cumbersome to model analytically.

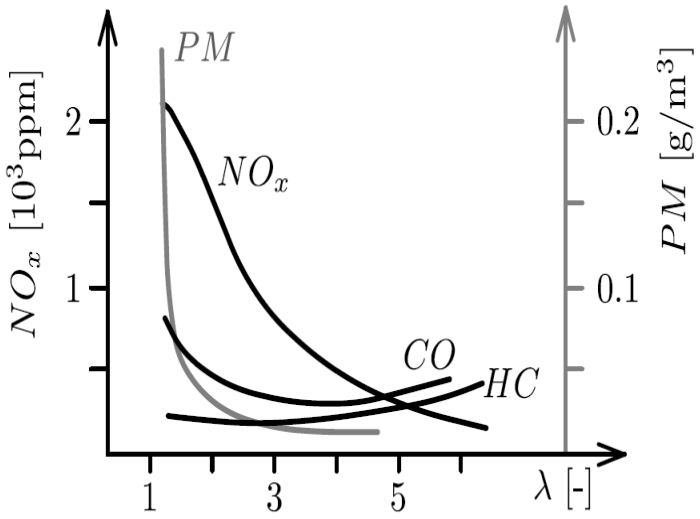

Figure 1.1: NO_x and PM as a function of λ.-Figure obtained from [13].

1.4 Literature Review

1.4.1 Hybrid-Electric Powertrains

Although the number of publications in the subject of hybrid-electric powertrain control for marine propulsion plants is limited, the control applications in automotive hybrid-electric powertrains has been exhaustively examined by numerous authors. The main objective of the majority of the publications in the field of hybrid-electric vehicle is the energy management/split between the internal combustion engine and the electric machine.

One main category of energy management strategies is the optimisation techniques. The category of optimal and sub-optimal techniques includes linear, quadratic and dynamic programming [35],[40],[20] and [9]. One major drawback associated with optimal strategies, which also limits their potentials for marine applications, is the fact that the exact knowledge of the driving cycle is necessary in order to obtain the solution of the optimization problem. Another problem, according P.Pisu et al.[31], is that solutions to optimizations problems lead to non analytic expressions for the controllers derived and, thus, difficult to implement in real world hybrid-electric plants.

Moreover, heuristic methods such as fuzzy logic [38], [30] and neural networks [5], have also adopted but neither achieve an optimal solution not robustness with respect to performance. Another method is linked to stochastic optimization and predictive control [19],[21]. Since the optimization goal involves the minimization of an objective function over a range of possible driving cycles rather than a specified one, the method seems promising for marine applications where the exact load profile of the vessel is never perfectly known. However, a great disadvantage associated with the aforementioned method is that the controller is designed off-line and implemented on-line with the aid of a look up table.

Clearly, dealing with the control problem only from a quasi-static perspective can

severely limit the potential benefits of a stochastic optimization, due to the presence of un-modelled dynamics and exogenous disturbances in the real plant, unless the static algorithm is integrated in a control system framework that also incorporates a dynamic and robust control system. The possibilities of combining a quasi-static optimization algorithm with a robust control algorithm was investigated by Sajjad Fekri and Francis Assadian in [10]. Another, worth mentioning publications that does not, however, deals with energy management in a dynamic way is [32].

1.4.2 Feedback Control Systems and Control Oriented Modelling

Introductory knowledge on feedback control system theory regarding uncertainty modelling, generalized plant derivation and controller implementation was acquired mainly from [42]. Moreover, the subject of the μ-controller synthesis and analysis is treated with more mathematical formality compared to [42] by K.Zhou and J.C.Doyle in [49]. Finally, the essential practical framework for the implementation of the controller, which is the main concern in the present thesis, is presented in [12] and [4].

For the virtual sensor model, the publications of J.Gravdal and O.Egeland [11] along with the work of S.Dixon [7] provide insights for the compressor model derivation. O.Storset et al. published the journal [44], which proved very useful for the adaptive observer design to estimate the volumetric efficiency on-line. The fundamental theoretical knowledge for time varying systems and on-line observation was obtained from [26] and [16], respectively.

The main reference for the modelling of the individual components of the internal combustion engine is the work of L.Guzzella [13]. Additional insight was also gained for the doctoral thesis of E.Alfiery [1]. Further details for engine parts modelling were also found in [8], [15] and [47]. Finally, the fuel mass flow estimation, which is a critical physical variable, is estimated using Willans approximation with details about the method presented in [36].

For certain components of the hybrid power-train that system identification principles rather than phenomenological modelling is applied, the fundamental information gained from the introductory book of L.Ljung [22] was crucial. An overview of the identification techniques is covered by K.J. Astrom and P. Eykhoff in the article [3]. A last valuable guide when dealing with identification problems in Matlab environment is [25].

1.5 The Experimental Plant

The hybrid-electric powertrain system of the LME consists of an ICE in parallel connection to an EM. Thus, the rotational speeds of EM and ICE are identical and the supplied torques add together. The desired torque demand is applied through a water brake, which is manipulated by an H_∞ controller. Figure 1.2 illustrates the hybrid-electric experimental plant of the LME along with a visual representation of this plant in AUTOCAD.

The water brake at LME is manufactured by AVL Zoellner GmbH, type 9n 38F, and has a load capacity of 1200 kW, with maximum speed 4000 rpm. The hydrodynamic water brake consists of two main part; namely, the rotor and the stator. The former is driven by the ICE and the EM while the stator is fixed and grounded. The rotor can rotates freely within the water brake casing and the relative motion between the

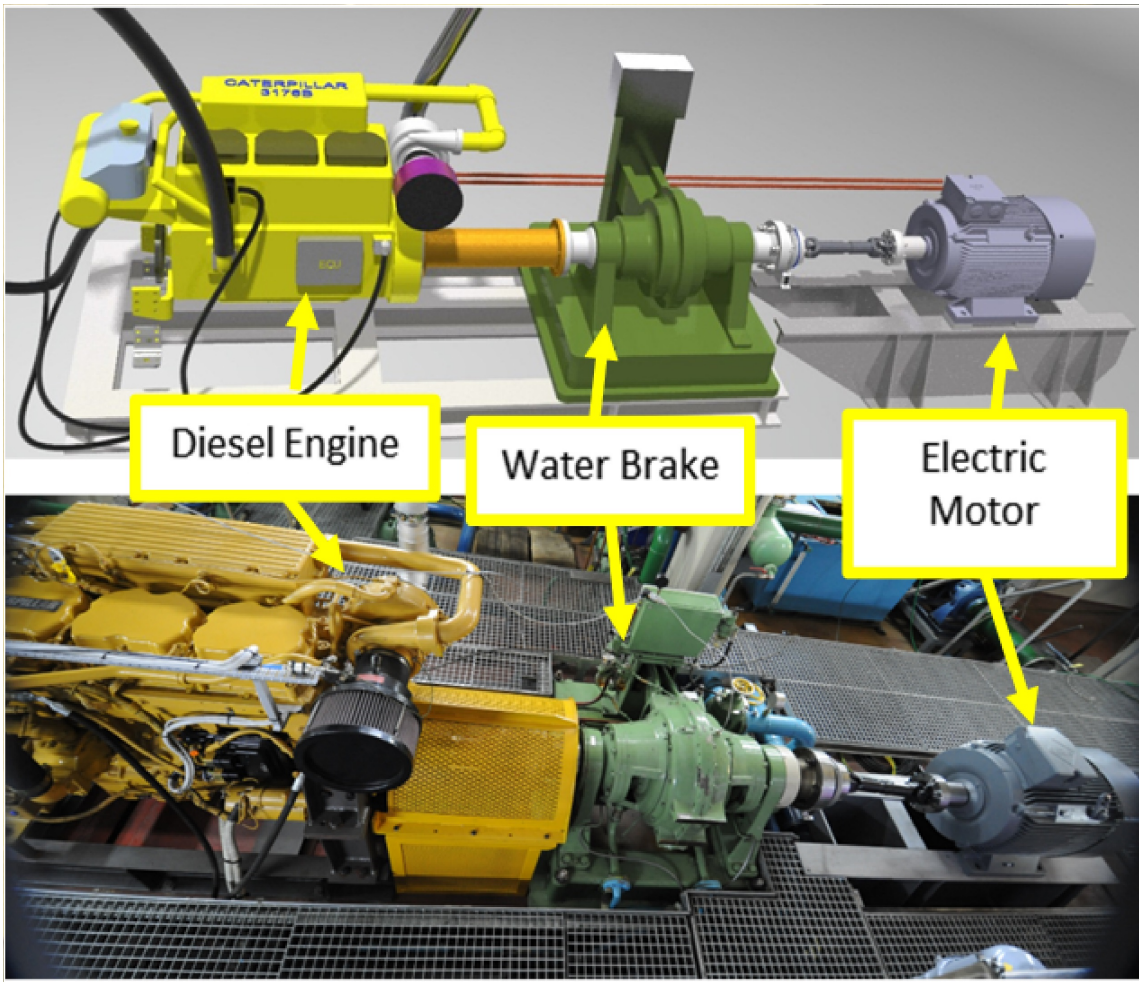

Figure 1.2: The LME hybrid-electric testbed.

rotor and the stator generates a centrifugal force that is subsequently transformed into a toroidal circulation of the fluid [27]. This circulation absorbs power from the ICE and the EM; therefore, acts as a resisting torque to the external torque applied.

The water dynamometer installed in the LME test bed facility can be partially filled with water and thus the applied torque can be variable depending on the water level [46]. The water level is adjusted through a valve, which regulates the flow to the dynamometer. The command from the H_∞ controller is fed to the pneumatic mechanism of the valve and controls its opening so the desired torque demand is achieved in a closed loop control.

Moreover, the internal combustion engine of the experimental propulsion plant is a CATERPILLAR 3176B four-stroke turbocharged marine diesel engine with rated power 448 kW at 2300 RPM. The ICE has five different sensors installed in it, which are depicted in Fig. 1.3.

As mentioned in the beginning of this section the ICE is coupled to an EM which is an AC asynchronous-induction three phase motor with squirrel cage. Precisely, the motor is of the type IE1-K21R 315 S4 and is manufactured by VEM with a rate power of 110 kW.

In an induction motor, the current supplied to the stator generates a magnetic flux which induces an opposing current to the winding of the rotor, a phenomenon conceptually similar to the operation of an electric transformer. In an induction machine the sum of the rotational velocity of the magnetic flux vector of the rotor and the rotational speed of the rotor has to equal the rotational speed of the stator magnetic flux vector. Therefore, the revolutions of the rotor are fully determined from the frequency of the current in the rotor winding [2].

However, the present induction machine is equipped with a power electronic device known as adjustable frequency drive. Through this device the decoupling between the the stator current, involved in the air gap flux, from the portion of the flux associated with torque production is achieved. In this way it is possible to obtain the desired torque at the specified speed without any constraint steaming from the stator's electric current frequency [41].

1.6 Structure of the Thesis

This thesis is structured as follows: In Chap. 2 the feasibility of a virtual λ-sensor design is examined and the phenomenological modelling of it is presented. A non-linear first-principles uncertain model of the hybrid-electric powertrain is derived in Chap. 3. Chap 4 presents the process of obtaining a quasi-static model of the ICE. This static non-linear model proved very useful in computing the steady state physical variables in the operating points of linearisation in Chap. 5, where a linear model of the hybrid-electric powertrain is obtained. Following the linear system derivation, the next step is the development of a robust controller which is treated in Chap. 6 and the experimental validation of the controller is presented in Chap. 7. Finally, Chap. 8 is dedicated to conclusions.

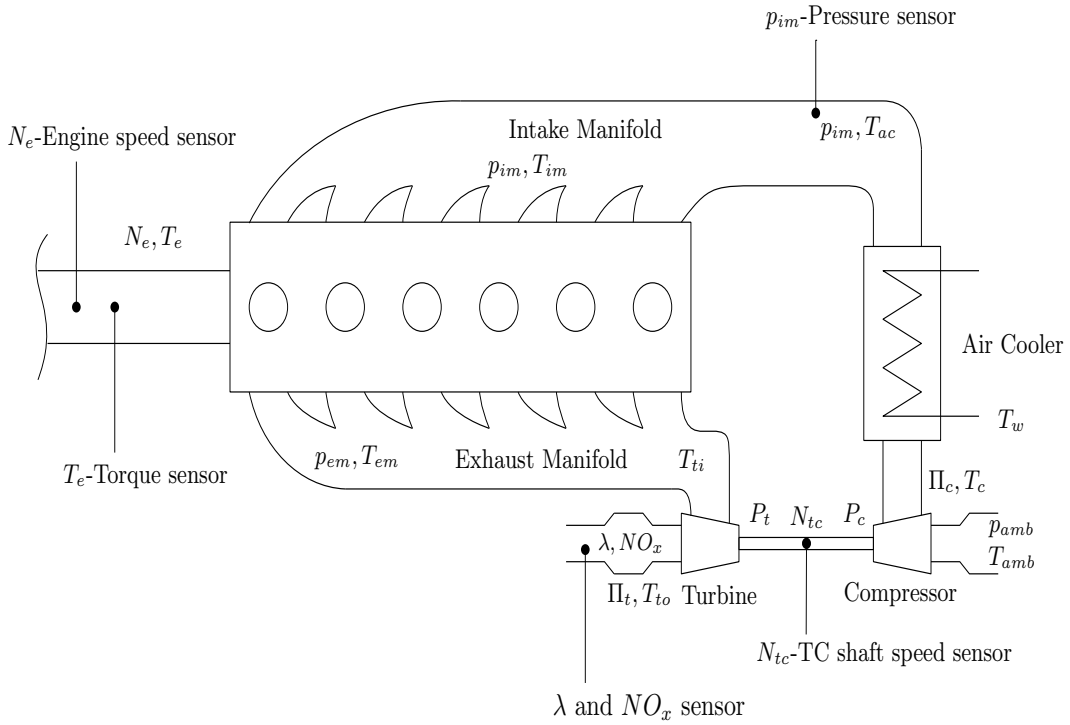

Figure 1.3: Engine model with the installed sensors.

Chapter 2

Virtual Sensor Design

In this chapter the air and fuel path models of the diesel engine are obtained combining thermodynamic relationships, semi-empirical formulas and on-line parameter identification principles. The model is produced with the intention of offering a reliable estimate of λ inside the cylinder using four physical variables which are available through measurements; namely, the rotational speed of the engine N_e, the turbocharger shaft speed N_{tc}, the barometric pressure at the air cooler outlet p_{im} and the torque produced of the internal combustion engine T_e. The schematic representation of the main components of the virtual sensor model is given in Fig. 2.1.

2.1 Physical Sensor

The physical sensor of lambda is installed in the exhaust duct, approximately 1 m after the exhaust valves of the diesel engine. Consequently, a variation in λ will be sensed only after the exhaust gas has arrived at this point.

The time that elapses between the end of the combustion cycle and the measuring of λ for the exhaust gas of the corresponding cycle is the time interval that the sensed signal is close to the reference value while the the value of λ inside the cylinder may be below the reference value. If the measured λ is used for controller purposes, then the error signal for the feedback controller is approximately zero during this time interval; thereby, the command to the electric engine is zero too.

For the aforementioned reason, if the controlled variable is the value of λ inside the cylinder instead of λ as measured from the sensor, engine's response to load transients will be improved with λ experiencing a less sharp drop. The advantage of this approach steams from the fact that the controller's command to the electric engine will no longer be zero during the time interval of the mismatch between the value of λ sensed and the actual value of λ inside the cylinder.

An additional advantage of this approach is associated with the way the Engine's Control Unit (ECU) functions. During fast load reductions, the ECU senses the acceleration and drastically reduces the injected fuel or even stops fuelling. For this reason, large spikes appear in the measurement of λ. These spikes correspond to positive deviations from the reference value of λ and represent very low PM and NO_x emissions. Therefore, it would be desirable for the controller designed to ignore them, otherwise the command to the electric motor command would display undesirable oscillatory behaviour.

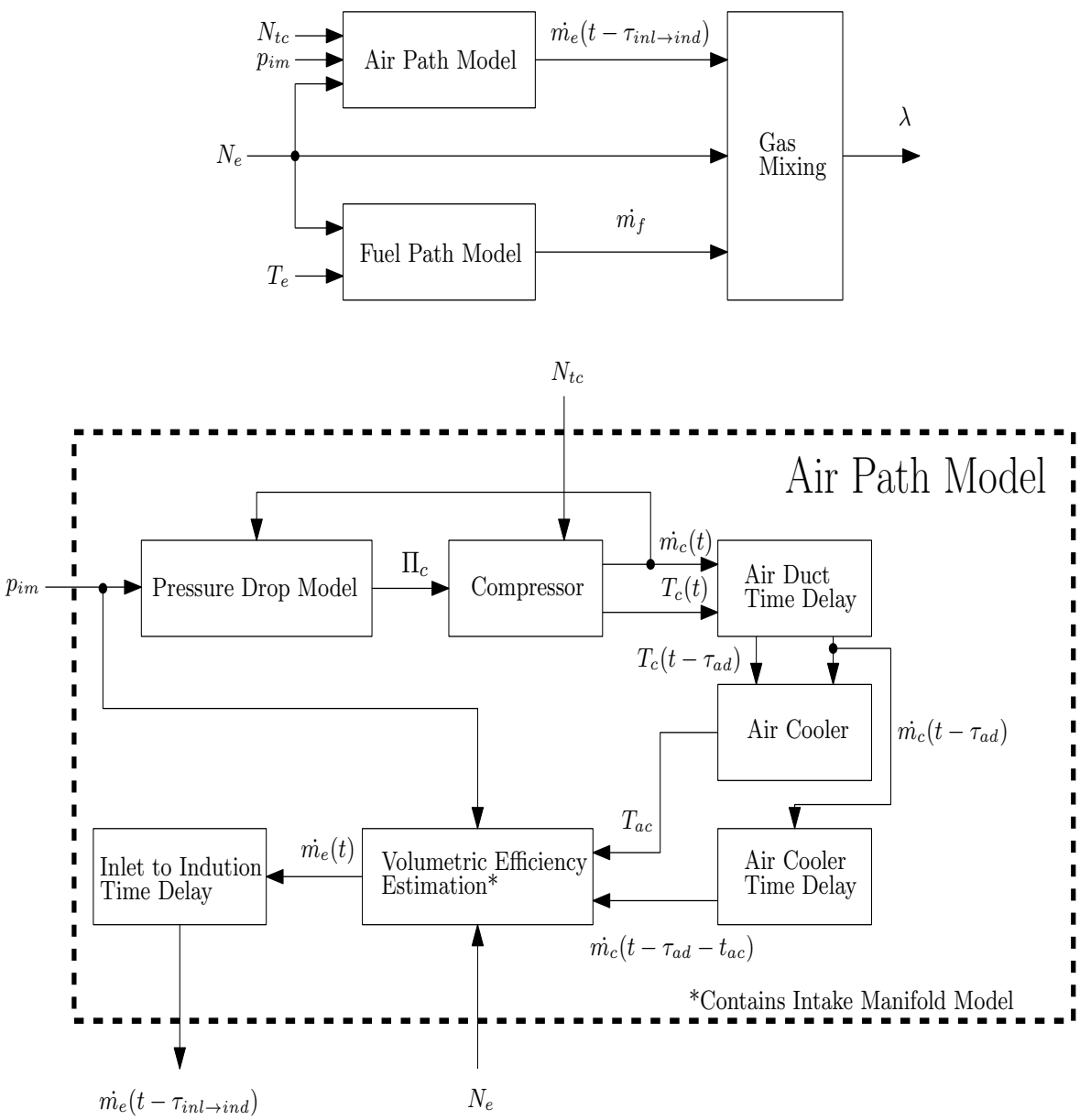

Figure 2.1: Virtual sensor fundamental components.

2.2 Air Path Modelling

2.2.1 Intake Manifold Modelling

Intake manifold is modelled as a fixed volume where the thermodynamic states (pressure, temperature, gas composition) are assumed to be homogeneous [13] . The mass balance in the intake manifold yields

$$\frac{dm_{im}}{dt} = \dot{m}_c - \dot{m}_e \tag{2.1}$$

where $\dot{m}_c$ is the mass flow through the compressor, $\dot{m}_e$ is the mass of air aspirated by the engine and $\frac{dm_{im}}{dt}$ is the rate of change in the mass of air that is accumulated in the intake manifold.

Moreover, assuming that the kinetic and potential energy of the fluid, in both the inlet and outlet of the intake manifold, are negligible and applying energy balance, the following differential equation is obtained

$$\frac{dH_{im}}{dt} = \dot{H}_c - \dot{H}_e \tag{2.2}$$

The rate of change in the intake manifold enthalpy is given by

$$\frac{dH_{im}}{dt}(t) = \frac{d(m_{im}(t)e_{im}(t))}{dt} = \frac{d(m_{im}(t)c_{va}T_{im}(t))}{dt} = c_{va}\frac{d(m_{im}T_{im})}{dt} \tag{2.3}$$

where c_{va} is the specific heat capacity under constant volume for the air.

The enthalpy of the fluid entering and leaving the intake manifold can by

$$\dot{H}_c = c_{pa} \cdot \dot{m}_c \cdot T_{ac} \tag{2.4}$$

and

$$\dot{H}_e = c_{pa} \cdot \dot{m}_e \cdot T_{im} \tag{2.5}$$

, respectively. In Eq. 2.4, T_{ac} is the temperature immediately after the air-cooler while in Eq. 2.5 T_{im} is the temperature in the intake manifold, which is assumed equal to the temperature of the air aspirated by the engine and c_{pa} is the heat capacity under constant pressure for the air.

Assuming that ideal gas law is valid, the following equation is obtained

$$m_{im}T_{im} = \frac{p_{im}V_{im}}{R_a} \tag{2.6}$$

where p_{im} is the pressure in the intake manifold and V_{im} is the volume of the manifold.

Inserting Eqs. 2.6, 2.5, 2.4 and 2.3 into Eq. 2.2 yields

$$\frac{dp_{im}}{dt} = \frac{\gamma_a R_a}{V_{im}} \cdot \dot{m}_c \cdot T_{ac} - \frac{\gamma_a R_a}{V_{im}} \cdot \dot{m}_e \cdot T_{im} \tag{2.7}$$

The two air flows $\dot{m}_c$ and $\dot{m}_e$ have to be modelled in terms of the measured variables.

2.2.2 Assessment of Compressor Maps Models

Compressor performance, both the air mass flow through it ($\dot{m}_c$) and the is-entropic efficiency ($\eta_{is,c}$), is usually presented in map as a function of dimensionless parameters. The introduction of the dimensionless quantities aims to make the compressor maps valid for different machine sizes (but still of the same design features) and various input/ambient conditions [8].

Two fundamentally different mathematical models have been propesed for the representation of the compressor flow characteristics.

1. **MODEL I**, $\boldsymbol{\dot{m}_c = f(\Pi_c, N_{tc})}$: The air mass flow $\dot{m}_c$ through the compressor is expressed as a function of the pressure ratio Π_c and the turbocharger speed N_{tc}.
2. **MODEL II**, $\boldsymbol{\Pi_c = g(\dot{m}_c, N_{tc})}$: The compressor pressure ratio Π_c is presented as a function of the air mass flow $\dot{m}_c$ and the turbocharger speed N_{tc}.

A comparative examination of these two models is presented in [28]. On the grounds that only measurements of the turbocharger speed N_{tc} and the pressure in the intake manifold $p_{im}$are available, there is no alternative other than choosing MODEL I. According to [28], the benefits of MODEL I are associated with the low sensitivity and the reduced stiffness when it is incorporated as a part in an engine model.

Engine is modelled as a volumetric pump with the aspirated mass of air into the engine given by

$$\dot{m}_e = \frac{\eta_v V_{cyl} p_{im} z N_e}{R_a T_{im} 120} \tag{2.8}$$

where V_{cyl} is the cylinder volume, η_v is the volumetric efficiency and z is the number of cylinders.

Moreover, the pressure ratio of the compressor can be evaluated as follows

$$\Pi_c = \frac{p_{im} + \zeta_{total} \frac{1}{2} \rho_3 c_3^2 + pd_{ac}}{p_{amb}} \tag{2.9}$$

where pd_{ac} is the pressure drop in the air cooler and c_3 is the average flow velocity at the compressor outlet, given by

$$c_3 = \frac{\dot{m}_c}{\rho_3 A_{duct}} \tag{2.10}$$

The density at the compressor outlet can be evaluated from the known pressure ratio Π_c and the is-entropic efficiency $\eta_{is,c}$ using the thermodynamic relationship

$$\rho_3 = \rho_1 \frac{(\Pi_c)^{\frac{\gamma_a}{\gamma_a - 1}} - 1 + n_{is,c}}{\Pi_c \cdot \eta_{is,c}} \tag{2.11}$$

In Eq. 2.9, ζ_{total} is a coefficient which incorporates the two main pressure losses occur in the pipeline, namely:

1. The linear pressure losses, which are taken into account with a coefficient $\zeta_{ln} = \lambda_{fr} \cdot \frac{l}{D}$, where l and D are the length and the diameter of the pipe, respectively. Additionally, λ_{fr} is coefficient derived from the Moody chart as a function of Reynolds number and the relative pipe roughness $\lambda_{fr}(Re, \frac{D}{\epsilon})$. The linear pressure losses are the same for two pipes which have the same length, diameter and relative roughness even if they have different elbows, fittings etc.

2. The local pressure losses, which are considered with the coefficient ζ_{lc}, are associated with pressure drops in fittings, elbows and control valves. This pressure drops are difficult to model analytically but can be derived from charts and diagrams which are available in Fluid Mechanics Textbooks.

Having an estimate of the above-mentioned coefficients in the operation point of the engine, the compressor pressure ratio is computed from Eq. 2.9.

In this point it is worth noting that the mass of air aspirated by the internal combustion engine, for fixed fuelling rate $\dot{m}_f$ and constant engine speed N_e, is approximately a linear function of the pressure in the intake manifold p_{im} as can be seen from Eq. 2.8 (No significant variations are presented in T_{im} and η_v). Moreover, in steady state and very slow transient operation, no mass of air is accumulated in the intake manifold and the mass of air produced by the compressor is equal to the mass of air aspirated by the engine at the same time instant; this can be formulated mathematically by the writing that

$$\frac{dm_{im}}{dt} = 0 \tag{2.12}$$

and

$$\dot{m}_c(N_{tc}, \Pi_c) = \dot{m}_e[N_e, p_{im}(\Pi_c, m_c, N_{tc})] \tag{2.13}$$

Although MODEL I presents high sensitivity to pressure variations especially in the low turbocharger shaft speed region, where the slope of mass flow with respect to the pressure ratio is considerably large, the angle of intersection between $\dot{m}_c$ and $\dot{m}_e$ is never close zero but lies within the range of 60 to 90 degrees. Thereby, the sensitivity of the mass flow rate $\dot{m}_c$ in the parameter Π_c is radically reduced.

From now on the assumption that $\dot{m}_c = \dot{m}_c(N_{tc}, \Pi_c)$ is made; thus, MODEL I is adopted for the compressor modelling.

2.2.3 Volumetric Efficiency Estimation Techniques

The volumetric efficiency η_v is essentially a measure of how different the engine is from an ideal volumetric pump. Clearly, volumetric efficiency drastically determines engine's ability to aspire air [44]. Consequently, it can substantially determines the value of λ inside the cylinder.

Volumetric efficiency η_v can be estimated through detailed CFD simulations. Another way of volumetric efficiency η_v computation, suggested in [13], is from a two-dimensional map of the mean effective pressure p_{em} and engine's speed N_e. The disadvantage of the former method is the that it requires precise and time-consuming simulations while the drawback of the latter is the fact that is less accurate for Diesel engines where volumetric efficiency η_v depends in other parameters apart from the mean effective pressure p_{em} and engine's speed N_e.

Precise dimensional analysis for turbocharged diesel engines, presented by Taylor in [45], suggests that volumetric efficiency can be given by a product of two independent efficiencies, with the one being a function of the pressure ratio between the exhaust and the intake manifold p_{em}/p_{im} and the other being a function of the engine speed N_e and the intake manifold temperature T_{im}.

$$\eta_v = \eta_\rho\left(\frac{p_{em}}{p_{im}}\right) \cdot \eta_z\left(N_e, \sqrt{T_{im}}\right) \tag{2.14}$$

One should take into account that the exhaust manifold pressure p_{em} is very difficult to measure due to the adverse conditions in it (high temperature, high velocity of exhaust gases and presence of pollutant formations). For this reason, the assumption introduced by Storset et.al in [44], that volumetric efficiency depends on engine speed N_e and a time-varying parameter $\theta(t)$ that needs to be identified, is adopted. Under these assumptions, the volumetric efficiency is product of two terms

$$\eta_v = P[\omega_e(t)] \cdot \theta(t) \tag{2.15}$$

2.2.4 Air Cooler Model

The temperature immediately after the compressor can be calculated from the known pressure ratio in the compressor and the is-entropic efficiency. The temperature after the compressor is given by

$$T_c = T_{amb} + T_{amb} \cdot [\Pi_c^{\frac{\gamma_a - 1}{\gamma_a}} - 1]/\eta_{is,c} \tag{2.16}$$

The air cooler can be modelled as a heat exchanger. The effectiveness of the air cooler is assumed to be a quadratic function of the air flow $\dot{m}_c$ [15].

$$ef = 1 - c \cdot \dot{m}_c{}^2 \tag{2.17}$$

And the air temperature T_i in the cooler outlet is

$$T_{ac} = ef \cdot T_w + (1 - ef) \cdot T_c \tag{2.18}$$

where T_w is the temperature of the coolant.

2.2.5 System of Differential Equations

Eq. 2.7 and Eq. 2.8 yield

$$\frac{dp_{im}}{dt} = \frac{\gamma_a R_a}{V_{im}} \cdot \dot{m}_c \cdot T_{ac} - \frac{\gamma_a V_{cyl} p_{im} z N_e}{120 V_{im}} \cdot \eta_v \tag{2.19}$$

Moreover, substituting Eq. 2.8 in Eq. 2.1 and using assumption 2.15 yields

$$\frac{dm_{im}}{dt} = \dot{m}_c - \frac{\eta_v V_{cyl} p_{im} z N_e}{R T_{im} 120} = \dot{m}_c - \frac{P(\omega_e)\theta V_{cyl} z N_e}{120 V_{im}} \cdot m_{im} \tag{2.20}$$

where the second equality is obtained using the ideal gas law. It follows from assumption 2.15 that

$$\frac{dp_{im}}{dt} = \frac{\gamma_a R_a}{V_{im}} \cdot \dot{m}_c \cdot T_{ac} - \frac{\gamma_a V_{cyl} z N_e P(\omega_e)\theta}{120 V_{im}} \cdot p_{im} \tag{2.21}$$

Equations 2.21, 2.20, 2.18 and 2.9 are mathematical system that describe the intake manifold dynamics and will be used to identify the unknown volumetric efficiency η_v.

2.2.6 Derivation of Compressor Map

Ideal Enthalpy

Incoming gas enters the impeller eye with velocity

$$c_1 = \frac{\dot{m}_c}{\rho_1 \cdot A_1} \tag{2.22}$$

where ρ_1 is the density at the compressor inlet. At the outlet of the impeller the radial component of the velocity is given by

$$c_{2r} = \frac{\dot{m}_c}{\rho_2 \cdot \pi \cdot D_2 \cdot t_2} \tag{2.23}$$

and the tangential velocity under the assumption of no slip can be calculated as follows

$$c_{2tn} = U_2 - c_{2r} cot(\beta_2) \tag{2.24}$$

where U_2 is the impeller tip velocity

$$U_2 = \omega_{tc} \cdot r_2 \tag{2.25}$$

The so called "slip factor" is introduced. It is defined as the ratio of the real tangential velocity $c_{2\acute{t}n}$ to the ideal velocity with no slip c_{2tn} [7]

$$\sigma = \frac{c_{2\acute{t}n}}{c_{2tn}} \tag{2.26}$$

For turbo-machines the applied torque equals the change on the angular momentum of the fluid between the compressor inlet and impeller outlet. The power delivered to the fluid is the product of the rotational speed of the shaft and the applied torque. The following equation holds

$$\dot{W}_c = \omega_{tc} \cdot \dot{m}_c (r_2 c_{2\acute{t}n} - r_1 c_{1tn}) = \dot{m}_c (U_2 c_{2tn} - U_1 c_{1tn}) \tag{2.27}$$

The rate of change in the energy delivered to the fluid is the ideal stagnation enthalpy increase over the compressor. Thereby, the equation that is obtained is

$$\dot{W}_c = \dot{m}_c \cdot \Delta h_{0cideal} \tag{2.28}$$

Equations 2.27 and 2.28 yield

$$\Delta h_{0cideal} = U_2 c_{2\acute{t}n} - U_1 c_{1tn} \tag{2.29}$$

The flow at the impeller inlet is assumed to be axial, thus the tangential speed c_{1tn} is equal to zero and Eq. 2.29 is simplified to

$$\Delta h_{0cideal} = U_2 c_{2\acute{t}n} \tag{2.30}$$

Equation 2.30 with the use of the slip definition and Eq. 2.24 becomes

$$\Delta h_{0cideal} = \sigma (U_2^2 - U_2 \cdot c_{2r} \cdot cot(\beta 2)) \tag{2.31}$$

Enthalpy Losses

There are at least four main categories of enthalpy losses in a centrifugal vane-less compressor, namely:

1. **Incidence Losses**

   This type of enthalpy losses occur due to incidence of the incoming fluid onto the rotor of the compressor at the inlet section. It is one of the major type of losses that greatly determines the compressor characteristic curve. The incidence losses can be calculated in various ways. From the most widely used models is the so called "NASA shock loss theory" which is based on the tangential component of velocity which is destroyed during incidence. The use of this model leads to a loss varying with the square of mass flow, being zero when the relative angle between the fluid and the fixed bladed angle is zero [11].

   As the gas hits the inducer, its velocity instantaneously changes its direction to comply with the fixed blade inlet angle. The direction is changed from the direction of flow β_1 to β_{1b} which is the fixed blade angle, and the kinetic energy associated with this tangential component of the velocity is lost. Therefore, the incidence loss can be expressed as

   $$\Delta h_i = \frac{W_{\theta 1}^2}{2} \tag{2.32}$$

   where the velocity lost due to incidence is described by the following equation

   $$W_{\theta 1} = U_1 - cot(\beta_{1b}) c_{1a} \tag{2.33}$$

   and

   $$c_{1a} = c_1 \tag{2.34}$$

   since the assumption that there is no tangential component of fluid velocity at the inlet has been made.

   Substituting 2.33 into 2.32, yields

   $$\Delta h_i = \frac{(U_1 - cot(\beta_{1b}) c_{1a})^2}{2} = \frac{(U_1 - \frac{cot(\beta_{1b}) \dot{m}_c}{\rho_{01} A1})^2}{2} \tag{2.35}$$

   where the last equivalence is derived from 2.22 and the use of assumption 2.34.

2. **Friction Losses**

   Friction losses are associated with the adhesive force between the fluid flow and the channel surfaces. In order to estimate friction losses the assumption adopted is that the flow is fully developed. The friction losses in the impeller are calculated using the following equation

   $$\Delta h_{fil} = f_i \cdot (\frac{l_i}{D_i}) \cdot \frac{w_b^2}{2} \tag{2.36}$$

   where D_i is the hydraulic diameter, since the compressor cross section is not a circle, l_i is the average length of the impeller flow passage and w_b is the mean fluid velocity in the impeller given by

   $$w_b = \frac{\dot{m}_c}{(\rho_{01} + \rho_{02})/2 \cdot A_{av}} \tag{2.37}$$

Additionally, the friction factor $f_i$is computed accoding to [11], using Haaland's formula

$$\frac{1}{\sqrt{f_i}} = -1.8 \cdot log[\frac{6.9}{Re} + [\frac{\frac{\epsilon}{D_i}}{3.7}]^{1.1}] \tag{2.38}$$

The Reynolds number is calculated as follows

$$Re = \frac{U_2 b_2}{\nu} \tag{2.39}$$

where ν is the kinematic viscosity of the fluid.

3. **Mixing Losses**

   The mixing losses are encountered at the outlet of the impeller section where the so called "jet flow" is mixed with the "wake flow". Although the flow of fluid at the impeller outlet is uniform in axial direction, the simultaneous presence of both low momentum fluid and high energy cores in radial direction causes the sudden mixing of these fundamentally different types of flows.

   Mixing losses are estimated using the conservation laws of jet-wake theory and are given by the formula

$$\Delta h_{mix} = \frac{1}{1 + tan^2\beta_2} \cdot \frac{1 - \epsilon_{wake} - b^\star}{1 - \epsilon_{wake}} \cdot \frac{c_2^2}{2} \tag{2.40}$$

   where

$$tan(\beta_2) = \frac{c_{r2}}{\sigma U2} \tag{2.41}$$

   In addition, ϵ_{wake} is a function of the blade to blade space occupied by the wake and $b^\star$ is the ratio of the diffuser inlet width and the impeller exit width.

4. **Vane-less Diffuser Losses**

   In the volume occupied by the diffuser the primary and secondary flows are mixed. As a result of friction and other factors, a loss, is experienced.

   Stanitz developed a numerical procedure for the analysis of flow in a vaneless diffuser and the estimation of losses in the diffuser section [6]. Although mixing losses have not be taken into account by Stanitz, they have already been included in the loss model described previously. According Stanitz the enthalpy losses in the vane-less diffuser section of an axial compressor are given by

$$\Delta h_{vld} = c_{pa} T_{02} [(\frac{p_3}{p_{03}})^{\frac{(\gamma-1)}{\gamma}} - (\frac{p_3}{p_{02}})^{\frac{(\gamma-1)}{\gamma}}] \tag{2.42}$$

Efficiency

The is-entropic efficiency of the compressor is defined as

$$\eta_{is,c} = \frac{\Delta h_{0ideal}}{\Delta h_{0ideal} + \Delta h_{loss}} \tag{2.43}$$

where Δh_{loss} is the sum of the above-mentioned losses occurring in the impeller and the diffuser

$$\Delta h_{loss} = \Delta h_i + \Delta h_{fil} + \Delta h_{mix} + \Delta h_{vld} \tag{2.44}$$

The aforementioned definition of efficiency has to be corrected so as the effect of other type of losses that are difficult to model analytically and have a smaller influence on the efficiency can be also taken into account. These type of losses are taken into consideration by directly subtracting them from the is-entropic efficiency $\eta_{is,c}$ given in Eq. 2.43. One type of these enthalpy losses is clearance loss $\Delta\eta_c$, which is mainly a function of the the axial clearance at the impeller tip. Moreover, another loss which has to be included is the back-flow loss $\Delta\eta_{bf}$. This loss is associated with the existence of pressure gradients in the impeller tip region which make necessary the reprocess of certain part of the fluid and the re-injection of it into the impeller of the compressor. Finally, the volute loss $\Delta\eta_v$ steams from the inability of the volute to use all the available energy out of the diffuser. Nonetheless, this loss is not so significant in vane-less diffusers.

The corrected is-entropic efficiency is then given by the following formula

$$\eta_{is,c} = \frac{\Delta h_{ideal}}{\Delta h_{ideal} + \Delta h_{loss}} - \Delta\eta_c - \Delta\eta_{bf} - \Delta\eta_v \tag{2.45}$$

Pressure Ratio Relationship

The overall efficiency $\eta_{is,c}$ is given by

$$\eta_{is,c} = \frac{h_{03is} - h_{01}}{h_{03} - h_{01}} = \frac{h_{03is} - h_{01}}{h_{02} - h_{01}} = \frac{C_p T_{01} \cdot (\frac{T_{03is}}{T_{01}} - 1)}{h_{02} - h_{01}} \tag{2.46}$$

where the term $h_{02} - h_{01}$ can be substituted from Eq. 2.31 and, in this way, Eq. 2.46 becomes

$$\eta_{is,c} = \frac{C_p T_{01} \cdot (\frac{T_{03is}}{T_{01}} - 1)}{\sigma(U_2^2 - U_2 \cdot c_{2r} \cdot cot(\beta 2))} \tag{2.47}$$

The overall pressure rise in compressor is given for ideal is-entropic compression by

$$\frac{p_{03}}{p_{01}} = (\frac{T_{03is}}{T_{01}})^{\frac{\gamma}{\gamma-1}} \tag{2.48}$$

Substituting Eq. 2.47 into Eq. 2.48 the pressure ratio becomes

$$\frac{p_{03}}{p_{01}} = (1 + \frac{\eta_{is,c} \cdot \Delta h_{ideal}}{T_{01} c_{pa}})^{\frac{\gamma_a}{\gamma_a - 1}} \tag{2.49}$$

The is-entropic efficiency $\eta_{is,c}$ is a function of the turbocharger speed N_{tc}, the mass flow through the compressor $\dot{m}_c$ and the pressure loss in the diffuser Δh_{vld} . The vane-less diffuser enthalpy losses depend on the dynamic and static pressures at the compressor inlet, impeller outlet and compressor outlet. The term Δh_{0ideal} is a function of N_{tc} and $\dot{m}_c$. Moreover, the stagnation temperature at the compressor inlet T_{01} varies with $\dot{m}_c$ for constant ambient conditions. Consequently, for known turbocharger speed N_{tc}, pressure ratio Π_c and known ratio of the total pressure increase to the pressure increase in the impeller section p_3/p_2, the right hand side of the equation is just a non-linear function of the mass flow $\dot{m}_c$.

Regarding the left hand side of Eq. 2.49, for a given mass flow $\dot{m}_c$, Eq. 2.22 can be used to estimate the inlet flow velocity c_1. The air in the engine room is assumed to be at temperature T_{amb}, pressure p_{amb} and at zero velocity. When the air enters

compressor, the temperature drops from T_{amb} to T_1 as a result of the velocity increase. Precisely, the new temperature is given by the following formula

$$T_1 = T_{amb} - \frac{1}{2}c_1^2 \tag{2.50}$$

The static pressure at the compressor inlet, assuming no pressure drop and is-entropic compression, is given by

$$p_{1s} = p_{amb} \cdot \left(\frac{T_1}{T_{amb}}\right)^{\frac{\gamma_a}{\gamma_a - 1}} \tag{2.51}$$

In a more realistic approach, the process could not be considered perfectly is-entropic. To account for this phenomenon the previously calculated pressure from Eq. 2.51 is reduced by a term proportional to the square of speed c_1

$$p_1 = p_{1s} - \zeta_{in}\frac{1}{2}\rho_{01}c_1^2 \tag{2.52}$$

The factor ζ_{in} is mainly a function of the inlet geometry and can be derived from diagrams. Moreover, using the ideal gas laws density at the compressor inlet is given by

$$\rho_1 = \frac{p_1}{RT_1} \tag{2.53}$$

Finally, the dynamic pressure at the compressor inlet is given by

$$p_{01} = p_1 + \frac{1}{2}\rho_1 c_1^2 \tag{2.54}$$

Estimating density ρ_3 from Eq. 2.11 the dynamic pressure at the compressor outlet can also be calculated by

$$p_{03} = p_3 + \frac{1}{2}\rho_3 c_3^2 \tag{2.55}$$

Consequently, for a given stagnation pressure in the outlet of the compressor $p_3 = \Pi_c \cdot p_{amb}$ or equivalently pressure ratio Π_c and turbocharger speed N_{tc} the left hand side of Eq. 2.49 is a non-linear equation of $\dot{m}_c$.

Since both sides of the Eq. 2.49, for given pressure ratio Π_c and turbocharger speed N_{tc}, are only functions of the air mass flow $\dot{m}_c$, Eq. 2.49 can be solved iteratively in order to yield the mass flow trough the compressor $\dot{m}_c$.

However, one should take into account that the mass flow through the compressor is calculated by solving a non-linear algebraic equation. This type of algebraic loops cannot be compiled during built process into C-Language and implemented in dSPACE Rapid Prototyping Environment. Thus the compressor model, both the model of $\dot{m}_c$ and of η_{is}, should be replaced by look-up tables.

Equation 2.49 for constant pressure ratio Π_c and turbocharger speed N_{tc} may gives imaginary solutions or even two solutions. Although this problem does not appear when the compressor model is incorporated with an engine model or the real engine, it can arise when Eq. 2.49 is solved for unrelated turbocharger speeds N_{tc} and pressure ratios Π_c to derive the compressor maps in the form of $\dot{m}_c = \dot{m}_c(\Pi_c, N_{tc})$.

For this reason, the assumption that the mass flow $\dot{m}_c$ and the turbocharger speed N_{tc} are given is made and Eq. 2.49 is solved in an inverse way to compute the corresponding pressure ratio Π_c; thus, the compressor map can be derived in the form of **MODEL II**-$\Pi_c = \Pi_c(\dot{m}_c, N_{tc})$. Afterwards, only by using a simple linear interpolation

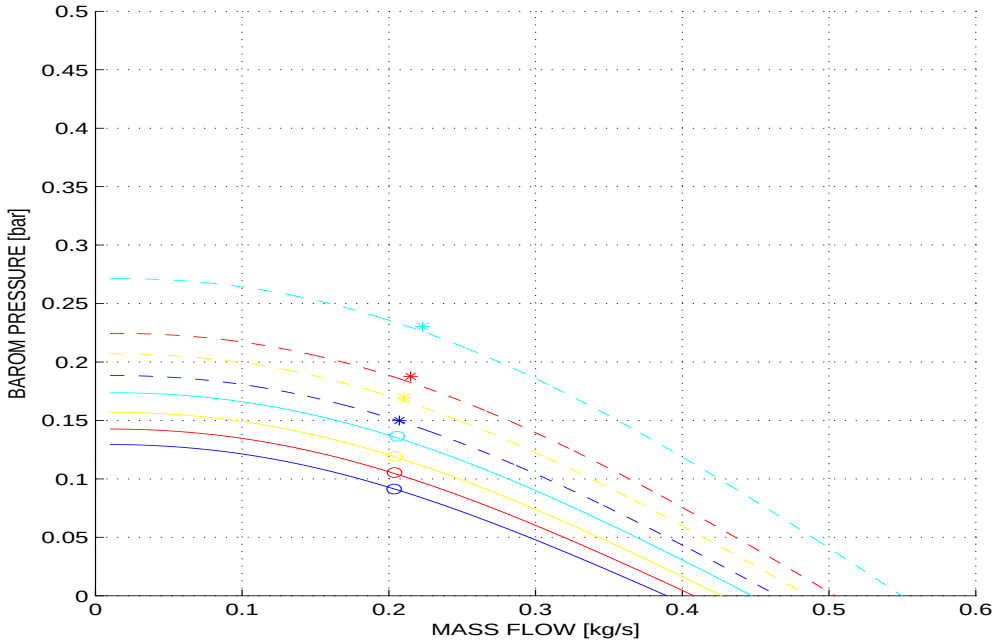

Figure 2.2: Barometric pressure at compressor outlet $(p_c - p_{amb})[bar]$ presented as a function of compressor mass flow $\dot{m}_c[kg/s]$ for different speeds of the turbocharger shaft N_{tc} in the range $[25000RPM : 35000RPM]$.

technique the corresponding value of $\dot{m}_c$ for know Π_c and N_{tc} can be computed. In this way, the desired representation is obtained, as the map is of the form $\dot{m}_c = \dot{m}_c(\Pi_c, N_{tc})$. The combinations of Π_c and N_{tc} which give a negative value of $\dot{m}_c$ are of no significance and of no effect as the connection of the engine model with the turbocharger model gives only meaningful combinations of Π_c and N_{tc} (that comply with the requirement of positive air mass flow $\dot{m}_c$ through the compressor).

One should note that the flow through the compressor chokes when the average fluid velocity within a cross section of the compressor reaches sonic conditions [11]. The chocking behaviour appears beyond the engine operation range of interest for the present application; thereby, the sonic effects are not captured by this model.

The barometric pressure at compressor outlet $(p_c - p_{amb})[bar]$ as a function of the mass flow through the compressor $\dot{m}_c[kg/s]$ for different speeds of the turbocharger shaft $N_{tc}[25000 : 35000RPM]$ along with the experimental points is depicted in Fig. 2.2. Moreover, Fig. 2.3 illustrates the isentropic efficiency η_{is} as function as the mass flow through the compressor. The speed of the turbocharger shaft N_{tc} is the parameter of the plot and lies in the range $[25000RPM : 35000RPM]$.

Compressor power

The power requested from the compressor is given by

$$P_c = \dot{m}_c c_{pa} \cdot (T_c - T_{amb}) \tag{2.56}$$

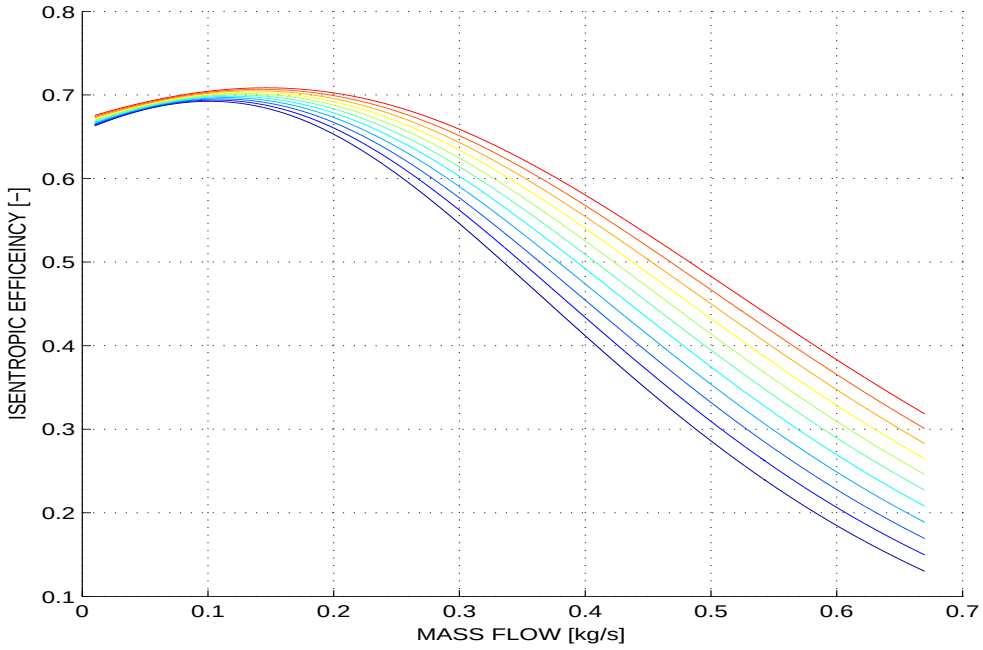

Figure 2.3: Isentropic efficiency η_{is} presented as a function of compressor mass flow $\dot{m}_c[kg/s]$ for different speeds of the turbocharger shaft N_{tc} in the range $[25000RPM : 35000RPM]$.

2.2.7 Observer and On-line Parameter Identification

General Scheme

The two differential Eqs. 2.19 and 2.20 are presented again here in one vector differential equation

$$\frac{d}{dt}\begin{pmatrix} p_{im} \\ m_{im} \end{pmatrix} = \begin{bmatrix} -\frac{\gamma V_{cyl} z N_e P(\omega_e)\theta}{120 V_{im}} & 0 \\ 0 & -\frac{\eta_v V_{cyl} z N_e}{120 V_{im}} \end{bmatrix} \cdot \begin{pmatrix} p_{im} \\ m_{im} \end{pmatrix} + \begin{bmatrix} \frac{\gamma R}{V_{im}} & 0 \\ 0 & 1 \end{bmatrix} \cdot \begin{pmatrix} \dot{m}_c T_{ac} \\ \dot{m}_c \end{pmatrix} \tag{2.57}$$

The above vector equation can be described by the generic configuration of a state space system with time-varying matrix coefficients. In other words, the system above can be written as follows

$$\frac{d\vec{x}}{dt} = A(t) \cdot \vec{x} + B(t) \cdot \vec{u} \tag{2.58}$$

where $\vec{x}$ is the states' vector, $\vec{u}$ is the inputs' vector and A(t), B(t) are the two time-varying matrices.

Only pressure in the intake manifold is available through measurement.This fact is taken into account by introducing a linear output equation

$$p_{im} = \begin{bmatrix} 1 & 0 \end{bmatrix} \cdot \begin{pmatrix} p_{im} \\ m_{im} \end{pmatrix} \tag{2.59}$$

The generic representation of the above scheme is

$$\vec{y} = C \cdot \vec{x} \tag{2.60}$$

From Eqs. 2.60 and 2.58 the following system is obtained

$$\begin{aligned} \frac{d\vec{x}}{dt} &= A(t) \cdot \vec{x} + B(t) \cdot \vec{u} \\ \vec{y} &= C \cdot \vec{x} \end{aligned} \tag{2.61}$$

The problem that arises is whether estimate an unknown state (in the present case the mass in the intake manifold m_{im}) can be estimated given only measurements of the known states (in our case the pressure in the intake manifold p_{im}).

Observability of Linear Time Varying Systems

The property of a linear system that allow us to estimate an unknown state only from measurements of another known state is called observability and the the system is called observable.

Definition 2.1. The pair of matrices $(C(\cdot), A(\cdot))$ is called observable on $[t0, t1]$ if and only if for all $x0 \in \Re^m$ and all $u : [t0, t1] \to \Re^m$, one can uniquely determine x_0 from the information of $(u(t), y(t))|t \in [t_0, t_1]$.

For the examined system it can be proved that is unobservable. In order to prove the above statement in mathematically formal way, some definitions and theorems will be presented in this section.

Let us consider the wide class of linear time varying state space systems described by the following differential equations

$$\begin{aligned} \frac{d\vec{x}}{dt} &= A(t)\cdot\vec{x} + B(t)\cdot\vec{u} \\ \vec{y} &= C\cdot\vec{x} + D\cdot\vec{u} \end{aligned} \tag{2.62}$$

The response of the system to both initial conditions and external inputs $s(t, t_0, x_0, u)$ can be partitioned into two distinct components

$$s(t, t_0, x_0, u) \quad = \quad s(t, t_0, x_0, 0) \quad + \quad s(t, t_0, 0, u) \tag{2.63}$$

where in the right part of equation, the first term is the so-called "zero input transition matrix", while the second is the so-called "zero state transition matrix". The state transition matrix is denoted as $\Phi(t, t_0)$ and is defined as

$$s(t, t_0, x_0, 0) = \Phi(t, t_0)x_0 \tag{2.64}$$

Thereby, the state transition matrix fully determines the dynamic response of the system under zero external input. For linear time-invariant system the state transition matrix can be easily derived in closed form.

Definition 2.2. Let $A(\cdot) : \Re \to \Re^{n\times n}$ be piecewise continuous function and consider the following linear ODE $\dot{x}(t) = A(t)x(t)$ .The transition matrix of the system is given by $\Phi(t, t_0) = X(t)X(t_0)^{-1}$ where $X(t)$ is the fundamental matrix so that equality $\dot{X}(t) = A(t)X(t)$ holds.

For the present system the state transition matrix is diagonal and has the following form

$$\Phi(\tau, t_0) = \begin{bmatrix} exp[\int_{t_0}^{\tau} & \phi(\xi)d\xi] & 0 \\ 0 & exp[\int_{t_0}^{\tau} & \psi(\xi)d\xi] \end{bmatrix} \tag{2.65}$$

where $\phi(\xi)$ and $\psi(\xi)$ are the diagonal elements of the state matrix $A(t)$ and as can be seen are time-varying parameters.

Definition 2.3. The observability gramian of the pair $(C(\cdot), A(\cdot))$ is the matrix

$$W_o(t_0, t_1) = \int_{t_0}^{t_1} \Phi(\tau, t_0)^T C(\tau)^T C(\tau)\Phi(\tau, t_0)d\tau \tag{2.66}$$

Theorem 2.4. *The pair of matrices $(C(\cdot), A(\cdot))$ is observable if and only if the the determinant of the observability gramian is non-zero* $\det[W_o(t_0, t_1)] \neq 0$.

Substituting element $\Phi(\tau, t_0)$ and C with their values, the result that $W_o(t_0, t_1) = 0$ is obtained. Thereby, the state m_{im} is not observable only from measurements of p_1. For this reason, the only feasible way to estimate the state m_{im} from measurements of p_1 is to construct an open loop observer. The open loop observer will be based on the

For more information about the properties of time varying systems the reader is referred to [26].

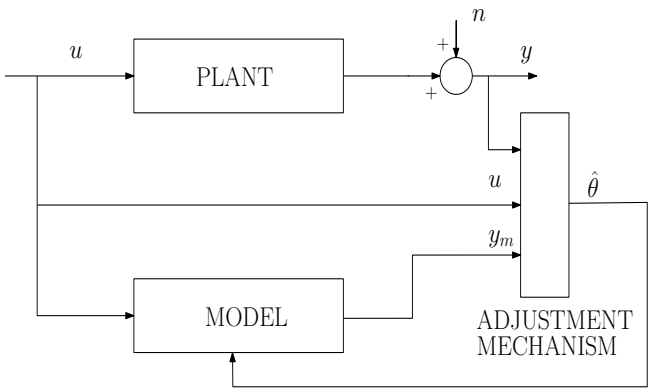

Figure 2.4: General configuration for on-line parameter identification problems.

Parameter Identifier

On-line parameter identification can be viewed and formulated as a model tracking problem (reference tracking or disturbance rejection), where the output of the model has to follow the output produced by the plant. The general configuration for identification problems is shown in Fig. 2.4. As it can be seen the input is fed to both the plant and the model. Moreover, an adjustment mechanism, using the information from the measured value and the prediction of the model, can continuously adjust the parameters of the model so that the error between the measured and the estimated value tends to zero [3].

The main focus of on-line parameter identification lies in finding the appropriate adjustment mechanism to eliminate the error between the real parameters and the identified ones. The adjustment mechanism should make the identification process robust; therefore, convergence should be guaranteed despite the presence of uncertainty of the proposed model, disturbances acting in the real plant and measurements' errors.

The differential equation of the identifier model is as follows

$$\dot{\hat{p}_1} = -\frac{\gamma V_{cyl} z N_e P(\omega_e)}{120 V_{im}} \cdot \hat{\theta(t)} \cdot \bar{p_1} + \frac{\gamma R}{V_{im}} \cdot \dot{m}_c T_{ac} \tag{2.67}$$

As shown in Eq. 2.67 the identifier model is fed with both the plant input $u = \dot{m}_c T_{ac}$ and the measured state $y = \bar{p_1}$. Furthermore, a feedback term proportional to the identification error $\bar{p_1} - \hat{p_1}$ is included in the state space Eq. 2.67, on the grounds that parameter identification is conceptually a reference tracking problem of the signal $\bar{p_1}$. The final differential equation is the following

$$\dot{\hat{p}_1} = -\frac{\gamma V_{cyl} z N_e P(\omega_e)}{120 V_{im}} \cdot \hat{\theta(t)} \cdot \bar{p_1} + \frac{\gamma R}{V_{im}} \cdot \dot{m}_c T_{ac} + g_p \cdot (\bar{p_1} - \hat{p_1}) \tag{2.68}$$

Adding this term servers to prevent constant disturbances in the measured pressure to destabilize the adaptive observer when they are integrated over a wide time interval.

In this point it worth noting that not all types of inputs guarantee the convergence of the estimated parameter to that of the real plant. Exponentially fast convergence of the estimated parameters to those of the real plant is achieved if and only if the system's input $u(t)$ is persistently exciting [16].

Definition 2.5. A signal $u(t)$ is called persistently exciting if

$$\int_t^{t+T} u^2(\tau)d\tau \geq a_0 T \tag{2.69}$$

for every T, where a_0 is a positive constant in the equation above.

The main objective is to find an identification error that is implementable and guarantee convergence to the real parameter. The basis of the analysis is Eq. 2.21. Every side of Eq. 2.21 is filtered so the derivatives that appear on the left side are realizable. The derivatives are not realizable since, theoretically, they cannot be calculated only with present and past values of the measured signal. Practically, derivative terms can be approximately evaluated numerically but this results in the introduction of noise. This problem can be suppressed by passing the signal through a low pass band filter. Filtering both sides of Eq. 2.21 yields

$$H_{fd}(p_{im}) = \frac{\gamma R}{V_{im}} \cdot H_{fi}(\dot{m}_c T_{ac}) - \frac{\gamma V_{cyl} z}{120 V_{im}} \cdot H_{fi}(N_e P(\omega_e)\theta p_{im}) \tag{2.70}$$

Defining the regress-or

$$\bar{\phi}(t) = -[\frac{\gamma V_{cyl} z}{120 V_{im}} \cdot H_{fi}(N_e P(\omega_e)\theta \bar{p_{im}})] \tag{2.71}$$

and the corresponding signal

$$z = \bar{\phi}\theta \tag{2.72}$$

which satisfies the fundamental property of being persistently exciting and, consequently, can be used for the on-line parameter estimation. The error signal is then given by

$$\epsilon = z(t) - \hat{z}(t) = \bar{\phi}\theta - \bar{\phi}\hat{\theta} = ...\text{Cumbersome algebra}... = \bar{\phi}\tilde{\theta} - \epsilon_{res} \tag{2.73}$$

where $\tilde{\theta}$ is the error in the estimated parameter. As can be seen from Eq. 2.73 the identification error is a linear function of the parameter error. If the identification error is written as a function of the measured and estimated variables and eliminate the terms that cause bias the following implementable identification error can be derived

$$\epsilon = z(t) - \hat{z}(t) = ...\text{Cumbersome algebra}... = [(H_{df} + g_{p1} H_{fi})(\bar{p}_{im} - \hat{p}_{im})] \tag{2.74}$$

Finally, the choice of an appropriate adaptation law needs to be made. A through presentation of the various types of adaptation laws is given in [16]. The adaptation law that is used is a piecewise function of the estimated volumetric efficiency $\hat{\eta_v}$ as follows

$$\dot{\hat{\theta}} = \begin{cases} (\Gamma + P)\bar{\phi}(t)\bar{\epsilon}(t) & for \quad \hat{\eta_v} \in S_\eta \\ 0 & for \quad \hat{\eta_v} \ni S_\eta \end{cases} \tag{2.75}$$

where

$$\dot{P} = \begin{cases} P^2\bar{\phi}^2 & for \quad \hat{\eta_v} \in S_\eta \\ 0 & for \quad \hat{\eta_v} \ni S_\eta \end{cases} \tag{2.76}$$

This adaptation law is a hybrid version that combines traditional least squares algorithm, projection and covariance resetting. In this way, the use of covariance resetting guarantees that the covariance matrix P will not become singular and the use of projection ensures that the value of η_v is within the physical limits (typically $\eta_v \in [0.5, 1]$ but the upper bound for Diesel Engines can be even higher due to the scavenge air $\eta_v = 1.1$).

2.3 Fuel Path Modelling

2.3.1 Willan's Model

The torque produced by the engine is a complex function of many variables, such as the fuel mass in the cylinder, the air to fuel ratio, the engine's speed, the injection timing, etc [13].

$$M_e = f(\dot{m}_f, \lambda, N_e, \zeta, ...) \tag{2.77}$$

Only with detailed thermodynamic simulations accurate prediction of the produced torque by the internal combustion engine is possible. However, for control purposes such simulations are too time-consuming and unnecessary, since lower accuracy in the estimated torque is also acceptable for the majority of control problems. For this reason, the engine is approximated as a Willans machine. Precisely, the engine is just an energy converter which converts the available input power W_{in} ($W_{in} = \dot{m}_f H_{LV}$) into output power W_{out} ($W_{out} = \omega_e M_e$) and effort variables [36]. For each time instant, the following equation holds

$$\omega_e \cdot M_e = \eta \cdot \dot{m}_f H_{LV} \tag{2.78}$$

where ω_e is the engine's speed in rad/s, η is the engine's efficiency and H_{LV} is the fuel's lower calorific value of the fuel.

To derive a simple equation, the assumption that an affine relation between the produced torque and the mass of fuel burned exists

$$M_e = \frac{ew(\omega_e) \cdot \dot{m}_f \cdot H_{LV}}{\omega_e} - M_{loss}(\omega_e) \tag{2.79}$$

In Eq. 2.79, e is only the thermodynamic efficiency of the engine, while in Eq. 2.78, η also incorporates friction losses and other mechanical losses of the engine.

The equation above depends on quantities that are associated with engine size. This dependency can be eliminated by introducing dimensionless variables which are defined as follows

$$p_{me} = \frac{4\pi}{V_{cyl}} \cdot M_e \tag{2.80}$$

$$p_{mf} = \frac{4\pi \cdot H_{LV} \cdot \dot{m}_f}{V_{cyl} \cdot \omega_e} \tag{2.81}$$

$$p_{mloss} = \frac{4\pi}{V_{cyl}} \cdot M_{loss} \tag{2.82}$$

and

$$c_m = \frac{S \cdot \omega_e}{\pi} \tag{2.83}$$

where S is the engine's stroke. The variable p_{mf} is the available mean effective pressure and p_{me} is the produced mean effective pressure. Equation 2.79 can be written in terms of the previously defined dimensionless variables as follows

$$p_{me} = ew(c_m) \cdot p_{mf} - p_{ml}(c_m) \tag{2.84}$$

which is the equation that will be used for the linear regression in order to calculate the coefficients ew and p_{ml}. It is worth noting that these two coefficients are primarily functions of the engine speed.

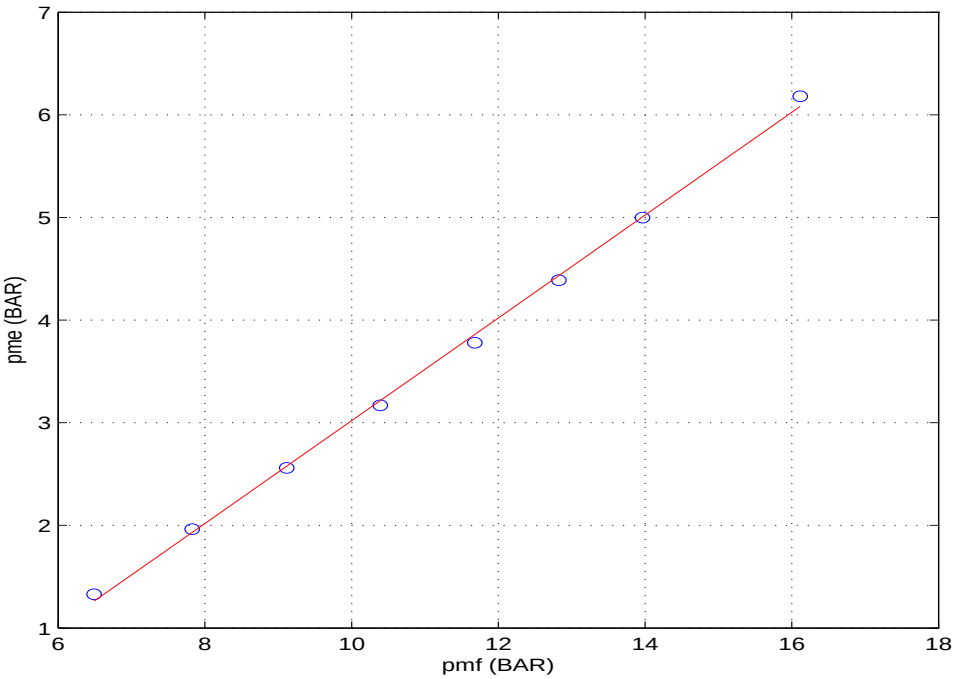

Figure 2.5: Linear regression of experimental data for Willan's relation.

Figure 2.5 illustrates the experimental data of the mean effective fuel pressure and mean effective pressure along with a line calculated using the least squares fit method for engine speed N_e = 1600 RPM.

In order to capture the reciprocating behaviour of the engine delays should be introduced between the cylinder-in and cylinder-out events. For instance, the injected fuel affects the torque produced only after the injection to power cycle. The torque produced at the time instant t is given by

$$M_e(t) = \frac{ew \cdot \dot{m}_f(t - \tau_{inj \to PC})}{\omega_e(t)} \cdot H_{LV} - M_{loss} \tag{2.85}$$

2.3.2 Inverse Willan's Model

Equation 2.85 shall be written in the following way

$$\dot{m}_f(t - \tau_{inj \to PC}) = \frac{\omega_e(t) \cdot (M_e(t) + M_{loss})}{H_{LV} \cdot ew} \tag{2.86}$$

Equation 2.86, if all terms are moved by $\tau_{inj \to PC}$, can be written as

$$\dot{m}_f(t) = \frac{\omega_e(t + \tau_{inj \to PC}) \cdot (M_e(t + \tau_{inj \to PC}) + M_{loss})}{H_{LV} \cdot ew} \tag{2.87}$$

The terms that appear in the right hand side of Eq. 2.87 are not realizable. In order to evaluate the mass of fuel at the time instant "t", measurements of the torque produced and the rotational speed of the engine at time instant "$t + \tau_{inj\to PC}$" are required.

From now on the assumption that the torque produced at the time instant $t+\tau_{inj\to PC}$ equals the torque produced at time instant t plus the inertial term $J_e\frac{d\omega_e}{dt}$ at the same time instant is made; thus, the following equation is obtained

$$M_e(t + \tau_{inj\to PC}) = M_e(t) + J_e\frac{d\omega_e}{dt}(t) \tag{2.88}$$

This approximation is introduced now but it will be shown a-posteri that is a reasonable approximation from the agreement between the proposed model and the experimental data. Moreover, engine's speed at time instant $t + t_{inj\to PC}$ can be replaced from the corresponding first order approximation

$$\omega_e(t + \tau_{inj\to PC}) = \omega_e(t) + \frac{d\omega_e}{dt}(t)\cdot\tau_{inj\to PC} \tag{2.89}$$

The term $M_e(t+\tau_{inj\to PC})$ can be substituted from Eq. 2.88 and the term $\omega_e(t+\tau_{inj\to PC})$ from Eq. 2.89; It follows from these two substitutions that

$$\dot{m_f} = \frac{[\omega_e + \frac{d\omega_e}{dt}\cdot\tau_{inj\to PC}]\cdot[M_e + J_e\frac{d\omega_e}{dt} + M_{loss}]}{H_{LV}\cdot ew} \tag{2.90}$$

where all the time dependant variables in Eq. 3.21 refer to time instant t.

The problem associated with the realisability of the right hand side of Eq. 2.87 still appears in Eq. 3.21 due to the presence of derivatives. However, in Eq. 3.21 derivatives can be approximately estimated from past data.

The disadvantage of approximating derivatives is the fact that noise is introduced into the system. The effect of noise can be suppressed by passing the derivatives through a low pass filter. Nevertheless, filtering of the measurements can be a source of delay. For this reason, a right balance should be found between the delay introduced and the noise presented in the estimated value of λ.

2.4 Lambda estimation

2.4.1 Estimation of AFRst

From the stoichiometric analysis of the the fuel, the following data were obtained

Table 2.1: Fuel Analysis Data

Lowest Calorific Value	10378	$kcal/kg$
Carbon	86.624	$[\%]\cdot m_{f,tot}$
Hydrogen	13.37	$[\%]\cdot m_{f,tot}$
Sulphur	0.0022	$[\%]\cdot m_{f,tot}$
Nitrogen	0.0014	$[\%]\cdot m_{f,tot}$

As illustrated in Table 2.1 the main chemical substances in the fuel used are Carbon and Hydrogen, the other two substances that correspond to small ratios of the total

mass of fuel will be ignored. A general hydrogen fuel of molecular composition C_aH_b is considered here. The parameter a is obtained by

$$a[kmC/KgF] = \frac{[KgC/KgF]}{M_C[kgC/kmC]} = 0.07214 \tag{2.91}$$

and, similarly, parameter b is given by

$$b[kmH/KgF] = \frac{[kmH/KgF]}{M_H[kgH/kmH]} = 0.13264 \tag{2.92}$$

The value of AFR_{st} can be evaluated as a function of $y = b/a = 1.83864$ from the formula presented in [14]

$$AFR_{st} = \frac{34.56 \cdot (4+y)}{12.011 + 1.008 \cdot y} = 14.554 \tag{2.93}$$

2.4.2 In-cylinder gas mixing

At each time instant the value of lambda λ for the fresh charge mixture of air and fuel is given by:

$$\lambda = \frac{AFR}{AFR_{st}} = \frac{\dot{m}_e/\dot{m}_f}{AFR_{st}} \tag{2.94}$$

A considerable part of the exhaust gases remains inside the cylinder and is mixed with the fresh air charge. The final value of $\lambda(t)$ would be a weighted average of $\lambda(t-\tau_{ieg})$ which is the value of λ for the previous cycle and of $\lambda_{fc}(t)$ which is the value of λ for the new air that is aspirated inside the cylinder. The following relationship is derived

$$\lambda(t) = \frac{\lambda(t-\tau_{ieg}) \cdot m_{res}(t) + \lambda_{fc}(t) \cdot [m_e(t) + m_f(t)]}{m_e(t) + m_f(t) + m_{res}(t)} \tag{2.95}$$

where all the masses in the equation above can be calculated from the corresponding mass flows using the integration formula as follows

$$m(t) = \dot{m}(t-\tau_{ieg}) \cdot \tau_{seg} \tag{2.96}$$

where the time period for integration is the time interval between induction and exhaust cycle

$$\tau_{seg} = \frac{2\pi \cdot 2}{\omega_e \cdot z} \tag{2.97}$$

2.5 Delays Computation

In the present thesis a mean value approach is adopted; thus, the reciprocating behaviour of the engine can only be captured by introducing delays between cylinder-in and cylinder-out events. Moreover, delays have to be introduced between the inlet and outlet of air ducts and air coolers. Although this approach is usually sufficient for relative slow processes, it is weak in capturing really fast variations in lambda λ. In the latter case discrete event modelling can be adopted.

In the experimental set-up of the LME, the barometric pressure in the air cooler outlet p_{im} and the turbocharger's shaft speed N_{tc} are measured. In this way an estimate of the air mass flow through the compressor can be obtained by using the compressor

maps that provide $\dot{m}_c$ as function of the above parameters. It is assumed that these two variables are measured in the time instant "t".

Air from the turbocharger is delivered through the air pipe to the air cooler. The average fluid velocity in the air pipe from compressor outlet up to the air cooler inlet is given by Eq. 2.10 and the time needed for the fluid to travel along the pipe that connects the compressor outlet with the air cooler inlet can be calculated by

$$\tau_{ad} = \frac{L_{ad}}{c_3} \tag{2.98}$$

Proceeding analogously to derive the time delay due to the presence of the air cooler, the formula that can be used is

$$\tau_{ac} = \frac{L_{ac} \cdot A_{ac} \cdot \rho_{av}}{\dot{m}_c} \tag{2.99}$$

In order to calculate the air cooler delay the geometric features of the air cooler and especially the effective cross sectional area A_{ac} have to be known. In Eq. 2.99, ρ_{av} is the mean density between the inlet and outlet of the air cooler $\rho_{av} = \frac{1}{2} \cdot (\rho_{ac^+} + \rho_3)$.

Moreover, the air in the intake manifold will only enter the engine during the intake stroke of one of the cylinders. For an one-cylinder engine the induction stroke is repeated approximately every $360^o + 180^o$ of the crank shaft angle. For an engine with z number of cylinders the induction stroke is repeated every $(360^o + 180^o)/z$ of the crank shaft angle. To convert crank-angle to time delay, with known engine speed, the following relationship is used

$$dt = \frac{d\phi(deg)}{360 \cdot \omega_e} \tag{2.100}$$

So the maximum inlet to induction delay can be calculated as follows

$$\tau_{inl \to ind} = \frac{3/2}{\omega_e \cdot z} \tag{2.101}$$

2.6 Virtual Sensor Model Simulation

The differential and algebraic equations that were presented in this chapter were implement in a MATLAB/Simulink model. The structure of this model is depicted in Fig. 2.1 where each block corresponds to a MATLAB/Simulink subsystem. The model was tested on-line and the measurements of the physical sensor were compared with the estimations provided by the virtual sensor. Precisely, two experiments were carried out at the LME to verify the accuracy of the proposed virtual sensor model.

In the first experiment the engine was running at approximately constant speed $N_e = 1600RPM$ and the torque produced by the ICE was as illustrated in Fig. 2.6. The measurements of N_{tc}, N_e, T_e and p_{im} were provided to the virtual sensor on-line with both the estimated and the measured values of λ being recorded.

From the experimental results, depicted in Fig. 2.8, it is shown that the steady state error is less than 0.2 for the various loads that were applied. The developed model can sufficiently capture the dynamic behaviour of the measured value of lambda

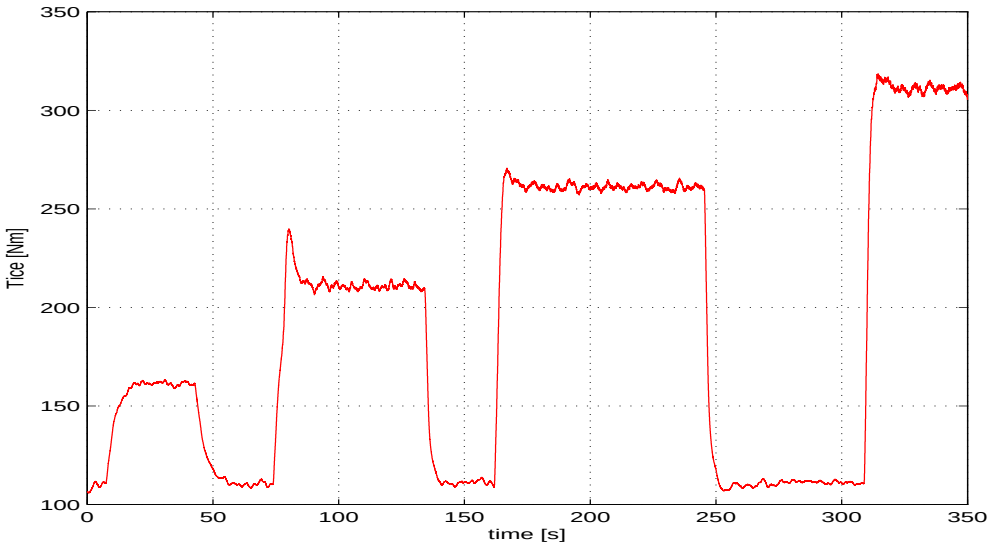

Figure 2.6: Torque probuced by the ICE-T_e for a step load.

during load increase transients. At the same time, the undesirable spikes of the physical sensor measurements during load reductions are not reproduced by the virtual sensor.

On the other hand, it should be mentioned that no significant benefit from measurement delay reduction is noticed with the implementation of the virtual sensor. Additionally, noise is presented in the estimated value of λ from the virtual sensor. The noise steams from the way in which the non-realisable derivative term is computed and from the high-frequency torque variations. The effect of noise can be eliminated by applying filtering to the derivative term but, in this way, additional time delay is induced in the estimation of λ. Clearly, a trade-off between the smoothness of the estimated data and the speed of measurement exists.

In the second experiment, a propeller load demand was applied to the ICE with the characteristics that are given in Fig. 2.7. As illustrated in Fig. 2.9, the measured and the estimated value of λ match well over the whole time interval presented in the figure with the maximum deviation between them being less than 0.25.

Finally, a conclusion that can be drawn from the comparison of Figs. 2.8 and 2.9 is that the measured and the estimated values of λ are close to one another in quasi-static loading and very slow transients. Thus, no need is presented to replace the physical sensor with the virtual one in this case of loading. On the contrary, the use of the virtual sensor may be proved beneficial in fast load transients when an accurate measurement of λ is essential.

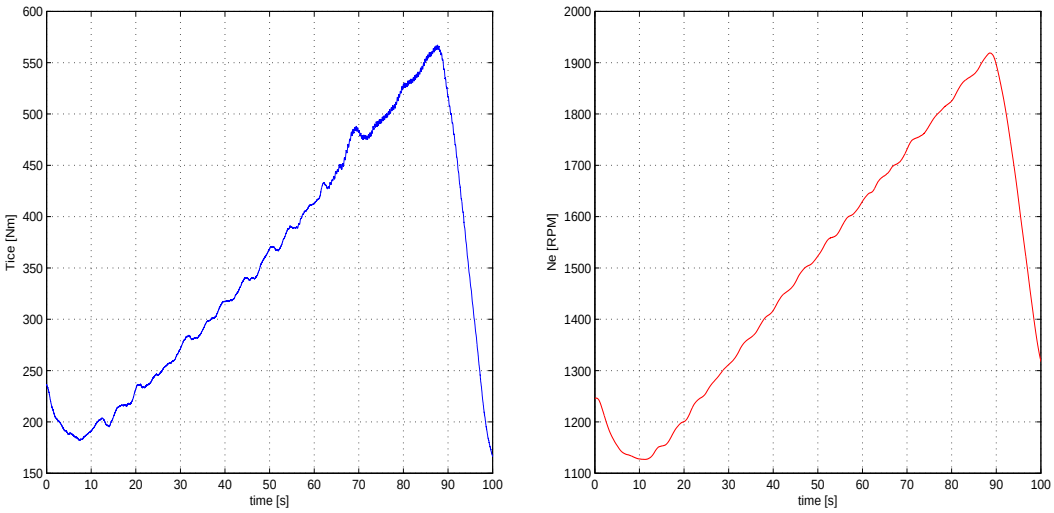

(a) Torque probuced by the ICE-T_e. (b) Engine rotational speed-N_e.

Figure 2.7: Propeller load characteristics.

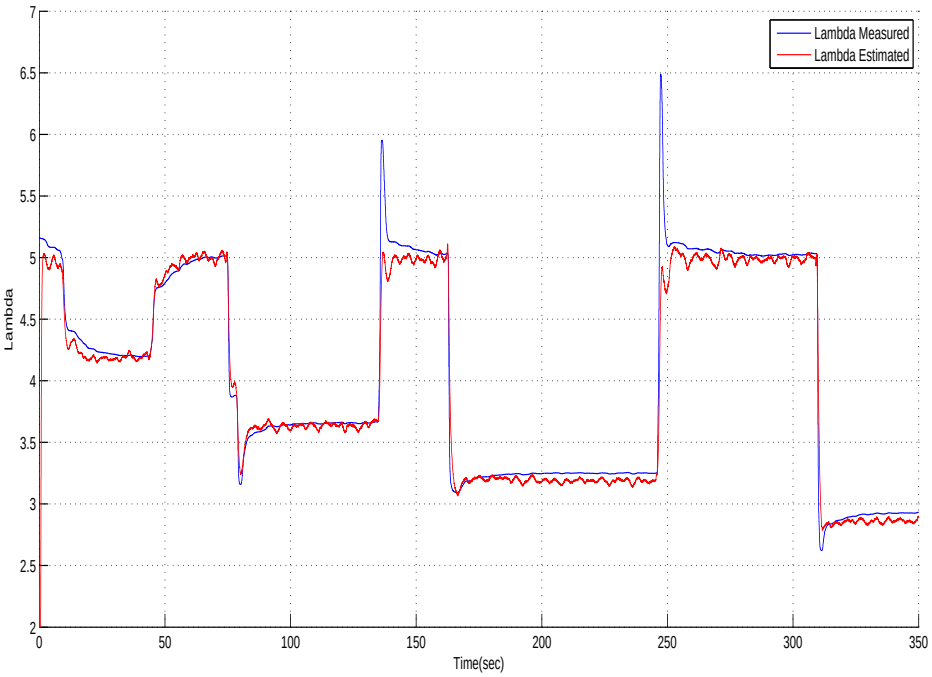

Figure 2.8: Measured and estimated value of lambda for a step load.

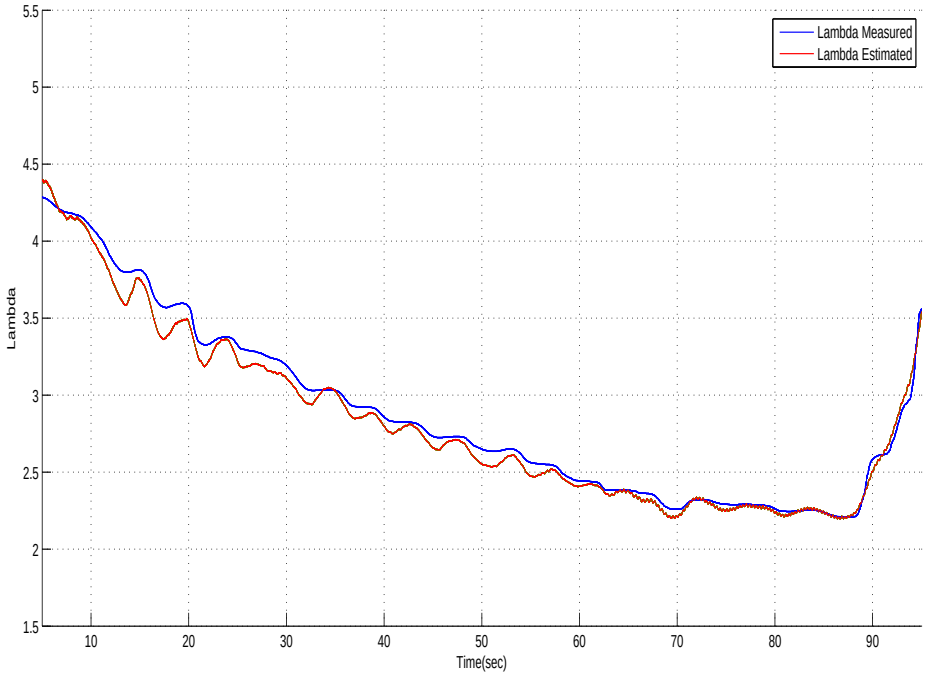

Figure 2.9: Measured and estimated value of lambda for a propeller load.

Chapter 3

Dynamic Uncertain Non-Linear Model of Lambda

In the process of controlling the value of λ for the hybrid power-train, the ICE has to be modelled. The model which will be derived has to sufficiently describe the variations of λ during transient conditions but simultaneously be of low order and use only the measured input variables, since it is oriented for a control application. All the components of the engine are modelled using a Mean Value Approach. The final model will have as output the value of λ and as input the fuel mass flow $\dot{m}_f$; the rotational speed of the engine N_e is considered as a fixed parameter. After the ICE engine model has been developed, the other components of the hybrid-electric powertrain are modelled as well and the final linearised model is computed in Chap. 5. Figure 3.1 presents the whole structure of the hybrid-electric powertrain, while the schematic representation of the ICE model with its corresponding components is illustrated in Fig. 3.2.

The Compressor, Air Cooler, Engine and Intake Manifold have already been modelled in Chap. 2, as they were integrated parts of the virtual sensor model. Unlike the previous chapter, where use of the measured turbocharger speed and pressure in the intake manifold has been made, in this section, the proposed model simulates this physical variables since they correspond to internal states of the model.

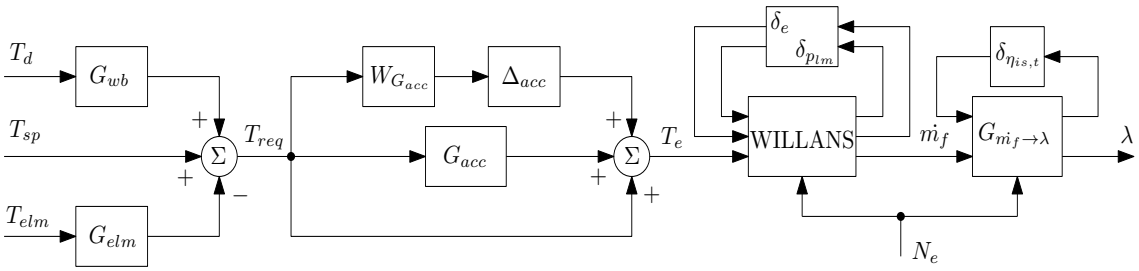

Figure 3.1: Hybrid power-train block diagram.

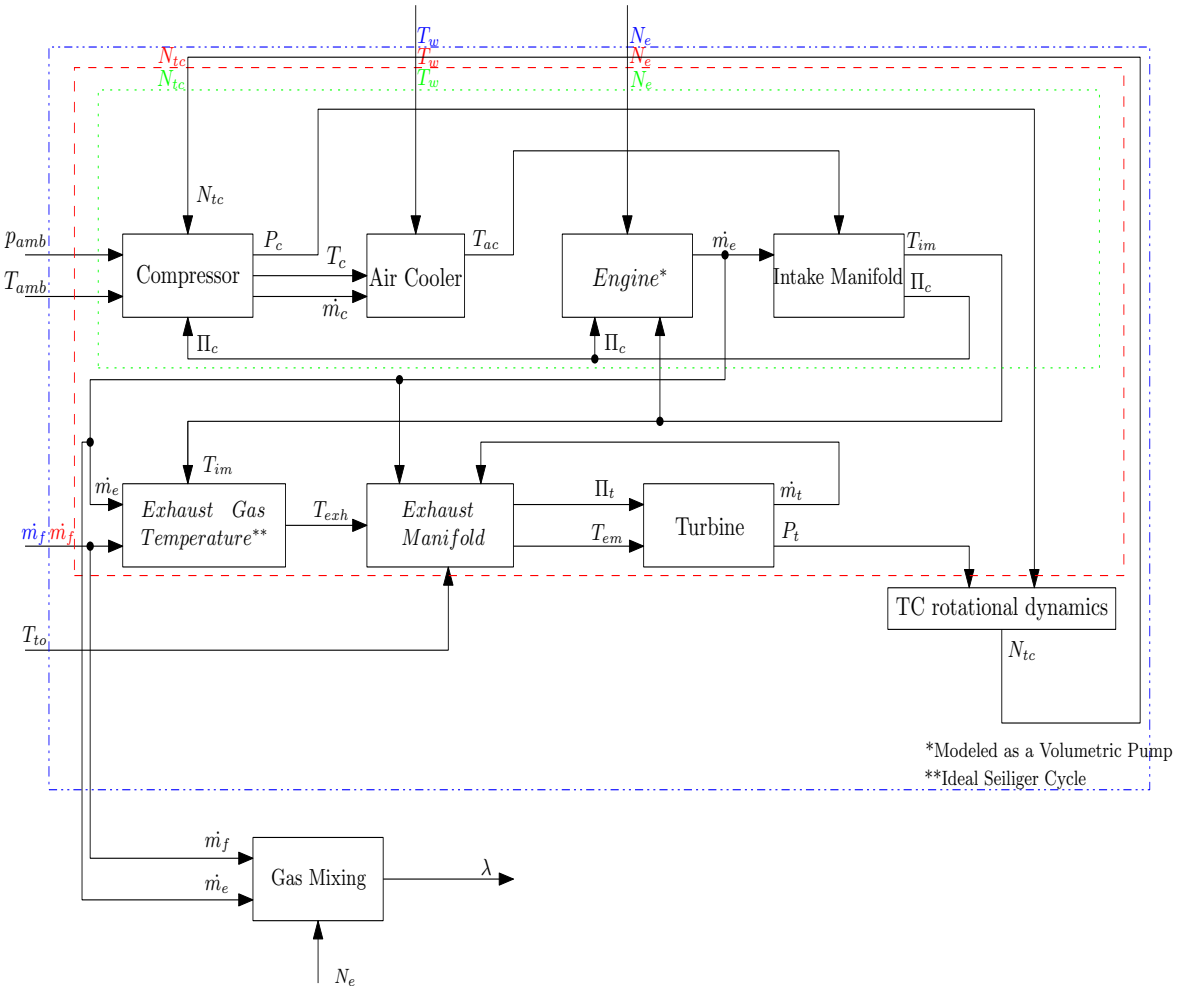

Figure 3.2: ICE model block diagram.

3.1 Exhaust gas temperature

The real thermodynamic processes in the cylinder can be approximated by an ideal Seiliger cycle [47]. Under this simplification the exhaust gas temperature immediately after the exhaust valve is given by

$$T_{exh} = \eta_{sc}\Pi_e^{1-1/\gamma_g} r_c^{1-\gamma_g} x_p^{1/\gamma_g - 1}\left(q_{in}\left(\frac{1-x_{cv}}{c_{pg}} + \frac{x_{cv}}{c_{vg}}\right) + T_{im} r_c^{\gamma_g - 1}\right) \tag{3.1}$$

where

$$q_{in} = \frac{\dot{m}_f H_{LV}}{\dot{m}_f + \dot{m}_e} \tag{3.2}$$

and

$$x_p = 1 + \frac{q_{in} x_{cv}}{c_{va} T_{im} r_c^{\gamma - 1}} \tag{3.3}$$

The exhaust temperature model has two tunable parameters η_{sc} and x_{cv}.

3.2 Turbine Model

3.2.1 Turbine Mass Flow

It has become clear from Subsection 2.2.6 that the mass flow delivered from the compressor is as a combined result of both the pressure ratio Π_c and the turbocharger rotational speed N_{tc}. Unlike the compressor, turbine drives air through it mainly due to the pressure ratio Π_t and not the turbocharger rotational speed N_{tc}. Therefore, simplifying turbine's behaviour with this of a non-linear orifice is a reasonable approximation that reduces complexity and is suitable for control applications [13].

The flow equation for a turbine is

$$\dot{m}_t = cA_t \frac{p_{em}}{\sqrt{R_g T_{em}}} \Psi(1/\Pi_t) \tag{3.4}$$

where cA_t is the effective flow area, R_g is an ideal gas constant for the exhaust gas, p_{em} and T_{em} are the pressure and temperature in the exhaust manifold, respectively. The term $\Psi(1/\Pi_t)$ is a piecewise function given by

$$\Psi(1/\Pi_t) = \begin{cases} (1/\Pi_t)^{\frac{1}{\gamma_g}} \sqrt{\frac{2\gamma_g}{\gamma_g - 1}\left[1 - (1/\Pi_t)^{\frac{\gamma_g}{\gamma_g - 1}}\right]} & for \quad \Pi_t \le \left(\frac{\gamma_g + 1}{2}\right)^{\frac{\gamma_g}{\gamma_g - 1}} \\ \sqrt{\gamma_g \left(\frac{2}{\gamma_g + 1}\right)^{\frac{\gamma_g + 1}{\gamma_g - 1}}} & for \quad \Pi_t > \left(\frac{\gamma_g + 1}{2}\right)^{\frac{\gamma_g}{\gamma_g - 1}} \end{cases} \tag{3.5}$$

The throttle Eq. 3.5 suggests a chocking behaviour above the critical pressure ratio $\Pi_{t,cr} \approx 2$. This behaviour does not usually accords with the experimental data. For this reason, many models have been proposed so that the actual behaviour is captured. A comparison of three of the most common models which are used is presented in [17]. These models have unknown tunable parameters which can be estimated when the model is fitted to the data provided by the manufacturer. A very flexible and mathematically compact model, which can capture the behaviour of the turbine, is the following:

$$\dot{m}_t = \frac{p_{em}}{\sqrt{T_{em}}} \Phi(\Pi_t) \tag{3.6}$$

where $\Phi(1/\Pi_t)$ is a function given by

$$\Phi(\Pi_t) = c_t \cdot \sqrt{1 - (\Pi_t)^{-k_t}} \tag{3.7}$$

In the above equation the constants c_t and k_t are two tunable parameters, which can be identified so the final model agrees with the turbine's map provided by the manufacturer or the experimental data.

3.2.2 Turbine's Isentropic Efficiency

In Subsection 3.2.1 the mass flow through the turbine $\dot{m}_t$ was assumed independent of the turbocharger speed N_{tc}. However, this assumption does not hold for the turbine's is-entropic efficiency which depends on the incidence of the incoming exhaust gas and, as a result, the turbocharger speed N_{tc}. Turbine's efficiency can be represented in a dimensionless map as a function of the "turbine blade speed ratio" $\tilde{c_u}$ and the pressure ratio Π_t. The "turbine blade speed" ratio is defined in [13] and given by the following formula

$$\tilde{c_u} = \frac{D_t \cdot \omega_{tc}}{c_{us}} \tag{3.8}$$

where

$$c_u = \sqrt{2c_{pg} \cdot T_{em}[1 - \Pi_t^{(1-\gamma_g)/\gamma_g}]} \tag{3.9}$$

The is-entropic efficiency of the turbine $\eta_{is,t}$ can be very well approximated by a quadratic function of the form

$$\eta_{is,t}(\tilde{c_u}) = \eta_{is,t,max} \cdot [\frac{2\tilde{c_u}}{\tilde{c_{u,opt}}} - (\frac{\tilde{c_u}}{\tilde{c_{u,opt}}})^2] \tag{3.10}$$

The parameters $\eta_{is,t,max}$ and $c_{u,opt}$ can be chosen in an appropriate way to fit the data provided by the manufacturer.

3.2.3 Turbine Power

The power delivered by the turbine is given by

$$P_t = \dot{m}_t \cdot c_{pg} \cdot T_{em} \cdot (1 - \frac{T_{to}}{T_{em}}) \tag{3.11}$$

where $\dot{m}_t$ is the mass flow through the turbine, T_{em} is the exhaust manifold temperature that is equal to the exhaust gas temperature at the inlet of the turbine and T_{to} is the temperature at the outlet of the turbine. Additionally, using the relationship of an non-isentropic expansion between the temperatures T_{to} and T_{em}, the ratio T_{to}/T_{em} is given by

$$1 - \frac{T_{to}}{T_{em}} = \eta_{is,t}(1 - \Pi_t^{\frac{1-\gamma_g}{\gamma_g}}) \tag{3.12}$$

Substituting Eq. 3.12 into Eq. 3.11 yields

$$P_t = \dot{m}_t \cdot c_{pg} \cdot T_{em} \cdot \eta_{is,t} \cdot (1 - \Pi_t^{\frac{1-\gamma_g}{\gamma_g}}) \tag{3.13}$$

3.3 Exhaust manifold model

The exhaust manifold is modelled similar to the intake manifold case as described in Subsection 2.2.1. Using the conservation of mass principle and the energy balance the following differential equations can be obtained

$$\frac{m_{em}}{dt} = \dot{m}_e + \dot{m}_f - \dot{m}_t \tag{3.14}$$

and

$$\frac{dp_{em}}{dt} = \frac{\gamma_g R_g}{V_{im}} \cdot (\dot{m}_e + \dot{m}_f) \cdot T_{exh} - \frac{\gamma_g R_g}{V_{em}} \cdot \dot{m}_t \cdot T_{em} - \dot{Q}_{em} \tag{3.15}$$

where $\dot{Q}_{em}$ is the heat transfer that takes place in the exhaust manifold and V_{em} is the volume of the exhaust manifold. Finally, from the ideal gas law the following equation is valid

$$m_{em} T_{em} = \frac{p_{em} V_{em}}{R_g} \tag{3.16}$$

3.4 Turbocharger Rotational Dynamics

The rotational speed of the turbocharger shaft w_{tc} can be derived from a power balance between the power delivered by the turbine P_t and the power absorbed by the compressor P_c. The power balance yields the following differential equation

$$\frac{d}{dt}(\frac{1}{2} J_{tc} w_{tc}^2) = P_t - P_c \tag{3.17}$$

where J_{tc} is the turbocharger's shaft inertia and w_{tc} is the rotational speed of the turbocharger shaft expressed in rad/sec.

Equation 3.17 can also be written as

$$J_{tc} \cdot \frac{d}{dt}(w_{tc}) = M_t - M_c \tag{3.18}$$

where M_t and M_c are the torque produced by the turbine and the torque request from the compressor respectively.

3.5 Engine Rotational Dynamics

Using the second law of Newton on rotational motion, the following differential equation can be obtained

$$J_e \frac{d\omega_e}{dt} = M_e - M_{req} \tag{3.19}$$

The kinetic energy is stored mainly in the engine's flywheel, since it accounts for most of the rotational inertia of the engine.

If the acceleration of the engine and the requested torque was known, then the torque produced by the engine could be very easily calculated from equation 3.19.

3.6 Fuel Mass Flow Model

In Subsection 2.3.2the following equation was otained

$$\dot{m_f} = \frac{\left[\omega_e + \frac{d\omega_e}{dt} \cdot \tau_{inj \to PC}\right] \cdot \left[M_e + J_e \frac{d\omega_e}{dt} + M_{loss}\right]}{H_{LV} \cdot e} \tag{3.20}$$

Substituting Eq. 3.19 into Eq. 3.20 yields

$$\dot{m_f} = \frac{\left[\omega_e + \frac{d\omega_e}{dt} \cdot \tau_{inj \to PC}\right] \cdot \left[M_{req} + 2 \cdot J_e \frac{d\omega_e}{dt} + M_{loss}\right]}{H_{LV} \cdot ew} \tag{3.21}$$

which is the equation that will be used to derive the fuel mass flow $\dot{m_f}$ inside the cylinder.

3.7 Electric Motor Identification

Unlike the components of the internal combustion engine, where a first-principles approach is adopted, the model of the electric motor is derived with the aid of identification theory. In this way, no prior knowledge of the state space equations that describe the system is necessary.

Ljung in [23] defined system identification as the art and science of building mathematical models of dynamic systems from observed input-output data. Additionally, as can be seen from Fig. 3.3, system identification is an iterative procedure and the identification process steps possess a natural logical sequence.

3.7.1 Step No1: Experiment Design

The input-output data are collected in a specified experimental set-up, appropriately designed by the user to maximize the information which can derived for the identified models. A crucial decision that has to be made in terms of the identification process concerns the type of the input signal that will be used in the experiment.

The identification experiment has to distinguish different models in the set of all the possible possible models which can be obtained. Ljung in [22] refers the class of identification experiments that acquire this property as informative and formulates mathematically this property as follows.

Theorem 3.1. *If an unspecified model set of single-input single-output linear models is defined as*

$$M^\star = \{G(s,\theta), H(s,\theta) | \theta \in D_M\} \tag{3.22}$$

where G is the model of the plant to be identified, H is the model of the noise and D_M is the set where the parameters of the family of models, then the necessary and sufficient condition for informative experiment is

$$|\Delta G(e^{i\omega})|^2 \Phi(\omega) \equiv 0 \tag{3.23}$$

where ΔG is the difference between two identified models and $\Phi(\omega)$ is the spectrum of the input signal.

Signals with this property are called **persistently exciting**. Additionally the following definition broadens the concept of persistently exciting signals

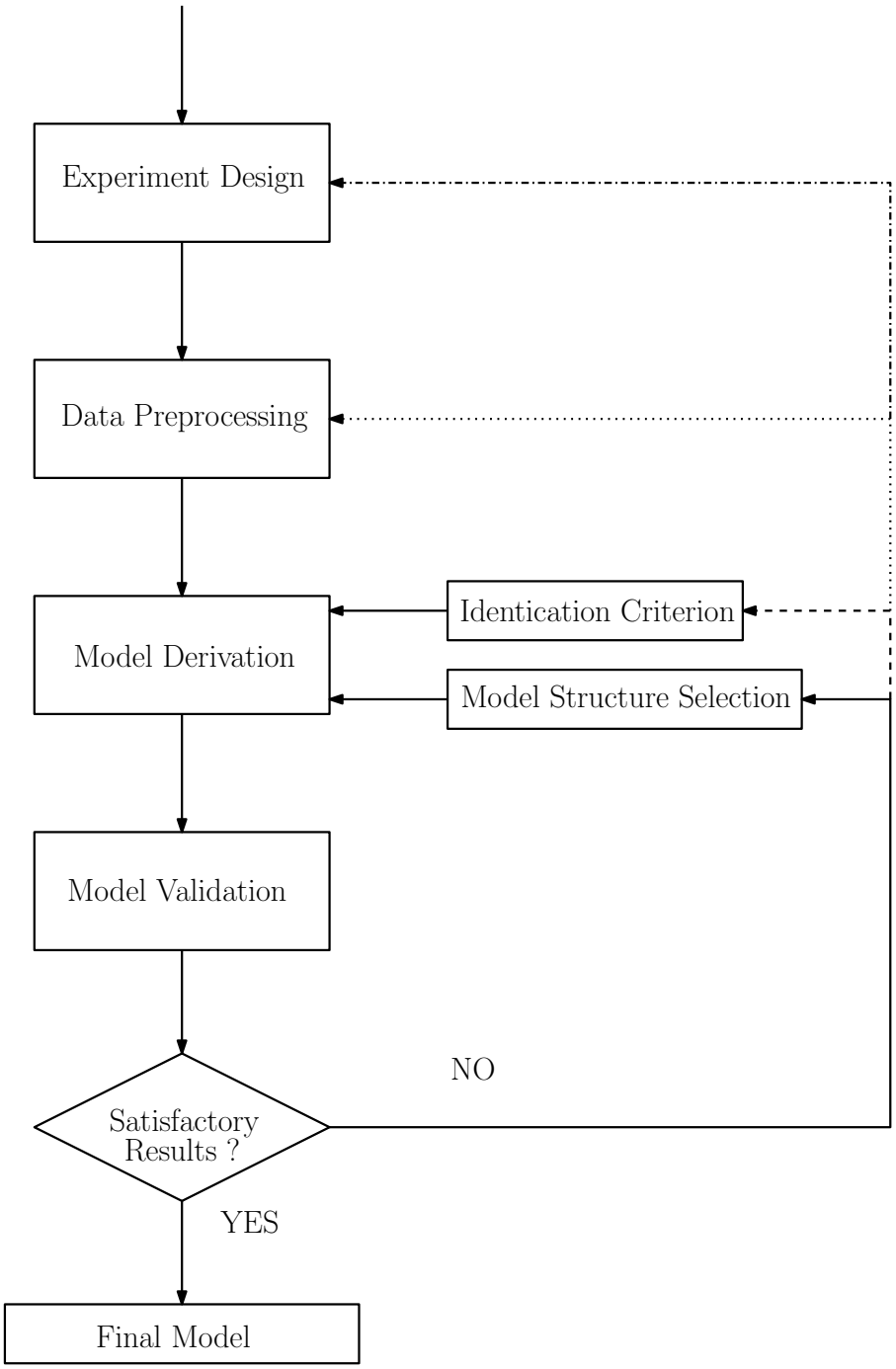

Figure 3.3: Identification algorithm.

Definition 3.2. A signal is called **persistently exciting of order n** if for all filters of the form $M_n(q)$ the relation

$$|M_n(e^{i\omega})|^2\Phi(\omega) \equiv 0 \tag{3.24}$$

is equivalent to

$$M_n(e^{i\omega}) \equiv 0 \tag{3.25}$$

Theorem 3.3. *An experiment where n parameters have to be identified is informative if and only if the input signal is persistently exciting order* $2n$.

From the above discussion it has become clear that it is desirable the signal to contains sufficiently many distinct frequencies. Moreover, to guarantee a high signal-to-noise ratio, a high signal power is necessary. On the grounds that the input signal is usually constrained due to physical limitations, the highest signal power has to be achieved with a given maximum amplitude [50]. This property can be expressed mathematically by demanding the crest factor, defined as

$$C_r = \sqrt{\frac{max_t u^2(t)}{lim_{N\to\infty}\frac{1}{N}\sum_{t=1}^{n} u^2(t)}} \tag{3.26}$$

to be as small as possible. One should take into account that the lower bound of the crest factor C_r is 1. Unfortunately, these two requirements, of small crest factor and sufficiently many distinct frequencies, are in conflict; therefore, a right balance should be achieved between the satisfaction of this two contradictory objectives.

Typical choices of waveforms include Filtered Gaussian White Noise (FGWN), Random Binary Signal (RBS) and Pseudo-Random Binary Signal (PRBS). In the present case, PRBS signal is chosen since it combines advantages of RBS with additional desirable properties found in deterministic signals. PRBS has an optimal crest factor like RBS and it has also good second order properties which are a typical characteristic of deterministic signals. Another property really suitable for identification process is the fact that PRBS signal can be reproduced, so the performance of different models can be evaluated.

Having made the choice of the identification signal, the experiment is carried out and identification dataset is collected; the dataset obtained from the identification experiment is shown in the left plot of Fig. 3.4.

3.7.2 Step No2: Data Preprocessing

The data presented in the left plot of Fig. 3.4 are not ready to be imported to the identification algorithms and have to undergo several processes. Data processing is essential due to the following reasons:

1. Data often contain high frequency disturbances that lie outside the frequency region of interest for the systems dynamics.

2. Occasional bursts and outliers may appear in data.

3. Drift, offset and low-frequency disturbances are usually presented due to the sensors' dynamics.

Observing the identification data set, we can infer that no considerable deficiencies of the first and second categories are noticed. Thereby, we are going to focus our attention on the third category. A typical model that describes the dynamic and static behaviour of a linear system is as follows

$$A(q) \cdot y(t) = B(q) \cdot u(t) + w(t) \tag{3.27}$$

where $y(t)$ is the system's response to input $u(t)$ under the presence of noise $w(t)$. The above equation for constant level input $u(t) \equiv \bar{u}$ and resulting steady state output $y(t) \equiv \bar{y}$ is written as follows

$$A(1) \cdot \bar{y} = B(1) \cdot \bar{u} \tag{3.28}$$

Considering that measurements of $u(t)$ and $y(t)$ are taken at arbitrary levels which are usually unrelated with one another, equation 3.28 may be viwed as an unnecessary constraint of 3.27. In [22] methods are proposed to solve this problem; among this techniques are the following:

1. Let us define the output measurements gathered from an experiment as y_m, corresponding to the input measurements u_m. Furthermore, the system's output to the steady state input $\bar{u}$ is defined as $\bar{y}$. Then, the data for the identification algorithm would be the deviations of the experimental data (y_m, u_m) from the equilibrium values

$$y(t) = y_m(t) - \bar{y} \tag{3.29}$$

$$u(t) = u_m(t) - \bar{u} \tag{3.30}$$

2. Another way to deal with the problem is to subtract the sample means so the processed data would be as follows

$$y(t) = y_m(t) - \frac{1}{N} \sum k = 1^N y_m(k) \tag{3.31}$$

$$u(t) = u_m(t) - \frac{1}{N} \sum k = 1^N u_m(k) \tag{3.32}$$

3. A third method is to keep all variables in their original physical units and add a term in the dynamic equation to compensate for the steady state offset

$$A(q) \cdot y(t) = B(q) \cdot u(t) + w(t) + \alpha \tag{3.33}$$

   The additional term is equal to

$$\alpha = A(1)\bar{y} - B(1)\bar{u} \tag{3.34}$$

   The constant parameter alpha is included in the identification vector θ and estimated from the data.

The second approach is chosen for the specific problem. Moreover, the data are detrended to remove low frequency disturbances and drifts. The initial and the processed data set are presented in Fig. 3.4.

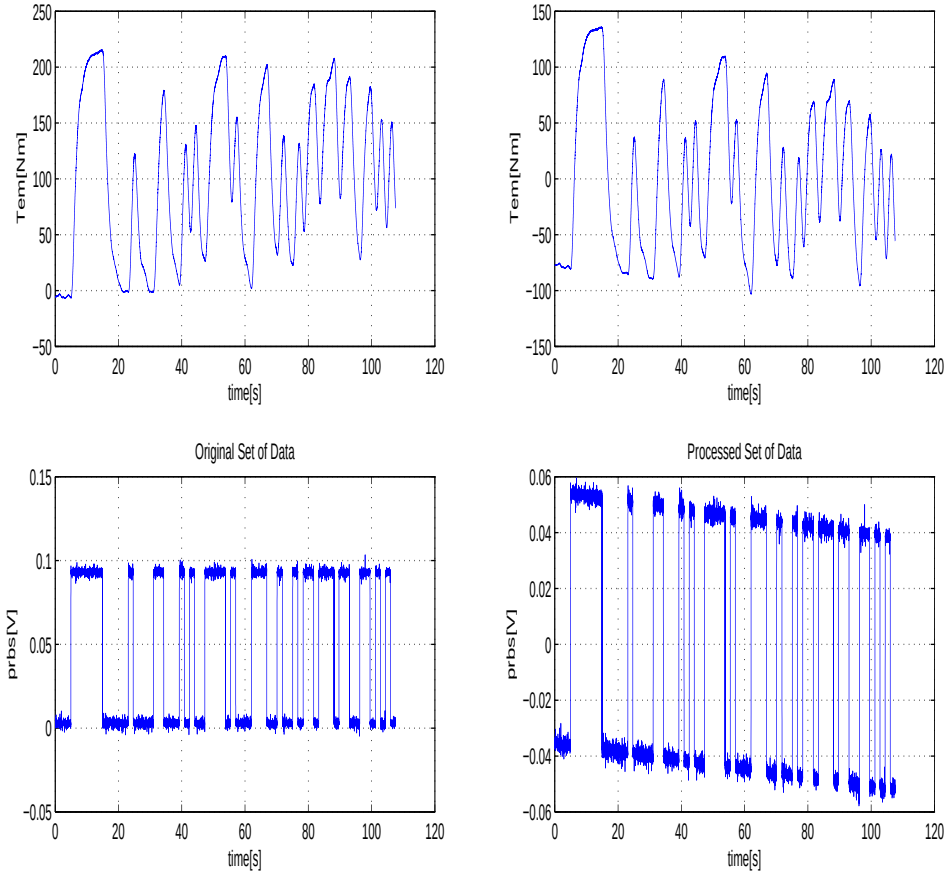

Figure 3.4: Initial and processed identification data.

3.7.3 Step No3: Model Derivation

Although in the beginning of this section it was mentioned that in the identification process no previous knowledge of the plant dynamics is required, any a-priori information about the plant type and order would facilitate the identification process. Particularly in this step, choosing a suitable "family" where the model to be specified belongs and an appropriate identification algorithm can facilitate the identification process.

One of the most common choices in terms of the parametrization of the model G is to let the coefficients of the numerator and denumerator be unknown variables which will be specified by the identification algorithm. Various models with the above generic representation can be found in [22]. In the present case, after careful observation of the identification data set, a continuous transfer function with 3 poles and 1 zero is proposed as the model of the electric motor (EM) torque generation process.

The plant model we want to specify has the following form in Laplace variables

$$Y(s) = \frac{A(s)}{B(s)} \cdot U(s) \tag{3.35}$$

where $U(s)$ and $Y(s)$ are the Laplace transforms of the input and output signals. The main problem is to specify the constant coefficients of the s polynomials of the numerator $A(s)$ and the denominator $B(s)$. For the time instant t the equation becomes

$$y^{(n)}(t) + a_1 y^{(n-1)}(t) + ... + a_n y(t) = b_1 y^{(m-1)}(t) + b_2 u^{(m-2)}(t) + ... + b_m u(t) \tag{3.36}$$

Two important parameters are defined

$$\begin{aligned} \theta &= [1, a_1, ..., a_n, b_1, ..., b_m]^T \\ \phi^T(t) &= [-y^{(n)}(t), ..., -y(t), u^{(m-1)}(t), ..., u(t)] \end{aligned} \tag{3.37}$$

Then the chosen model would be of the form

$$y(t) = \phi^T(t) \cdot \theta^\star \tag{3.38}$$

If all the derivatives where accessible it would be an easy task to estimate the coefficients using a linear regression formula. A proposed solution to the problem is to pass the measurements through a continuous time filter; thereby, the new variables are

$$\begin{aligned} z_k(t) &= L(s) \cdot y_k(t) \\ w_k(t) &= L(s) \cdot u_k(t) \end{aligned} \tag{3.39}$$

and parameter $\phi^T(t)$ if defined accordingly

$$\phi^T(t) = [-z^{(n)}(t), ..., -z(t), w^{(m-1)}(t), ..., w(t)] \tag{3.40}$$

Although the above representation is not mathematically formal as we have mixed time with Laplace variables, it can capture the main concept of first passing the measurements through the filter before applying a linear regression formula. The data filter can have one of the following forms:

- **SVF:** Basic State Variable Filter

$$L(s) = \left(\frac{\lambda}{\lambda + 1}\right)^n \tag{3.41}$$

- **GPMF:** Generalized Poisson Moment Function

$$L(s) = (\frac{\lambda}{\lambda + 1})^{n+1} \tag{3.42}$$

- **Refined:** Refines choice of filter (the denominator of the system)

$$L(s) = \frac{1}{A(s)} \tag{3.43}$$

After passing the data through the filter and assuming no presence of noise the parameters can be solved by the least squares method. The result to the minimization problem

$$\hat{\theta} = argmin \parallel \frac{1}{N} \sum_{k=1}^{N} [y(t_k) - \phi^T(t_k) \cdot \theta] \parallel^2 \tag{3.44}$$

is as follows

$$\hat{\theta} = [\sum_{k=1}^{N} \phi(t_k)\phi^T(t_k)]^{-1} \cdot [\sum_{k=1}^{N} \phi(t_k)z(t_k)] \tag{3.45}$$

However, since noise is presented and cannot be neglected, the entries of the vector in 3.46 are replaced by their instruments and the new parameter vector is given by

$$\zeta^T(t) = [-z_f^{(n)}(t), ..., -z_f(t), w^{(m-1)}(t), ..., w(t)] \tag{3.46}$$

and the parameter vector is now derived from the following equation

$$\hat{\theta} = [\sum_{k=1}^{N} \zeta(t_k)\phi^T(t_k)]^{-1} \cdot [\sum_{k=1}^{N} \zeta(t_k)z(t_k)] \tag{3.47}$$

where the elements of ζ are called instrument of instrumental variables [24].

The choice of filter for the instrumental variables should guarantee that the instruments are correlated with the regression variables but uncorrelated with the noise. The process of choosing instruments is described by Ljung in [22] (Sec. 7.6). After the initialization of the parameter vector, using the above-mentioned estimate, its value is updated using the non-linear least squares method.

For the identification of the transfer function from the processed data set, Matalab's System Identification Toolbox is used with the **tfest** command. Various commands are also available for the identification process in Matlab depending on the knowledge that is possesed about the type of the model to be identified. The transfer function of the Electric Motor that was obtained is:

$$G_{elm}(s) = \frac{1485.7s + 7345.2}{s^3 + 3.1475s^2 + 6.6877s + 3.0062} \tag{3.48}$$

3.7.4 Step No5: Model Validation

The parameter estimation algorithms converge to the best model within the specified set of possible models. However, the problem that arises is whether the model obtained is good enough in terms of:

1. Agreeing quite well with the observed data.

2. Being suitable for the developed purpose.

3. Describing adequately well the true system.

Question 3 cannot be answered in practical situations, so the most crucial requirement of the identified model is to be useful for the initial problem that was designed for. However, testing all the models can be time-consuming and costly for control applications. Developing some confidence in the identified models before they are implemented in the real plant is far more preferable option.

One suggested way to investigate model's simplicity is through the application of an order reduction algorithm and examination of its effect on model's input-output dynamics. Very fast modes of the model that correspond to very small singular values can be neglected without a substantial error. Clearly, a model that can be reduced without losing its ability in describing the input-output dynamics is unnecessarily-complex.

In order to have a quantitative measure of the relative ability of the original and the reduced order model to describe the process, the error between them can be evaluated. The H_∞ norm of the difference between the original system G and the reduced system G_k of order k satisfies

$$\|G - G_k\|_\infty \leq 2(\sigma_{k+1} + ... + \sigma_n) \tag{3.49}$$

where $\sigma_1, ..., \sigma_n$ are the hankel singular values of the system G [39]. The magnitude of the singular values is given in the following matrix

Table 3.1: Singular values of the Electric Motor transfer function

σ_1	1440
σ_1	294
σ_1	73

Another common method for evaluating model's performance is by simulating model's response and compare it with the actual response of the system. In this way, all the features that can be captured and the ones which could not be reproduced by the model are revealed. For the identification of the transfer function only half of the whole experimental set of data was used. The other half was used to validate the identified transfer function. Figure 3.5 depicts the comparison between torque output from the identified transfer function and the torque as derived from the experimental set of data of the real plant with the input shown in Fig. 3.6 .

Finally, a very effective way of evaluating model's performance is through the computation of the residuals. Residuals are the part of the data that the model was unable to reproduce. Consequently, model quality is in a direct correlation with the information obtained from the residuals.Precisely residuals are defined as

$$\epsilon(t) = \epsilon(t, \hat{\theta_N}) = y(t) - \hat{y}(t|\hat{\theta_N}) \tag{3.50}$$

In order to drive conclusions from the residuals the following statistic variables are defined

$$S_1 = max_t|\epsilon(t)|, S_2 = \frac{1}{N}\sum_{t=1}^{N}\epsilon^2(t) \tag{3.51}$$

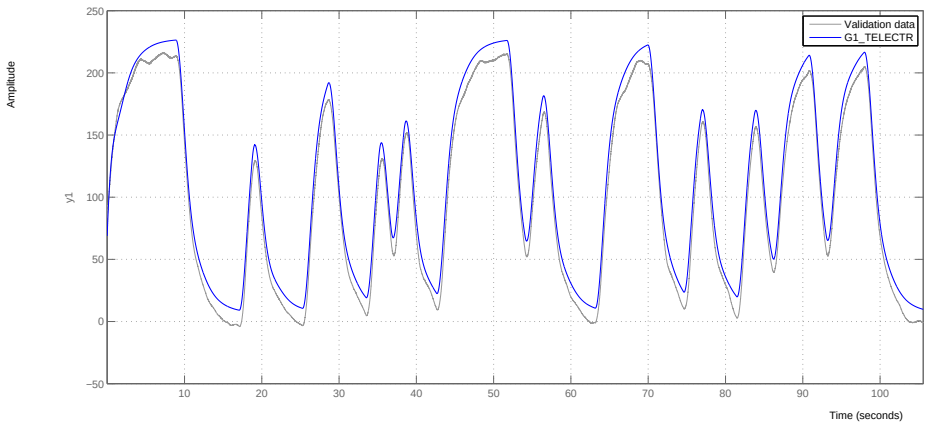

Figure 3.5: Comparison between the identified transfer function and the experimental dataset.

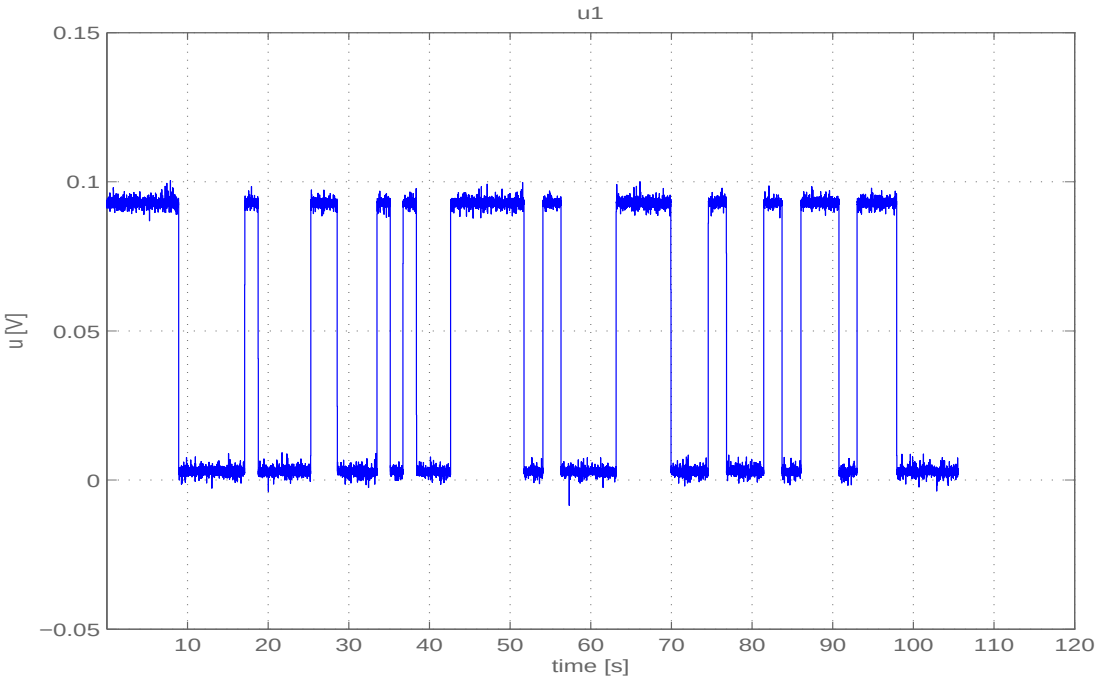

Figure 3.6: Model validation input signal.

where the first variable is effectively an approximate measure about the magnitude of the largest residual that the model will produce and the second quantity is the average error for this estimation.

Moreover the residuals should not depend on a particular set, for instance the data set that was used to identify the model. If such a dependency exists, then it is possible that residuals contain traces of the past inputs and the model will not produce good results for other inputs. A way to check this dependency is through the computation of the covariance between the residuals and the past inputs

$$\hat{R_{eu}^N}(\tau) = \frac{1}{N}\sum_{t=1}^{N}\epsilon(t)u(t-\tau) \tag{3.52}$$

Another equivalent way to test this property is by the computation of the auto correlation between the residuals themselves

$$\hat{R_{e}^N}(\tau) = \frac{1}{N}\sum_{t=1}^{N}\epsilon(t)\epsilon(t-\tau) \tag{3.53}$$

If this number is large then a part of $y(t)$ has not been modelled well, as a certain part of ϵ could have been predicted from past data.

3.8 Water Brake Model

From data acquired from the LME, the transfer function of the water brake oopen loop plant model and the feedback controller were obtained. The closed loopd model from the reference torque value to the demanded torque is given by

$$G_{wb}(s) = \frac{GK}{(1-GK)} \tag{3.54}$$

where G is the transfer function of the open loop plant-from the valve command to the torque demand-and K is the controller designed to achieve the reference torque. The step response of the closed loop transfer function $G_{wb}(s)$ is shown in Fig. 3.7 and the corresponding bodeplot is illustrated in Fig. 3.8.

When the requested load reaches $M_{req} \simeq 500Nm$ the operation of the controller becomes marginally unstable and the torque oscillates significantly. The oscillatory behaviour steam from the fact that the model of the hydraulic brake demonstrates a highly non-linear behaviour in high loads which has not been reproduced by the open loop plant model used for the controller design.

3.9 Acceleration Model

Suppose that the engine is running at steady state and, as a result, engine acceleration is approximately zero, since the produced torque equals the requested torque. As soon as the new higher load is applied, a torque deficit appears, the engine is decelerated and the engine speed drops. The drop in engine speed is sensed from the speed governor which increases the fuel injected into the cylinder by an appropriate amount.

As can be seen from Fig. 3.9 the engine acceleration is higher when the load increase is more substantial.

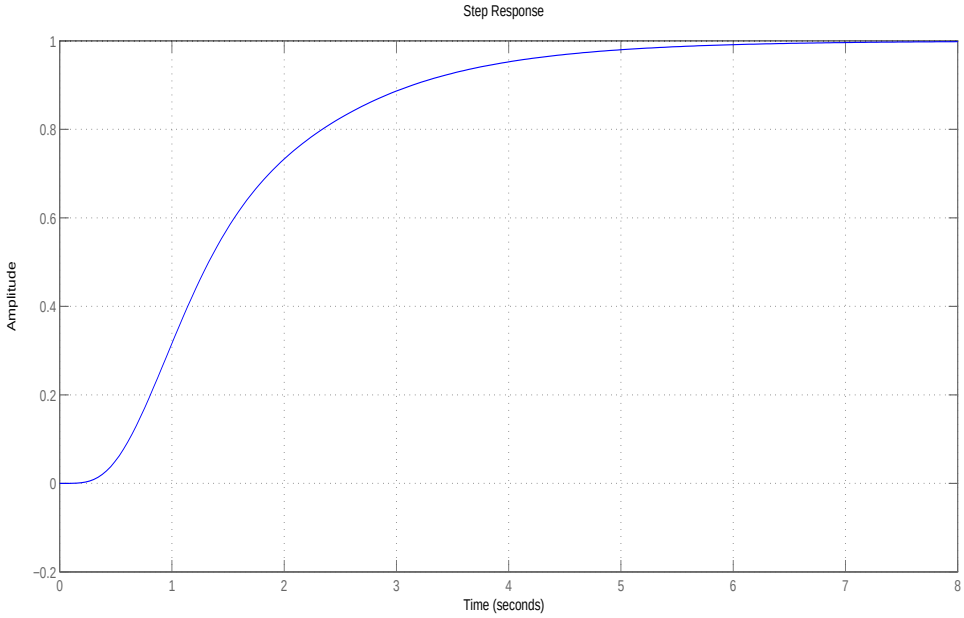

Figure 3.7: Step response of the closed loop transfer function $G_{wb}(s)$.

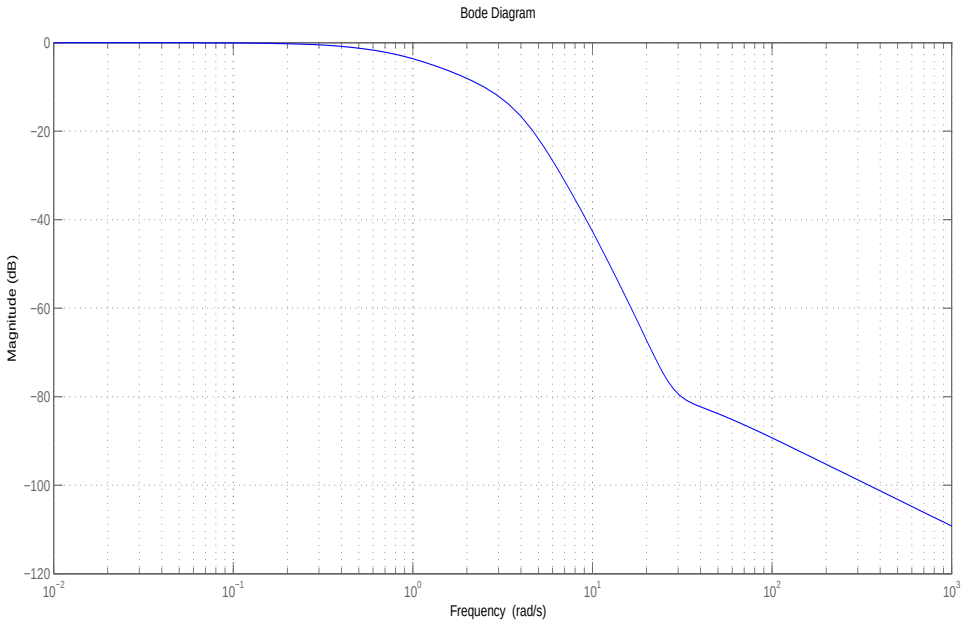

Figure 3.8: Bode-plot of the closed loop transfer function $G_{wb}(s)$.

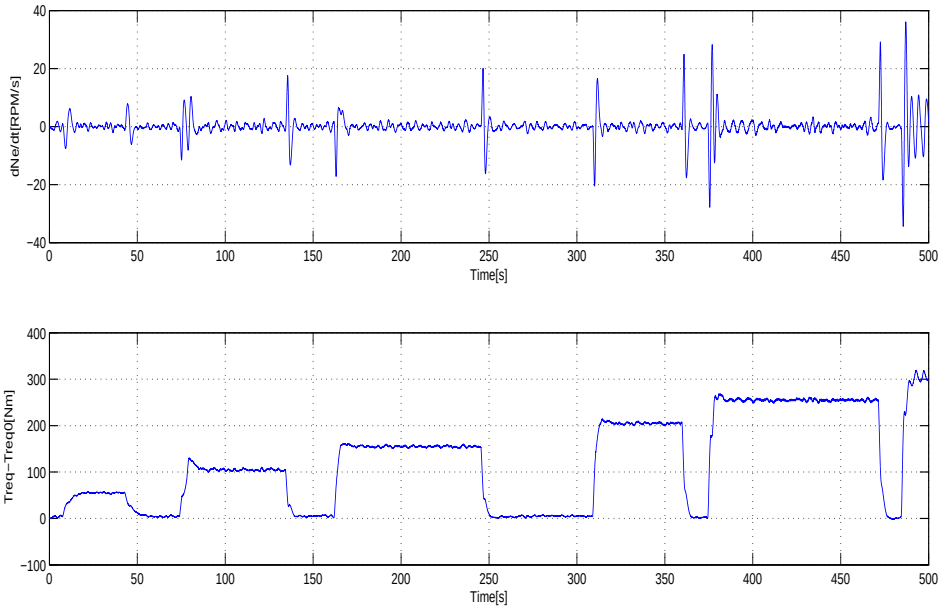

Figure 3.9: Top: Engine acceleration, Bottom: Various load increases. The sampling time is $T_s = 0.001s$.

The data illustrated in Fig. 3.9 will be divided into four separate data sets which will be used for the identification of the acceleration transfer function. For this reason, MATLAB/System Identification Toolbox will be used to estimate four transfer functions with input the requested torque difference between the current value and the steady state value $M_{req} - M_{req0}$ and with output the rotational acceleration of the engine $\dot{N}_e$. The final transfer function will be an uncertain linear time invariant model as will be shown in Subsection 3.10.3.

Figure 3.10 presents the four estimated transfer functions for the four step loads.

3.10 Uncertainty Modelling

3.10.1 Uncertainty in Willans Parameters

It is worth noting that Willans parameters are primarily functions of the mean piston speed c_m. Additionally, there is weak dependency in other physical variables such as the mass of fuel burned in the cylinder $\dot{m}_f$, the value of lambda λ, et.c. [13].

On the grounds that only experimental data for $N_e = 1600$ RPM were available, the dependency on the piston speed and the other parameters can be taken into account by assuming that the value of these coefficients is uncertain. The identified values from linear regression are denoted as $e\bar{w}$ and $\bar{p}_{ml}$. The final uncertain Willans parameters are

$$ew = e\bar{w} \cdot (1 + \delta_{ew}) \tag{3.55}$$

and

$$p_{ml} = \bar{p}_{ml} \cdot (1 + \delta_{p_{ml}}) \tag{3.56}$$

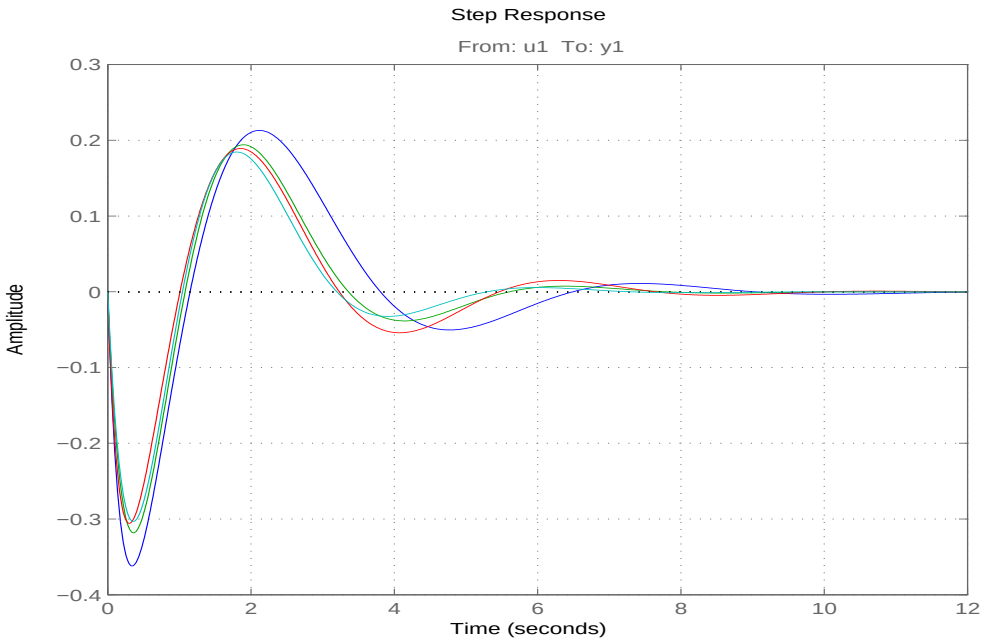

Figure 3.10: Step responses of identified transfer functions.

where δ_{ew} and $\delta_{p_{ml}}$ are uncertain real parameters which take values in the range $[\delta_{ew,min}, \delta_{ew,max}]$ and $[\delta_{p_{ml},min}, \delta_{p_{ml},max}]$, respectively and correspond to deviations of the nominal values.

3.10.2 Uncertainty in Turbine's is-entropic efficiency

As mentioned in Subsection 3.2.2, the isentropic efficiency is usually evaluated from the data obtained by the manufacturer. Obviously, no effect of corrosion is taken into account in these data. However, turbine's performance can substantially deteriorate over time due to the corrosion effect of the exhaust gases and the pollutant formations. For this reason, the so called "nominal is-entropic efficiency" derived from Eq. 3.10 is corrected by an uncertain factor as follows

$$\eta_{is,t} = \eta_{is,tnom} \cdot (1 + \delta_{\eta_{is,t}}) \tag{3.57}$$

where $\delta_{\eta_{is,t}}$ is a uncertain real parameter which takes values in a appropriate range $[\delta_{\eta_{is,tmin}}, \delta_{\eta_{is,tmax}}]$.

3.10.3 Uncertainty in Rotational Acceleration Transfer Function

Firstly, the so-called "Nominal Transfer Function" is chosen to be the transfer function whose step response is shown with green continuous line in Fig. 3.10. This choice is made because this transfer function has a step response that lies in between the two extreme responses and is approximately in the middle of them. Clearly, the choice of a more simple and of lower order transfer function can be made at the expense of a very wide uncertainty region.

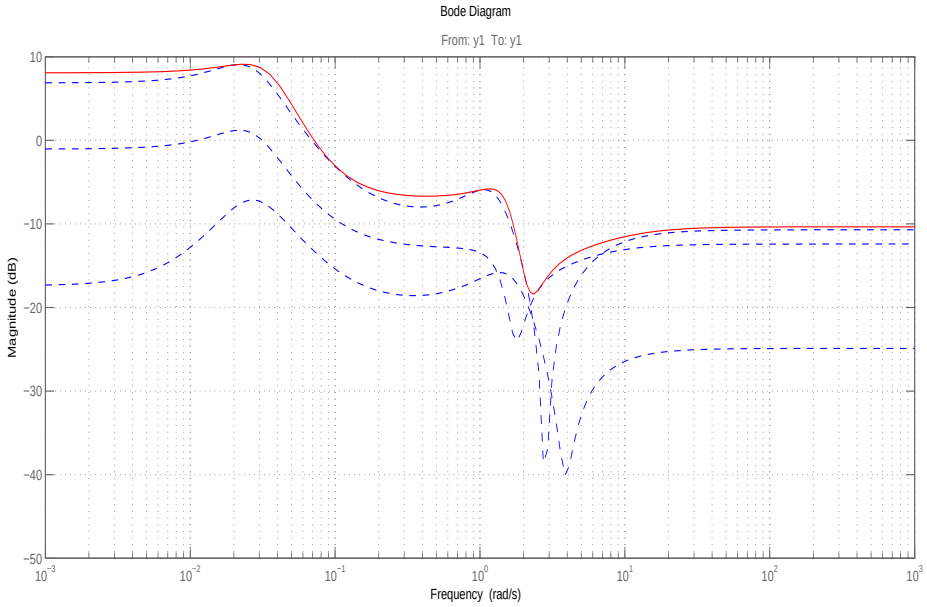

Figure 3.11: Relative error and 5th order weight bound.

Secondly, the assumption that the final family of transfer functions is given by

$$\dot{N}_e(s) = \dot{N}_{enom}(s) \cdot (1 + W_{\dot{N}_e}(s)\Delta(s)) \tag{3.58}$$

is made where $\dot{N}_{enom}(s)$ is the Nominal Transfer Function, $\Delta(s)$ are the unmodelled dynamics and $W_{\dot{N}_e}(s)$ is a weight appropriately chosen so that the uncertain transfer function $\dot{N}_e(s)$ cover the whole range of responses shown in Fig. 3.10. In order to derive this weight the relative error between the Nominal Transfer Function and all the other three transfer functions identified with Matlab System Identification Toolbox is evaluated. The relative error for the three identified transfer functions along with the the evaluated $5th$ order weight which is approximately the upper bound of the relative error is given as a function of frequency in the magnitude bode plot of Fig. 3.11.

In order to verify the accuracy of the estimated weight, the step response of the uncertain transfer function (which is actually a "family" of step responses) is compared to the step responses of the four identified transfer functions. As shown in Fig. 3.12, the step responses of the four identified transfer functions lie in the range of responses of the uncertain transfer function $\dot{N}_e(s)$.

3.11 Dynamic Uncertain Model Simulation

3.11.1 Step Load

To examine the validity of the proposed model of the ICE, an experiment was carried out in the LME where the turbocharger speed N_{tc}, the barometric pressure in the intake manifold p_{im}, the engine speed N_e, the torque produced by the ICE T_{ice} and lambda λ at the exhaust duct were measured. The torque requested from the ICE was the

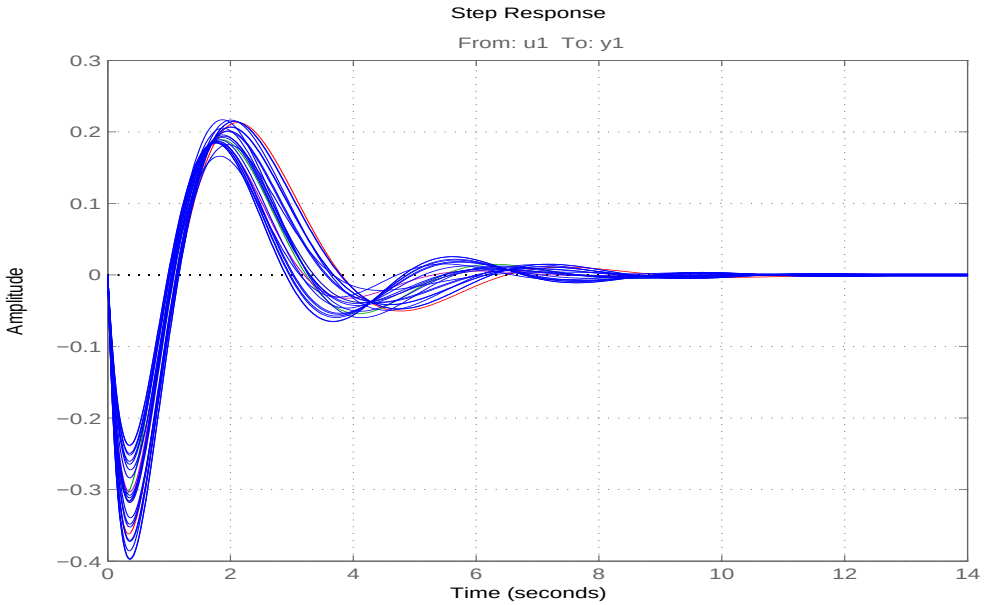

Figure 3.12: Step responses of the four identified transfer functions and the uncertain transfer function $\dot{N}_e(s)$.

single input to the developed non-linear uncertain model, while all the other variables were simulated. The results obtained are shown in Fig. 3.15 for the step load depicted in Fig. 3.13.

As presented in Fig. 3.15 the simulated turbocharger speed N_{tc} and the pressure in the intake manifold p_{im} match the experimental data. The proposed model can capture the transient behaviour of these variables and also the steady state error is less than 100 RPM for the turbocharger speed N_{tc} and 0.02 bar for the intake manifold pressure p_{im}. Regarding the value of lambda λ we can observe a very good agreement between the experimental data and the simulated value. Precisely, the dynamic behaviour of lambda during load increases is reproduced by the model and the model has the desirable property of not producing spikes during load decrease. The maximum steady state error between the simulated and the measured value is below 0.15 and is noticed only for load 110 Nm. Apart from this, the steady state error between the simulated and the measured value of λ is close to zero for the various loads applied.

3.11.2 Propeller Load

Since the ICE is an integrated part of a hybrid marine propulsion plant, it will be useful to investigate the validity and performance of the model in a propeller load which is a more realistic demand from a marine plant. The propeller load applied is illustrated in Fig. 3.14.

As presented in Fig. 3.16 the performance of the uncertain model is still acceptable even in the case of a propeller load. Despite the fact that higher deviation between the measured and the simulated physical variables is presented in this case (particularly, for the intake manifold pressure p_{im}), the model can capture with adequate accuracy

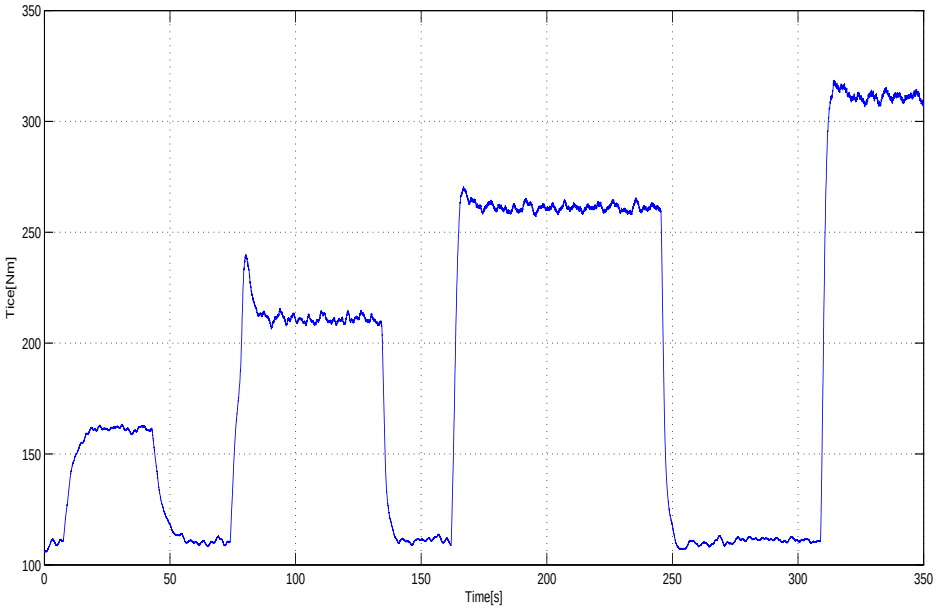

Figure 3.13: Torque step load.

the variations of lambda λ.

An important note that should be made regarding Figs. 3.15 and 3.16 is that in the former only the nominal model was simulated while for the latter the uncertain model is simulated. The reason for this choice is the fact that Willans parameters depend on engine speed; thus, it is desirable to examine the validity of the uncertain model within a wider range of this parameters.

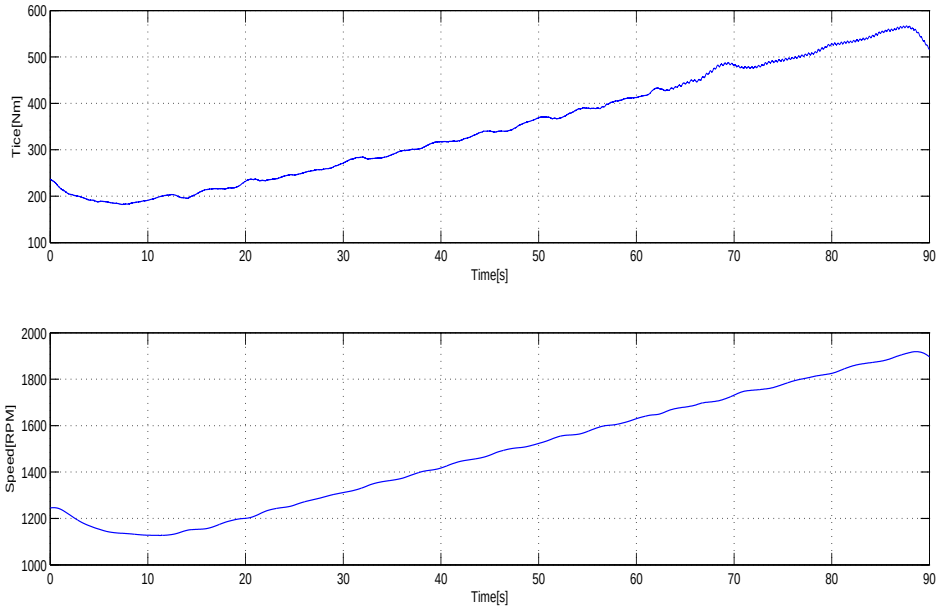

Figure 3.14: Propeller load torque and rotational speed.

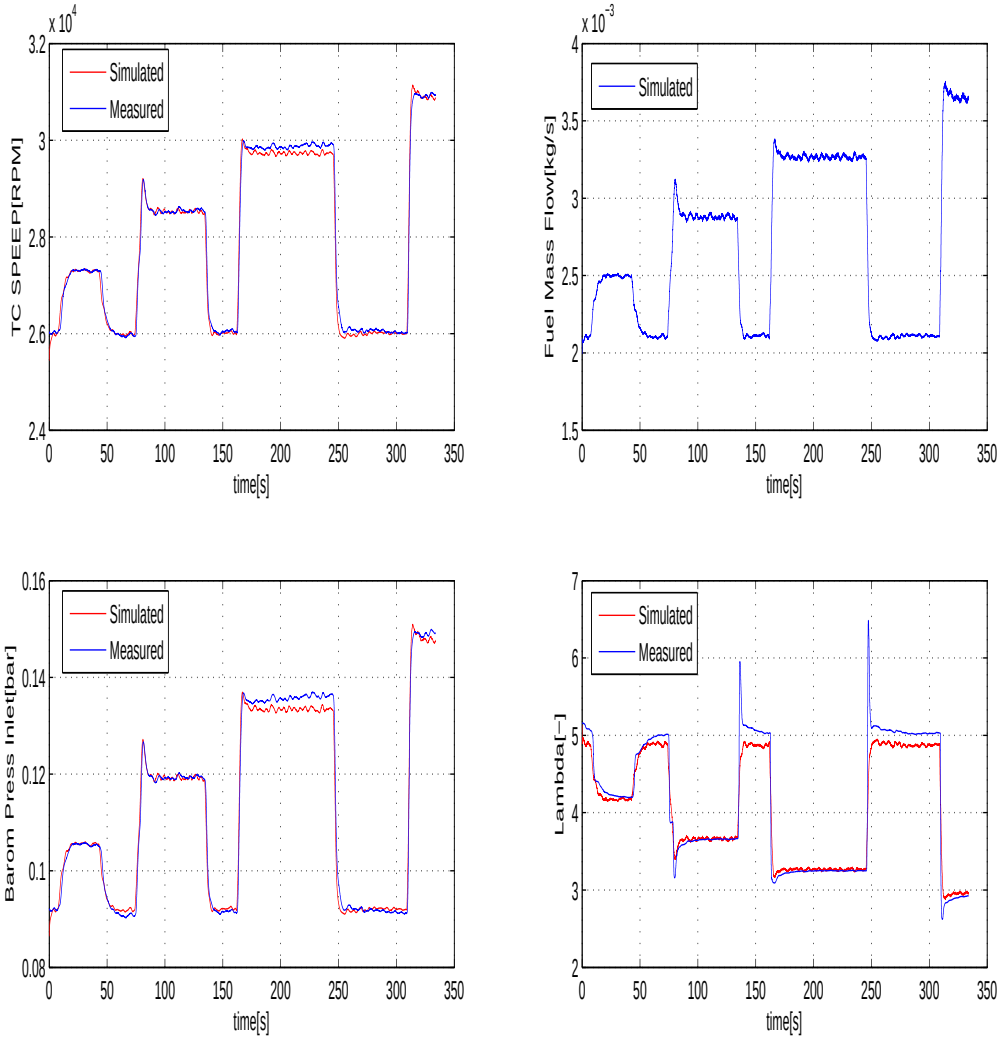

Figure 3.15: Simulated nominal and measured variables for a step load.

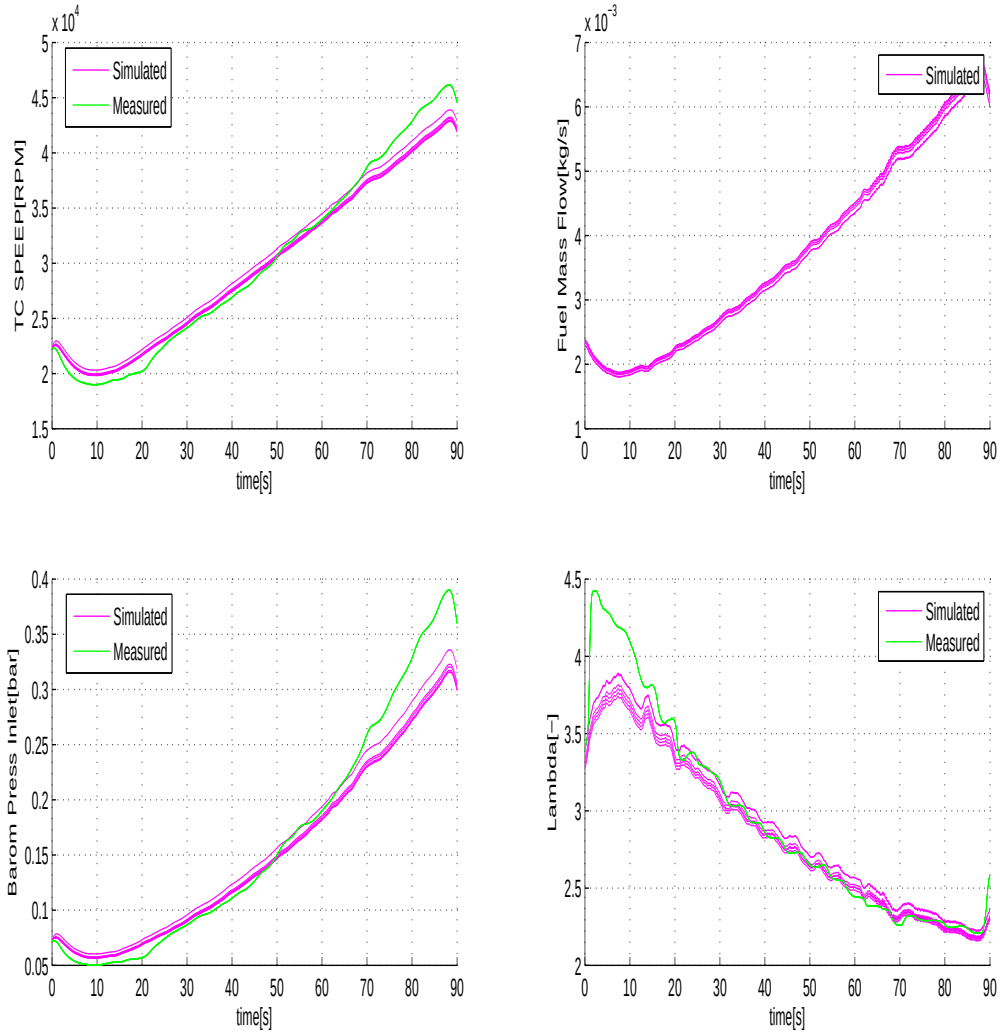

Figure 3.16: Simulated uncertain and measured variables for a propeller load.

Chapter 4

Static Uncertain Non-Linear Model of Lambda

After the non-linear dynamic uncertain model of the ICE has been developed in Chap. 3, it is further processed in this chapter in order to derive constraint equations among the various physical variables of the ICE in steady state. These algebraic equations are obtained by neglecting dynamic terms with minor influence in the steady state behaviour of the ICE. The main objectives of the derivation of these algebraic equations are the implementation of a second virtual sensor model which make use of only one physical variable and the computation of the physical variables in the operating point of the ICE where the non-linear dynamic system is linearised in Chap. 5.

4.1 Compressor and engine match

In steady state operation and very slow load transients, the mass of air in the intake manifold is approximately constant (no positive or negative mass of air accumulation); thereby, this assumption yields $dm_{im}/dt = 0$ *(assumption A)*. Under the assumption of zero mass accumulation, Eq. 2.1 yields

$$\dot{m}_c[N_{tc}, \Pi_c(p_{im}, m_c)] = \dot{m}_e(N_e, T_{im}, \eta_v, p_{im}) \tag{4.1}$$

Additionally the thermodynamic states are assumed constant in the intake manifold, so that $dp_{im}/dt = 0$ *(assumption B)*. With the use of assumption A, assumption B and Eq. 2.7 the following equality is obtained

$$T_{im} = T_{ac}[\Pi_c(p_{im}, m_c), N_{tc}] \tag{4.2}$$

Moreover, that engine's volumetric efficiency η_v will be assumed that attains a constant value within the operation range of interest *(assumption C)*. Under assumptions A, B and C a simple equation can be obtained

$$\dot{m}_c(N_{tc}, p_{im}) = \dot{m}_e(N_e, p_{im}) \tag{4.3}$$

For constant engine speed equality 4.3 is a useful relationship that directly connects the pressure in the intake manifold pressure p_{im} with the turbocharger speed N_{tc}. In addition, intake manifold pressure p_{im} can be very-well approximated by a quadratic

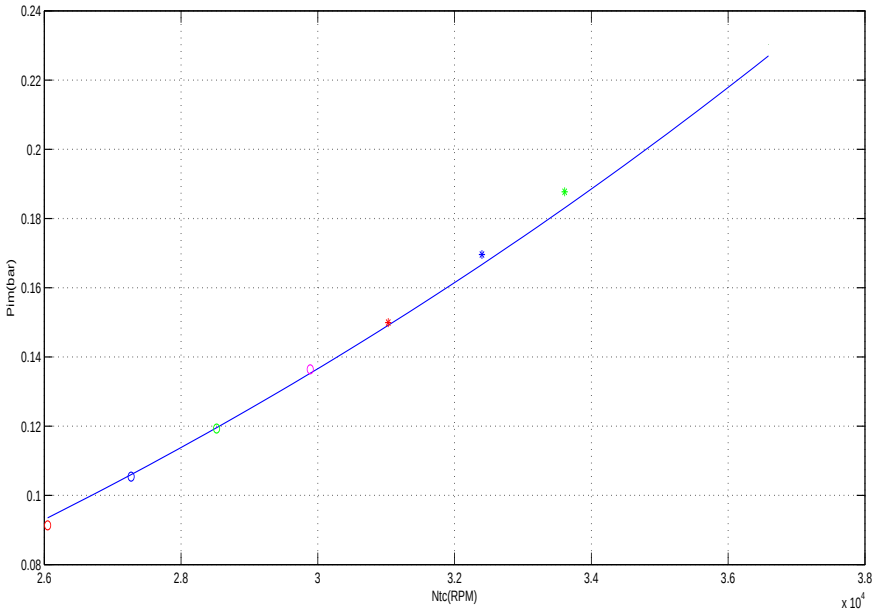

Figure 4.1: Relationship between pressure in the intake manifold and turbocharger speed.

function of the turbocharger speed N_{tc} [29]. The coefficients of this quadratic polynomial are parametric functions of the engine speed. To put it in a more concrete way for a specified engine speed N_e the following equation holds

$$p_{im} = f_{coem}(N_{tc}) \tag{4.4}$$

where the name "coem" stands for the abbreviation of the words **co**mpressor and **e**ngine **m**atch.

To illustrate the result, an experiment was carried out for constant engine speed $N_e = 1600RPM$ and under engine loads M_e in the range $[100 : 500]Nm$, where the pressure in the intake manifold p_{im} and the turbocharger speed N_{tc} were measured. Figure 4.1 depicts the non-linear function as it was derived from Eq. 4.3 and the quadratic approximation of it along with the experimental set of points as measured from the experiment. The non-linear function that was derived from Eq. 4.3 and the quadratic approximation of it match so well that they are not even distinguishable from one another.

4.2 Turbocharger and Engine Match

In Sec. 4.1,a non-linear relationship between the turbocharger speed N_{tc} and the intake manifold pressure p_{im} was derived, by making simplifications associated with the intake manifold dynamics. In this section, a simple relation between the turbocharger speed N_{tc} and the fuel mass flow $\dot{m}_f$ in the Internal Combustion Engine is developed.

Firstly the assumption that the change of kinetic energy stored in the turbocharger shaft is negligible-especially in steady state operation when the acceleration is approx-

imately zero-due to its small inertia is adopted; thus, under this assumtpion it holds that $\frac{d}{dt}(\frac{1}{2}J_{tc}w_{tc}^2) = 0$ *(assumption D)* and

$$P_t = P_c \tag{4.5}$$

Secondly, proceeding in a similar way to the intake manifold case and assuming that $dm_{em}/dt = 0$ *(assumption E)*, Eq. 3.14 can be simplified to

$$\dot{m}_t = \dot{m}_e + \dot{m}_f \tag{4.6}$$

A further assumption made is that no heat transfer takes place between the exhaust duct and the atmosphere, so that $\dot{Q}_{em} = 0$ *(Assumption G)*. Moreover, the thermodynamic states in the exhaust manifold are approximately time invariant and, as a result, $dp_{em}/dt = 0$ *(Assumption F)*. The aforementioned two assumptions and Eq. 3.15 yield

$$T_{ti} = T_{exh} \tag{4.7}$$

The dependency of all the above-mentioned physical quantities on physical variables will be presented. The compressor power is given by

$$P_c = P_c(\dot{m}_c, T_c, \eta_{is,c}, \Pi_c) = P_c(N_{tc}, P_{im}) \tag{4.8}$$

where the last equality in Eq. 4.8 is derived from the fact that all the variables that appear on the left side of equation are functions of N_{tc} and P_{im}. Furthermore, from Eq. 3.13 the following dependency can be inferred

$$\begin{aligned} &P_t = P_t(\dot{m}_t, T_{em}, \eta_{is,t}, \Pi_t) = \text{[Using eq. 3.4,eq. 3.1 and eq. 3.10]} \\ &= P_t[\dot{m}_t(\Pi_t), T_{em}(\dot{m}_e, \dot{m}_f, T_{im}), \eta_{is,t}(\Pi_t, N_{tc})] = \\ &= P_t[\dot{m}_t(\Pi_t), T_{em}[\dot{m}_e(N_{tc}, p_{im}, \eta_v, N_e), \dot{m}_f, T_{im}(N_{tc}, p_{im})], \eta_{is,t}(\Pi_t, N_{tc})] = \\ &= P_t(N_{tc}, p_{im}, \dot{m}_f, \Pi_t, \eta_v, N_e) \end{aligned} \tag{4.9}$$

As it was mentioned in Sec. 4.1 a quadratic relationship between pressure in the intake manifold p_{im} and the turbocharger's shaft speed N_{tc} for constant engine speed N_e is valid. Inserting Eq. 4.4 into Eq. 4.9 yields

$$P_t = P_t(N_{tc}, \Pi_t, \dot{m}_f) \tag{4.10}$$

Now we can derive that

$$\Pi_t = f_{tuem}(N_{tc}, \dot{m}_f) \tag{4.11}$$

according to Eqs. 4.10,4.8,4.4 and 4.5, where the name "tuem" stands for the abbreviation of the words **tu**rbine and **e**ngine **m**atch.

To be more precise uncertain term has to be included in Eq. 4.11, steaming from the fact that the exact value of $\eta_{is,t}$ is not known.

$$\Pi_t = f_{tuem}(N_{tc}, \dot{m}_f, \delta_{\eta_{is,t}}) \tag{4.12}$$

Furthermore, Eq. 4.6 shall be written as follows

$$\dot{m}_t(\Pi_t) = \dot{m}_c(N_{tc}, p_{im}) + \dot{m}_f \tag{4.13}$$

Using the function 4.4 and 4.12 the above equation can be written as follows

$$\dot{m}_t[\Pi_t(N_{tc}, \dot{m}_f, \delta_{\eta_{is,t}})] = \dot{m}_c[N_{tc}, P_{im}(N_{tc})] + \dot{m}_f \tag{4.14}$$

It is clear from Eq. 4.14 that turbocharger speed N_{tc} and the fuel mass flow $\dot{m}_f$ are connected with a non-linear relationship. Consequently, there is an uncertain function

$$N_{tc} = f_{tcem}(\dot{m}_f, \delta_{\eta_{is,t}}) \tag{4.15}$$

where the name "tcem" stands for the abbreviation of the words **t**urbo**c**harger and **e**ngine **m**atch.

In steady state condition, when all transient phenomena are negligible, the torque produced by the Internal Combustion Engine M_e equals the torque requested from the Internal Combustion Engine M_{req} and, consequently, engine's rotational acceleration is zero $dN_e/dt = 0$ *(assumption H)* . The equation that describes the fuel mass flow in steady state condition is as follows

$$\dot{m}_f = \frac{\omega_e \cdot M_{req} + M_{loss}}{H_{LV} \cdot ew} \tag{4.16}$$

So the relation that holds between the requested torque and the fuel mass flow if we also include the uncertain terms $\delta_{p_{ml}}$ and δ_{ew} from the Willans approximation is the following

$$\dot{m}_f = \dot{m}_f(M_{req}, \delta_{ew}, \delta_{p_{ml}}) \tag{4.17}$$

Substituting Eq. 4.17 into function 4.15 yields

$$N_{tc} = f_{tcem'}(M_{req}, \delta_{\eta_{is,t}}, \delta_{ew}, \delta_{p_{ml}}) \tag{4.18}$$

The above function is valid only for a specified engine speed.

Figure 4.2 depicts that the experimental points lie within the region of validity of the theoretically derived uncertain function 4.18. The experiment was carried for constant engine speed at $N_e = 1600RPM$.

4.3 Derivation of a static and non-linear torque to lambda model

4.3.1 Air Path and Fuel Path Modelling

According to 4.3, the mass of air aspirated by the engine is assumed equal to the air mass flow through the compressor. Thus, the following equation is obtained

$$\dot{m}_e = \dot{m}_c(N_{tc}, p_{im}) \tag{4.19}$$

according to the previous assumption. The air mass flow through the compressor can be derived easily from the compressor maps which are functions of the turbocharger shaft speed N_{tc} and the compression ratio Π_c.

Moreover, under the simplifications that Eqs. 4.18 and 4.4 are valid, it follows from the previously derived equations that

$$\begin{aligned} \dot{m}_e &= \dot{m}_c[f_{tcem}(M_{req}, \delta_{\eta_{is,t}}, \delta_{ew}, \delta_{p_{ml}}), f_{coem}(N_{tc})] = \\ &= \dot{m}_c[f_{tcem}(M_{req}, \delta_{\eta_{is,t}}, \delta_{ew}, \delta_{p_{ml}}), f_{coem}(f_{tcem}(M_{req}, \delta_{\eta_{is,t}}, \delta_{ew}, \delta_{p_{ml}}))] = \\ &= \dot{m}_c(M_{req}, \delta_{\eta_{is,t}}, \delta_{ew}, \delta_{p_{ml}}) \end{aligned} \tag{4.20}$$

The mass of fuel in steady state condition can be directly estimated from 4.17

$$\dot{m}_f = \dot{m}_f(M_{req}, \delta_{ew}, \delta_{p_{ml}}) \tag{4.21}$$

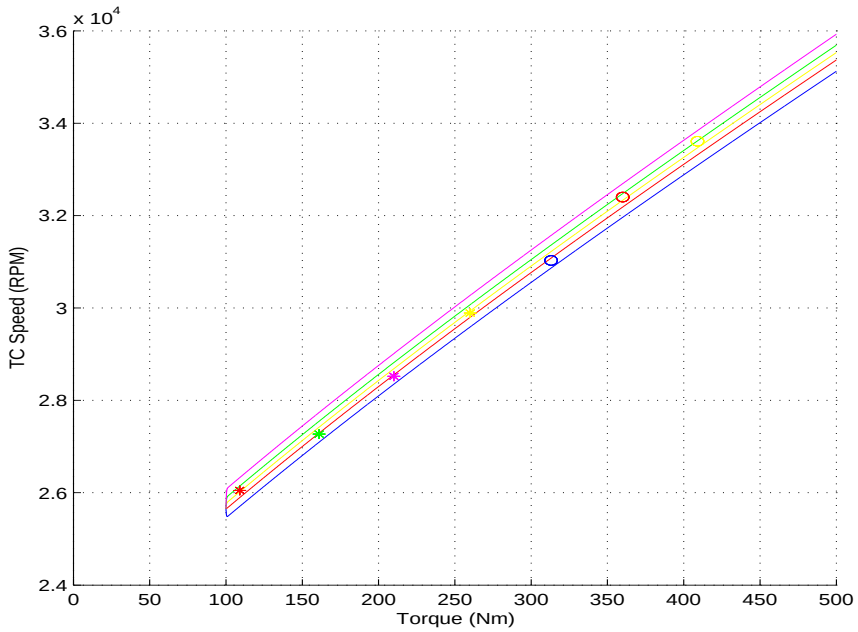

Figure 4.2: Relationship between the requested torque from the internal combustion engine and turbocharger speed.

4.3.2 Lambda Estimation

When the transient phenomena in the ICE have declined, the value of λ will be constant over time and no difference in the values of λ for two consecutive engine cycles will be observed $[\lambda(t-\tau_{ieg}) = \lambda(t)]$ *(Assumption I)*. Assumption I and Eq. 2.95 yield

$$\lambda(t) = \lambda_{fc}(t) \tag{4.22}$$

The value of λ inside the cylinder is given by

$$\lambda(M_{req}, \delta_{\eta_{is,t}}, \delta_{ew}, \delta_{p_{ml}}) = \frac{\dot{m}_e(M_{req}, \delta_{\eta_{is,t}}, \delta_{ew}, \delta_{p_{ml}})}{\dot{m}_f(M_{req}, \delta_{ew}, \delta_{p_{ml}}) \cdot AFR_{st}} \tag{4.23}$$

As can be seen from Eq. 4.23, λ is only a function of the requested torque M_{req} and the uncertain parameters. We have to make clear in this point that the above relation holds only for a specified engine speed. In other words it is a parametric function of the engine speed as well

$$\lambda(M_{req}, \delta_{\eta_{is,t}}, \delta_{ew}, \delta_{p_{ml}}; N_e) = \frac{\dot{m}_e(M_{req}, \delta_{\eta_{is,t}}, \delta_{ew}, \delta_{p_{ml}}; N_e)}{\dot{m}_f(M_{req}, \delta_{ew}, \delta_{p_{ml}}; N_e) \cdot AFR_{st}} \tag{4.24}$$

4.4 Static Non linear model validation

The validity between the proposed static non-linear model was examined by comparing the theoretically derived non-linear function to an experimental set of points. Figure 4.3 demonstrates that all the experimental data points are within the region of validity of the uncertain model.

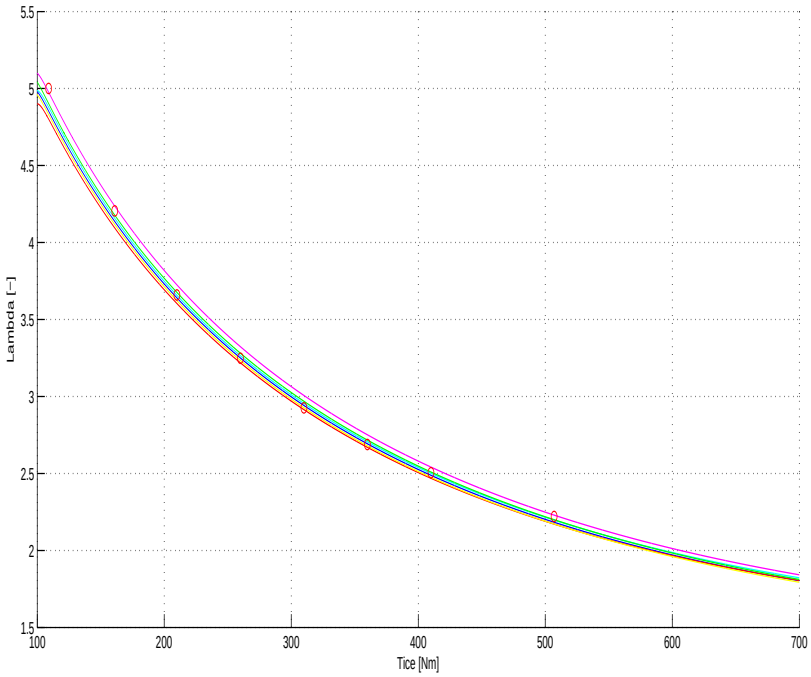

Figure 4.3: Comparison between the static non-linear function of lambda and the experimental set of data.

4.5 Virtual Sensor for Direct Implementation in Diesel Plants

In the virtual sensor designed in Chap. 2, the assumption that there is availability of the torque measurement is adopted. Although a torque measurement device is common for most diesel engine test benches, this is not the case for commercial power-trains due to the high cost of this sensor. An alternative way of fuel estimation is presented in this section.

Equations 4.9 and 4.13 yield that

$$P_t = \phi(p_{im}, N_{tc}, \dot{m}_f, \eta_v, \Pi_t, N_e) \text{ and } \Pi_t = \psi(N_{tc}, \dot{m}_f, p_{im}) \tag{4.25}$$

In this approach, the transient effects of the exhaust manifold are assumed to be negligible. Proceeding the same way for the intake manifold equation

$$p_{im} = \zeta(N_{tc}; N_e) \tag{4.26}$$

is obtained.

Clearly, the simplicity steaming for this assumptions comes at the expense of weak prediction of the engine transient behaviour during very fast load transients. However, for marine application this is a fair approximation. Later in Chap. 5 the relative significance of the neglected terms will be evaluated.

For constant N_e and η_v Eqs. 4.25 and 4.26 may as well be written as

$$P_t = \phi(N_{tc}, \dot{m}_f; N_e) \tag{4.27}$$

Moreover, instead of proceeding as usual and ignoring the dynamic effects of the turbocharger inertia, turbocharger change in kinetic energy is taken into account. Thus, it can be derived that

$$P_t = \frac{d}{dt}(\frac{1}{2}J_{tc}w_{tc}^2) + P_c(N_{tc}, p_{im}; N_e) \tag{4.28}$$

and for constant engine speed, the above equation with the use of 4.26 and 4.27becomes

$$P_t(N_{tc}, \dot{m}_f; N_e) = \frac{d}{dt}(\frac{1}{2}J_{tc}(\pi N_{tc}/30)^2) + P_c(N_{tc}; N_e) \tag{4.29}$$

Applying a filter in Eq. 4.29 in order to make the derivative term realizable yields

$$H_{fi}[P_t(N_{tc}, \dot{m}_f; N_e)] = H_{df}[\frac{1}{2}J_{tc}(\pi N_{tc}/30)^2)] + H_{fi}[P_c(N_{tc}; N_e)] \tag{4.30}$$

Equation 4.30 is the final relationship from which the fuel mass flow can be calculated. It should be noted that filtering of Eq. 4.29 is essential in order to remove the effect of noise. Nonetheless, filtering introduces a time delay and lambda estimation is delayed.

The experimental results shown in Fig. 4.4 illustrate that the virtual sensor model displayed an acceptable performance during load transients. However, the slow response should be noted.

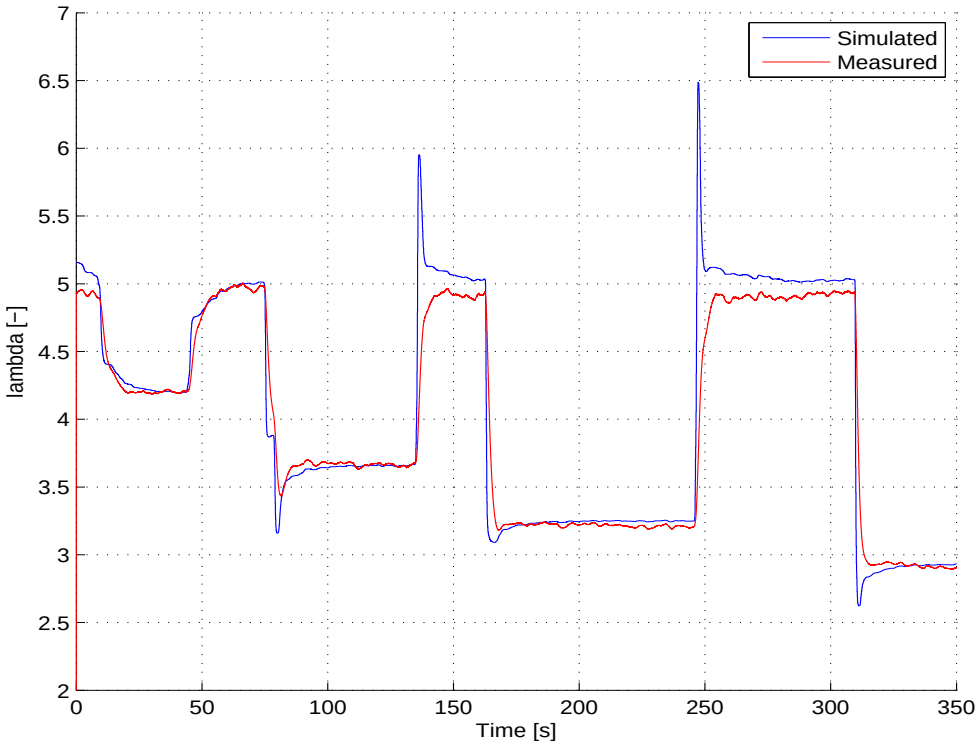

Figure 4.4: Measured and estimated value of lambda provided by the virtual sensor.

Chapter 5

Low Order Uncertain Dynamic Model of Lambda

In Chaps. 2 and 3, the differential equations that describe the dynamic behaviour of the engine were presented. Moreover, in Chap. 4, in order to derive the algebraic constraint equations the dynamic terms were assumed negligible in the analysis presented.

A problem of different nature is examined in this chapter. Precisely, the relative significance of the dynamic terms that appear in differential equations is considered. After the relative importance of the differential terms is known, simplifications are made and a low order dynamic model which can sufficiently capture the dynamic behaviour of the engine is derived. Additional comments are made about the qualitative characteristics of engine performance in different operating points. Finally, the plant and disturbance transfer functions that will be used for the controller implementation are also obtained in this chapter.

5.1 Full System of Non Linear Differential Equations

The differential equations which were obtained in Chaps. 2 and 3 for the ICE are summarized in this section in order to facilitate reading.

INTAKE MANIFOLD, COMPRESSOR, ENGINE and AIR COOLER: Eqs. 2.6, 2.19, 2.1 2.9, 2.56, 2.8 and 2.18

$$m_{im}T_{im} = \frac{p_{im}V_{im}}{R_a} \tag{5.1}$$

$$\frac{dm_{im}}{dt} = \dot{m}_c - \dot{m}_e \tag{5.2}$$

$$\frac{dp_{im}}{dt} = \frac{\gamma_a R_a}{V_{im}} \cdot \dot{m}_c \cdot T_{ac} - \frac{\gamma_a R_a}{V_{im}} \cdot \dot{m}_e \cdot T_{im} \tag{5.3}$$

$$\dot{m}_e = \frac{\eta_v V_{cyl} p_{im} z N_e}{R_a T_{im} 120} \tag{5.4}$$

$$\Pi_c = \frac{p_{im} + \zeta_{total} \frac{1}{2} \rho_3 c_3^2}{p_{amb}} \tag{5.5}$$

$$T_{ac} = ef \cdot T_w + (1 - ef) \cdot T_c \tag{5.6}$$

and

$$M_c = (\frac{1}{\omega_{tc}}) \cdot \dot{m}_c \cdot c_{pa} \cdot (T_c - T_{amb}) \tag{5.7}$$

EXHAUST MANIFOLD, ENGINE and TURBINE: Eqs. 3.16, 3.14, 3.1, 3.15 and 3.13

$$m_{em} T_{em} = \frac{p_{em} V_{em}}{R_g} \tag{5.8}$$

$$\frac{m_{em}}{dt} = \dot{m}_e + \dot{m}_f - \dot{m}_t \tag{5.9}$$

$$T_{exh} = \eta_{sc} \Pi_e^{1-1/\gamma_g} r_c^{1-\gamma_g} x_p^{1/\gamma_g - 1} (q_{in} (\frac{1 - x_{cv}}{c_{pg}} + \frac{x_{cv}}{c_{vg}}) + T_{im} r_c^{\gamma_g - 1}) \tag{5.10}$$

$$\frac{dp_{em}}{dt} = \frac{\gamma_g R_g}{V_{im}} \cdot (\dot{m}_e + \dot{m}_f) \cdot T_{exh} - \frac{\gamma_g R_g}{V_{em}} \cdot \dot{m}_t \cdot T_{em} - \dot{Q}_{em} \tag{5.11}$$

and

$$M_t = (\frac{1}{\omega_{tc}}) \cdot \dot{m}_t \cdot c_{pg} \cdot T_{em} \cdot \eta_{is,t} \cdot (1 - \Pi_t^{\frac{1-\gamma_g}{\gamma_g}}) \tag{5.12}$$

TURBOCHARGER ROTATIONAL DYNAMICS: Eq. 3.18

$$J_{tc} \cdot \frac{d}{dt}(w_{tc}) = M_t - M_c \tag{5.13}$$

In the following sections the operation point of the engine has to be defined. All physical variables at the operation point are at steady state and are denoted with *. As thoroughly explained in Chap. 4, two characteristic physical variables, namely: engine shaft speed ω_e and the fuel mass flow $\dot{m}_f$ are sufficient to estimate all the other physical variables in steady state. The turbocharger speed $N_{tc}^\star$, the compressor pressure ratio $\Pi_c^\star$ and the turbine pressure ratio $\Pi_t^\star$ can be computed from the static non-linear engine model given the engine shaft speed $\omega_e^\star$ and the fuel mass flow $\dot{m}_f{}^\star$.

5.2 Reduced Order System of Non-Linear Differential Equations

The temperature in the intake manifold inlet T_{ac} is assumed equal to the temperature at the intake manifold outlet T_{im}, under an isothermal assumpiton that is valid when a large heat transfer takes place. Moreover, the heat transfer that takes place in the exhaust manifold is considered to be negligible; thereby, $\dot{Q}_{em} = 0$. Similarly to the intake manifold case, the temperature T_{exh} is approximately equal to T_{em}. Finally, assuming that no pressure drop takes place in the air duct-from the cooler outlet to the engine inlet-and in the exhaust manifold, the equalities $p_{im} = \Pi_c \cdot p_{amb}$ and $p_{em} = \Pi_t \cdot p_{amb}$ are valid. These assumptions yield that

$$\frac{V_{im} p_{amb}}{R_a T_{im}} \cdot \frac{d\Pi_c}{dt} = \dot{m}_c(\Pi_c, N_{tc}) - \frac{\eta_v V_{cyl} z N_e p_{amb}}{R_a T_{im} 120} \cdot \Pi_c \tag{5.14}$$

$$\frac{V_{em} p_{amb}}{R_g T_{em}} \cdot \frac{d\Pi_t}{dt} = \frac{\eta_v V_{cyl} z N_e p_{amb}}{R_a T_{im} 120} \cdot \Pi_c + \dot{m}_f - \dot{m}_t(\Pi_t) \tag{5.15}$$

and

$$\frac{2\pi}{60} \cdot J_{tc} \cdot \frac{d}{dt}(N_{tc}) = M_t(\Pi_t, \dot{m}_f, \Pi_c, N_{tc}) - M_c(\Pi_c, N_{tc}) \tag{5.16}$$

where

$$T_{im} = T_{im}(\Pi_c, N_{tc}) \text{ and } T_{em} = T_{em}(\dot{m}_f, \Pi_c, N_{tc}) \tag{5.17}$$

The final equation from which the value of λ is computed is the following

$$\lambda = \frac{\dot{m}_e(\Pi_c)}{\dot{m}_f \cdot AFR_{st}} \tag{5.18}$$

so no effect of gas mixing is considered.

Equations 5.14, 5.15 and 5.16 define a system of non-linear differential equations which can be written as follows

$$\begin{aligned} \dot{\vec{x_1}} &= \vec{f}(\vec{x_1}, \vec{x_2}, \vec{u}, \epsilon) \\ \epsilon\dot{\vec{x_2}} &= \vec{g}(\vec{x_1}, \vec{x_2}, \vec{u}, \epsilon) \end{aligned} \tag{5.19}$$

where $\vec{x_1} = N_{tc}$, $\vec{x_2} = \binom{\Pi_c}{\Pi_t}$, $\vec{u} = \dot{m}_f$ and ϵ is a scalar used to define small quantities. The system of differential Eqs. 5.19 represents a wide class of systems. In [18] an overview of the validity of order reduction for the above class of systems and the simplifications made are examined. For $\epsilon = 0$ the system of differential equations becomes

$$\begin{aligned} \dot{\bar{\vec{x}}}_1 &= \vec{f}\bar{\vec{x}}_1, \bar{\vec{x}}_2, \bar{\vec{u}}, 0) \\ 0 &= \vec{g}(\bar{\vec{x}}_1, \bar{\vec{x}}_2, \bar{\vec{u}}, 0) \Leftrightarrow \bar{\vec{x}}_2 = \phi(\bar{\vec{x}}_1, \bar{\vec{u}}) \end{aligned} \tag{5.20}$$

Now the reduced order model is described with the following differential Eq.

$$\dot{\bar{\vec{x}}}_1 = \vec{f}[\bar{\vec{x}}_1, \phi(\bar{\vec{x}}_1, \bar{\vec{u}}), \bar{\vec{u}}] \equiv \bar{\vec{f}}(\bar{\vec{x}}_1, \bar{\vec{u}}) \tag{5.21}$$

According to [18], 5.21 is the reduced order non-linear differential equation for the system of non-linear differential equations 5.19 when ϵ is sufficiently small. Applying the same principles in the present case, the system of Eqs. 5.14, 5.15 and 5.16 is simplified to

$$\frac{d}{dt}(N_{tc}) = \frac{60}{2\pi} \cdot \frac{1}{J_{tc}}[T_t(\Pi_t, \dot{m}_f, \Pi_c, N_{tc}) - T_c(\Pi_c, N_{tc})] \tag{5.22}$$

with the constraints

$$\dot{m}_c(\Pi_c, N_{tc}) = \frac{\eta_v V_{cyl} z N_e p_{amb}}{R_a T_{im} 120} \cdot \Pi_c \tag{5.23}$$

and

$$\frac{\eta_v V_{cyl} z N_e p_{amb}}{R_a T_{im} 120} \cdot \Pi_c + \dot{m}_f = \dot{m}_t(\Pi_t) \tag{5.24}$$

Equations 5.23 and 5.24 lead to the following constraints-functions.

$$\Pi_c = f_{coem}(N_{tc}) \text{ and } \Pi_t = f_{tuem}(N_{tc}, \dot{m}_f) \tag{5.25}$$

Finally, substituting constaints 5.25 into Eq. 5.22 yields

$$\frac{d}{dt}(N_{tc}) = \frac{60}{2\pi} \cdot \frac{1}{J_{tc}}[T_t(N_{tc}, \dot{m}_f) - T_c(N_{tc})] \tag{5.26}$$

The 1^{st} order non-linear differential Eq. 5.26 along with the algebraic constraints 5.25 adequately describes the relatively slow load transients of the engine. Heuristically, model reduction is achieved by adding more constraints to a high order system; thereby, reducing the degrees of freedom, or equivalently the number of states, of it. As

mentioned in [18], the order reduction is connected to a family of techniques in which the fast dynamics of the system are neglected and only the slow ones are taken into account. Fast dynamics are associated with high frequencies of the system and their behaviour.

High-frequency dynamics can taken into account as multiplicative uncertainty. In this way the error steaming from order reduction is reduced. The weight of the multiplicative uncertainty is connected to the error introduced into the reduced model by neglecting high-frequency dynamics. In order to derive this frequency dependent weight the frequency range over which high frequency neglected dynamics considerable influence the system has to be estimated. The processes of evaluating the frequency range of the neglected dynamics and the error bounds can be performed for the linearised plant. For linear plants a wide range of techniques is available for order reduction and error bounds estimation.

5.3 Full System of Linear Differential Equations

Linearising Eqs. 5.14, 5.15 and 5.16 and collecting the coefficients of the same terms together, yields the following vector differential equation

$$\frac{d}{dt}\begin{pmatrix} N_{tc} \\ \Pi_c \\ \Pi_t \end{pmatrix} = \mathbf{J} \cdot \begin{pmatrix} N_{tc} - N_{tc}^{\star} \\ \Pi_c - \Pi_c^{\star} \\ \Pi_t - \Pi_t^{\star} \end{pmatrix} + \begin{bmatrix} \frac{60}{2\pi J_{tc}} \cdot \frac{\partial T_t}{\partial \dot{m}_f} \\ 0 \\ 1 \end{bmatrix} \cdot (\dot{m}_f - \dot{m}_f{}^{\star}) \tag{5.27}$$

where $\mathbf{J}$ is the Jacobian Matrix of the system of differential equations computed at the operation point $(N_{tc}^{\star}, \Pi_c^{\star}, \Pi_t^{\star})$

$$\mathbf{J}(N_{tc}^{\star}, \Pi_c^{\star}, \Pi_t^{\star}) = \begin{bmatrix} \frac{60}{2\pi J_{tc}}\left[\frac{\partial T_t}{\partial N_{tc}} - \frac{\partial T_c}{\partial N_{tc}}\right] & \frac{60}{2\pi J_{tc}}\left[\frac{\partial T_t}{\partial \Pi_c} - \frac{\partial T_c}{\partial \Pi_c}\right] & \frac{60}{2\pi J_{tc}}\frac{\partial T_t}{\partial \Pi_t} \\ \frac{R_a T_{im}}{V_{im} p_{amb}}\frac{\partial \dot{m}_c}{\partial N_{tc}} & \frac{R_a T_{im}}{V_{im} p_{amb}}\frac{\partial \dot{m}_c}{\partial \Pi_c} - \frac{\eta_v V_{cyl} z N_e}{120 V_{im}} & 0 \\ 0 & \frac{R_g T_{em} \eta_v V_{cyl} z N_e}{V_{em} R_a T_{im} 120} & \frac{R_g T_{em}}{V_{im} p_{amb}}\frac{\partial \dot{m}_t}{\partial \Pi_t} \end{bmatrix} \tag{5.28}$$

and the input matrix $\mathbf{B}$ at the same operation point is as follows

$$\mathbf{B}(N_{tc}^{\star}, \Pi_c^{\star}, \Pi_t^{\star}) = \begin{bmatrix} \frac{60}{2\pi J_{tc}} \cdot \frac{\partial T_t}{\partial \dot{m}_f} \\ 0 \\ 1 \end{bmatrix} \tag{5.29}$$

It is worth noting that all the derivatives appear in the matrices above are calculated at the operation point $(N_{tc}^{\star}, \Pi_c^{\star}, \Pi_t^{\star})$ which is a function of only the engine shaft speed $\omega_e^{\star}$ and the fuel mass flow $\dot{m}_f{}^{\star}$. Clearly, the engine behaviour around an operation point is fully defined if the functions and the corresponding derivatives of them that appear in the matrices above are known.

Additionally, similarly to the order reduction, approximating the non-linear model with a linear one can be taken into account by considering the effect of non-linear dynamics as input uncertainty.

5.4 Reduced Order System of Linear Differential Equations

The problem which is considered is the derivation of a low order linear model of lambda λ. The starting point is the reduced order non-linear differential equation that was obtained in 5.2. Equation 5.26 is linearised

$$\frac{d}{dt}(N_{tc}) = \frac{60}{2\pi J_{tc}}\left[\frac{\partial T_t}{\partial N_{tc}}(N_{tc} - N_{tc}^{\star}) + \frac{\partial T_t}{\partial \dot{m}_f}(\dot{m}_f - \dot{m}_f{}^{\star}) - \frac{\partial T_c}{\partial N_{tc}}(N_{tc} - N_{tc}^{\star})\right] \tag{5.30}$$

The value of lambda λ with the use of constraint 5.23 is computed by

$$\lambda = \frac{\dot{m}_c(N_{tc})}{\dot{m}_f \cdot AFR_{st}} \tag{5.31}$$

Linearising Eq. 5.31 by keeping only the first order terms of the Taylor expansion series yields

$$\lambda - \lambda^{\star} = \frac{1}{AFR_{st}\cdot \dot{m}_f{}^{\star}}\left[\frac{\partial \dot{m}_c}{\partial N_{tc}}(N_{tc} - N_{tc}^{\star}) + \dot{m}_c(N_{tc}^{\star}) \cdot \frac{-1}{\dot{m}_f{}^{\star}}(\dot{m}_f - \dot{m}_f{}^{\star})\right] \tag{5.32}$$

The Jacobian "matrix" for the reduced 1^{st} order system is given by

$$\mathbf{J}_r = \frac{60}{2\pi\cdot J_{tc}} \cdot \left[\frac{\partial T_t}{\partial N_{tc}} - \frac{\partial T_c}{\partial N_{tc}}\right] \tag{5.33}$$

and the input "matrix" is as follows

$$\mathbf{B}_r = \left[\frac{60}{2\pi \cdot J_{tc}} \cdot \frac{\partial T_t}{\partial \dot{m}_f}\right] \tag{5.34}$$

Applying the Laplace transformation and introducing the deviation variables $\delta y = y - y^{\star}$ in Eqs. 5.32 and 5.30 yields

$$\delta\lambda(s) = \frac{1}{AFR_{st}\cdot \dot{m}_f{}^{\star}}\left[\frac{\partial \dot{m}_c}{\partial N_{tc}} \cdot \delta N_{tc}(s) - \frac{\dot{m}_c(N_{tc}^{\star})}{\dot{m}_f{}^{\star}} \cdot \delta \dot{m}_f(s)\right] \tag{5.35}$$

and

$$\delta N_{tc}(s) = \frac{\frac{\partial T_t}{\partial \dot{m}_f}}{s - \left[\frac{60}{2\pi\cdot J_{tc}} \cdot \left(\frac{\partial T_t}{\partial N_{tc}} - \frac{\partial T_c}{\partial N_{tc}}\right)\right]} \cdot \delta \dot{m}_f(s) \tag{5.36}$$

Substituting Eq. 5.36 into Eq. 5.35 yields the transfer function

$$G_{\lambda}(s) = \frac{\left[\frac{\partial \dot{m}_c}{\partial N_{tc}}\frac{\partial T_t}{\partial \dot{m}_f}\frac{60}{2\pi\cdot J_{tc}} + J_r\cdot \dot{m}_c(N_{tc}^{\star})(\dot{m}_f{}^{\star})^2\right] - \left[\dot{m}_c(N_{tc}^{\star})\right]\cdot s}{\left[-AFR_{st}\cdot \dot{m}_f{}^{\star}\cdot J_r\right] + \left[AFR_{st}\cdot \dot{m}_f{}^{\star}\right]\cdot s} \tag{5.37}$$

Due to the fact that the exact value of the turbine's is-entropic efficiency $\eta_{is,t}$ is not known, the above transfer function contains one real uncertain parameter.

5.5 Model Analysis

5.5.1 Poles and Zeros

The **nominal** transfer function has one pole, located at the point:

$$s_p = J_r = \frac{60}{2\pi \cdot J_{tc}} \cdot \left[\frac{\partial T_t}{\partial N_{tc}} - \frac{\partial T_c}{\partial N_{tc}}\right] \tag{5.38}$$

Moreover, there is one real zero and it's location is at the point:

$$s_z = J_r + \frac{60}{2\pi \cdot J_{tc}} \cdot \frac{\partial \dot{m}_c}{\partial N_{tc}} \cdot \frac{\partial T_t}{\partial \dot{m}_f} \tag{5.39}$$

In order to detirmine the effect of poles and zeros in stability and performance their sign should be investigated.

As it have been mentioned in subsection 3.2.1, unlike the compressor that the air mass flow is a function of both the turbocharger shaft speed N_{tc} and the pressure ratio Π_c, turbine drives mass through it mainly due to the pressure ratio Π_t. For this reason the following equality is valid

$$\frac{\partial \dot{m}_t}{\partial N_{tc}}|(N_{tc}^\star, \Pi_c^\star, \Pi_t^\star) \ll \frac{\partial \dot{m}_c}{\partial N_{tc}}|(N_{tc}^\star, \Pi_c^\star, \Pi_t^\star) \tag{5.40}$$

The torque produced by the turbine and the compressor can be, in a simplified approach, considered mainly a function of the air mass flow and, consequently, obtain that

$$\frac{\partial T_t}{\partial N_{tc}}|(N_{tc}^\star, \Pi_c^\star, \Pi_t^\star) < \frac{\partial T_c}{\partial N_{tc}}|(N_{tc}^\star, \Pi_c^\star, \Pi_t^\star) \tag{5.41}$$

Consequently, the system is stable since the poles lies in the left half plane and no fundamental limitations are imposed to control as the zero is also located in the left half plane. Additionally, due to the presence of uncertainty in the real parameter $\eta_{is,t}$, the poles and zeros will lie within a region around the point of their the nominal location. The uncertainty is included in the terms $\frac{\partial T_t}{\partial \dot{m}_f}$ and $\frac{\partial T_t}{\partial N_{tc}}$.

5.5.2 Limiting behaviour of the transfer function

Moreover, the response of the engine in "very fast" and "very slow" fuel transients is investigated. In others words, the limiting behaviour of the magnitude $|G_\lambda(j\omega)|$, which is the frequency response of the transfer function $G_\lambda(s)$, when $j\omega \to \infty$ and $j\omega \to 0$ is examined.

For "very fast" fuel transients we have that $j\omega \to \infty$ and

$$|G_\lambda(j\infty)| = |\frac{-\dot{m}_c(N_{tc}^\star)}{AFR_{st} \cdot (\dot{m}_f{}^\star)^2}| = \frac{\lambda^\star}{\dot{m}_f{}^\star} \tag{5.42}$$

where $\lambda^\star$ is the steady state value of λ at the operation point $\dot{m}_f{}^\star, \omega_e^\star$. On the other hand, for "very slow" fuel transients we derive the following limiting behaviour of the frequency response

$$|G_\lambda(j0)| = |-\frac{\lambda^\star}{\dot{m}_f{}^\star} - \frac{\frac{60}{2\pi \cdot J_{tc}} \frac{\partial \dot{m}_c}{\partial N_{tc}} \frac{\partial T_t}{\partial \dot{m}_f}}{\dot{m}_f{}^\star \cdot AFR_{st} \cdot J_r}| = \frac{\lambda^\star}{\dot{m}_f{}^\star} + \frac{f(\lambda^\star)}{\dot{m}_f{}^\star} \tag{5.43}$$

where the function $f(\lambda^\star)$ is the product of the terms

$$f(\lambda^\star) = \frac{\frac{60}{2\pi \cdot J_{tc}} \frac{\partial \dot{m}_c}{\partial N_{tc}} \frac{\partial T_t}{\partial \dot{m}_f}}{AFR_{st} \cdot J_r} \tag{5.44}$$

and

$$J_r = \frac{60}{2\pi \cdot J_{tc}} \cdot [\frac{\partial T_t}{\partial N_{tc}} - \frac{\partial T_c}{\partial N_{tc}}] \tag{5.45}$$

All the derivatives that appear on the numerator of the expression 5.44 have positive values. Precisely, the mass of air delivered through the compressor $\dot{m}_c$ increases with the turbocharger speed N_{tc} and, similarly, the torque delivered by the turbine T_t is an increasing function of the fuel mass flow $\dot{m}_f$ due to the rise in the enthalpy of the exhaust gas in the turbine inlet. The critical term that determines the sign of the function is J_r. As it was illustrated in 5.5.1 this term is negative. Therefore, the following inequality inequality holds

$$|G_\lambda(j0)| < |G_\lambda(j\infty)| \tag{5.46}$$

between the "slow" and "fast" transients. In slow transients the additional term $\frac{f(\lambda^\star)}{\dot{m}_f{}^\star}$ decreases the magnitude of $|G_\lambda(j\omega)|$, which can be effectively viewed as the slope that connects variations in the fuel mass flow $\delta\dot{m}_f$ with the corresponding variations in $\delta\lambda$ from the steady state operation point $(\dot{m}_f{}^\star, \lambda^\star)$. Therefore, during slow transients we achieve a lower value of λ for the same decrease in the fuel mass flow $\dot{m}_f$ compared to fast fuel transients. However, we can achieve a higher value of λ for the same increase in the fuel mass flow $\dot{m}_f$ in comparison with fast fuel transients. By using an electric motor (EM) the variations in the torque demand of the internal combustion engine (ICE) become less sharp and slower and the same holds for the fuel mass flow. Thereby, as indicated by inequality 5.46 the slower dynamic yield a higher value of λ and consequently a less sharp drop during a load increase.

The reason for this behaviour can be explained with the air and fuel path dynamics. The fuel path dynamics are much faster than those of the air path and during fast transients they are the ones who dominate over the air path dynamics. A fuel variation almost instantly affects the air to fuel ratio inside the cylinder, while there is some time that should elapse before this variations in fuel could affect the air path mainly because of the dynamics associated with the turbocharger.

5.6 Parametrization of the Transfer Function

The transfer function is parametrized in the following way:

$$G(s) = K \cdot \frac{s - s_z}{s - s_p} \tag{5.47}$$

where K is the gain of the transfer function, s_z and s_p are the locations of the zero and pole of the transfer function, respectively.

Since the Jacobian matrices of the linear system depends on the operation point, a change in it will also result in a swift in the location of the poles and zeros. Moreover, the gain of the transfer function also varies with the operation point. The location of poles and zeros is shown in Fig. 5.1a and 5.1b, respectively as a function of the operating point.

Having these maps and knowing the operation point or operation range of the engine, its performance can be qualitatively evaluated. For instance, it can be observed that poles and zeros swift towards the positive right half plane when the load and engine's rotational speed is reduced. Therefore, it is expected a deterioration in the performance of the hybrid power-train in low-load and low-speed operating points.

The aforementioned maps provide also essential information for sea-going vessels with hybrid propulsion plant. In order to make use of the maps the fuel mass flow

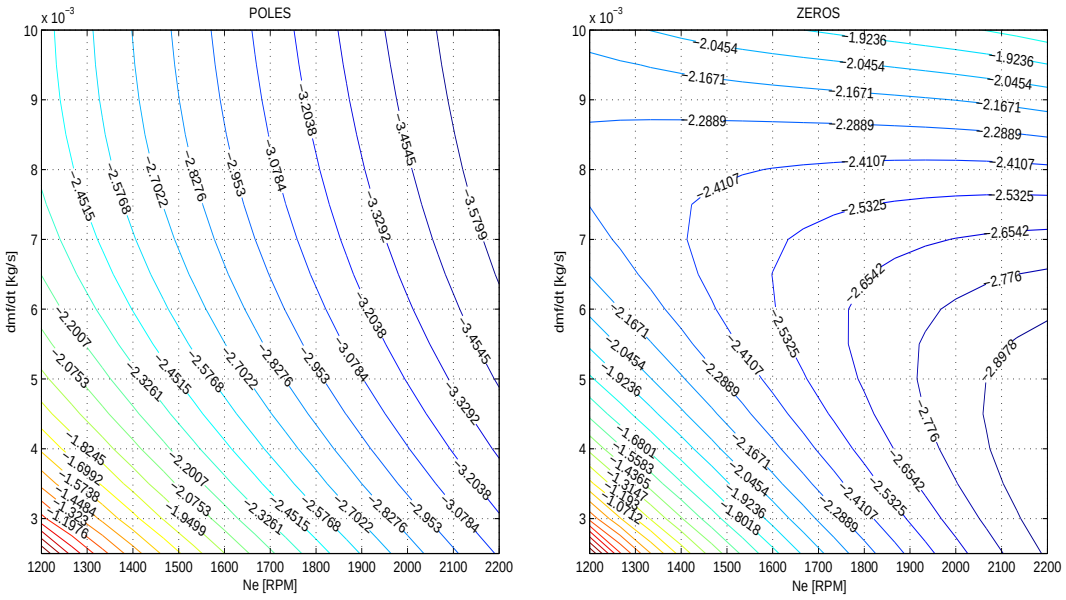

(a) Poles (b) Zeros

Figure 5.1: Engine poles and zeros map as a function of the operation point.

should be known. For seagoing vessels an approximate relationship between the torque shaft demand and the propeller rotational speed ω_p is valid; $M_{req} = C_p\omega_p^2$. In addition, for propulsion plants with reduction gear, ω_e and ω_p are connected with the relation $\omega_e = \omega_p/r_g$, where r_g is the reduction factor.

The fuel mass flow as a function of the engine speed can be found by substituting propeller demand equation into 4.16

$$\dot{m}_f = \frac{C_p/r_g^2}{H_{LV} \cdot ew} \cdot \omega_e^3 + \frac{M_{loss}}{H_{LV} \cdot ew} \tag{5.48}$$

By superimposing function 5.48 to the ICE maps insights can be gained about the performance of the ICE under different propeller load curves.

5.7 Linearisation of the hybrid powertrain model

In Chap. 3 every component of the power-train was modelled analytically. Afterwards, only the model of the ICE was simulated and the results were compared with the experimental measurements. In this section, two single-input single-output models will be derived from the non-linear analytic hybrid power-train model.

For λ-control, the plant model and the disturbance model have to be computed. The plant model, refered as G, is the transfer function with input the command to the frequency inverter of the electric motor-cmd and output the value of λ, while the disturbance model is represented with G_d and has input the change in reference value of torque to the disturbance model-T_d and the same output as G.

Model linearisation can be performed analytically, as presented in the previous section, by the calculation of the Jacobian matrix of the non-linear system. Clearly this

process is useful for getting insights about the effect of the various model parameters in system dynamics and about the performance of the ICE in numerous operating points. However, the manual computation of the Jacobian matrices is not efficient. For this reason, the linearisation of the whole hybrid model is based on the computational power of Matlab-Simulink.

From the discussion in the previous sections of this chapter, it is clear that the non-linear first order differential Eq. 5.26 along with the constraint Eqs. 5.25 adequately describe the dynamic behaviour of the ICE for sufficiently slow transients. The model of the ICE is presented in the aforementioned way as a Simulink model, in which each individual component of the ICE corresponds to a Simulink-block and the coupling between separate components is taken into account by considering the connection of the signal lines.

In order to calculate the linearised plant, an operation point of constant input values u_0 and initial level of the integrators x_0 has to be defined [1]. For this reason, the system is simulated with the desirable input values and when the transient phenomenon has declined-thus, the states are at steady state-the model is linearised with Matlab command **linearize**.

In the operating point of linearisation, the torque produced by the ICE is T_{sp} = $300Nm$ and the additional torque T_d = $100Nm$, considered as a disturbance, is the load received by the EM that produces T_{em} = $100Nm$ at cmd = $0.041V$. The rotational speed of the shaft is 1600 RPM, common for both the ICE and the EM. When the input vector has been defined and the operation point has been computed, the nominal model is linearised.

The resulting plant is of high order and this may also lead to a high order controller. High order controllers cause problems associated with reliability and maintenance in a practical control application [12]. Moreover, low orders controllers improve the numerical properties of the *mu*-synthesis algorithm as it will be mentioned in Sec. 6.2. For this reason the initial-high order controller is reduced and the bode plot of the initial models along with reduced 4th order transfer function of the original plant transfer function G and the reduced 5th order transfer function of the original disturbance transfer function G_d are shown in Fig. 5.2.

5.8 Linear Uncertain Transfer Function

Table 5.1 summarizes all the uncertain real parameters and uncertain transfer functions that appear in the hybrid power-train model.

Table 5.1: Uncertain Terms

Name	Symbol	Uncertainty Type
Uncertain Willans Parameter	δ_{ew}	Uncertain Real Parameter
Uncertain Willans Parameter	$\delta_{p_{lm}}$	Uncertain Real Parameter
Uncertain Is-entropic efficiency	$\delta_{\eta_{is,t}}$	Uncertain Real Parameter
Uncertain Rotational Acceleration Transfer Function	$\Delta_{\dot{N}_e}$	Uncertain Transfer Function
High Frequency Dynamics	Δ_{hf}	Uncertain Transfer Function
Non-linear Dynamics	Δ_{nl}	Uncertain Transfer Function

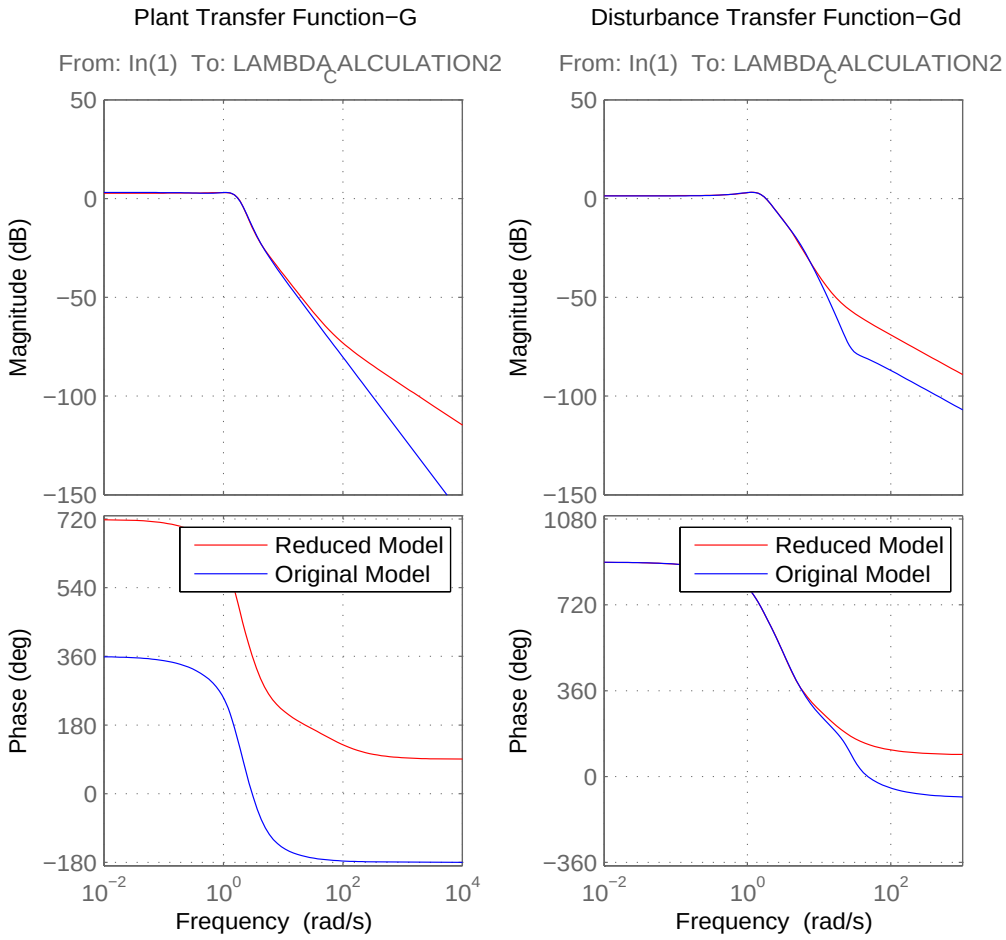

Figure 5.2: Bode diagram of the original transfer functions G, G_d (blue line) and the reduced ones G_{rd}, $G_{d,rd}$.

Now that all the uncertain terms presented in the system have been identified, a decision has to be made regarding the way in which uncertainty will be modelled. Clearly, there is substantial freedom in this choice, since various approaches can be adopted. The possible ways of dealing with uncertainty range from very conservative designs (for instance, lumping all uncertainty parameters in a single perturbations block) to very marginal designs, where the uncertainty has a structure specified by the nature of the problem with no simplifications made. A general rule, regarding uncertainty representation, is that conservative designs-large region of uncertainty-demonstrate poor performance but they can maintain their properties over a wider range of operation points in contrast to marginal designs-narrow uncertainty range-where performance drastically deteriorates when the operation point swifts far from the nominal.

The uncertain non-linear model is linearised for the three different operating points shown in Table 5.2 using matlab function **ulinearize**. The bode digram of the uncertain disturbance transfer functions-each of them linearised at different operating point-as well as the reduced order nominal transfer function is shown in Fig. 5.3a and the corresponding graph of the uncertain and nominal plant transfer functions is given in Fig. 5.3b.

Table 5.2: Operation Points of Linearisation

Model No	T_{sp} [Nm]	T_d [Nm]	*cmd* [V]	N_e [RPM]	*Time Instant of Snapshot* [s]
1	300	50	0.025	1600	20
2	300	100	0.041	1600	20
3	300	150	0.0615	1600	20

The proposed modelling of the uncertainty is as follows:

1. One [1x1] full complex uncertain linear time invariant transfer function block and less than one in magnitude, denoted by Δ_G, is introduced to compensate for all the uncertain terms in the plant transfer function G.

2. One [1x1] full complex uncertain linear time invariant transfer function block and less than one in magnitude, denoted by Δ_{G_d}, is introduced to compensate for all the uncertain terms in the disturbance transfer function G_d.

The final uncertain transfer function of the plant model is

$$G = G_n \cdot (1 + W_G \Delta_G) \tag{5.49}$$

and the disturbance transfer function is

$$G_d = G_{d_n} \cdot (1 + W_{G_d} \Delta_{G_d}) \tag{5.50}$$

where the subscript $_n$ denotes the nominal model and W is the uncertainty weight of the transfer functions appropriately computed to cover the whole range of responses. The weight of the multiplicative uncertainty for the plant and the disturbance transfer functions is computed in the same way as in subsection 3.10.3 and it is illustrated in Fig. 5.4.

The plant and disturbance model are utilized for the controller implementation which is described in Sec. 6.4. In order to validate the deterioration of performance

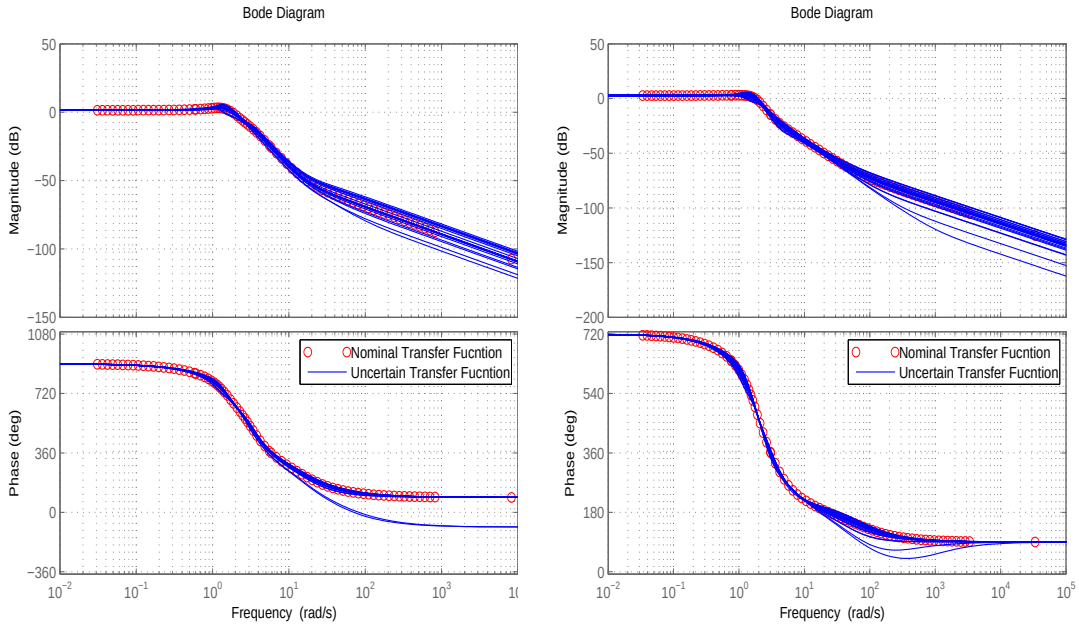

(a) Disturbance transfer function.

(b) Plant transfer function.

Figure 5.3: Bode plot of the uncertain and the reduced transfer functions.

of the hybrid-electric powertrain in the low speed and low torque operation range, as proposed in Sec. 5.6, the process of deriving a uncertain plant and disturbance transfer function is repeated for shaft speed 1500 RPM.

5.9 Derivation of a Linear Uncertain Model for a Propeller Loading

When a propeller load is applied to the hybrid propulsion plant, the torque demand is determined by the engine rotational speed according to the relation $M_{req} = C_p/r_g^2\omega_e^2$. Given the propeller constant C_p and the range of torque demand, the uncertain linear system can be evaluated. Table 5.3 presents the characteristics of the propeller load.

Table 5.3: Propeller load characteristics

Propeller Constant-C_p[Nm/(rad/s)]	Torque Range [Nm]	Speed Range [rad/s]
0.01467	[200:550]	[1100:1900]

The process of deriving the nominal and the uncertain plant and disturbance transfer functions is similar to the step load-case and the points of linearisation are illustrated in Table 5.4. However, for the propeller load the region of the uncertainty is substantially larger compared to the step load-case, since the operating points of the engine lie within a wider region. This fact has to be taken into consideration when the specification of the closed loop plant are determined. The wider range of uncertainty comes at the expense of performance and, in our case, disturbance rejection requirement are

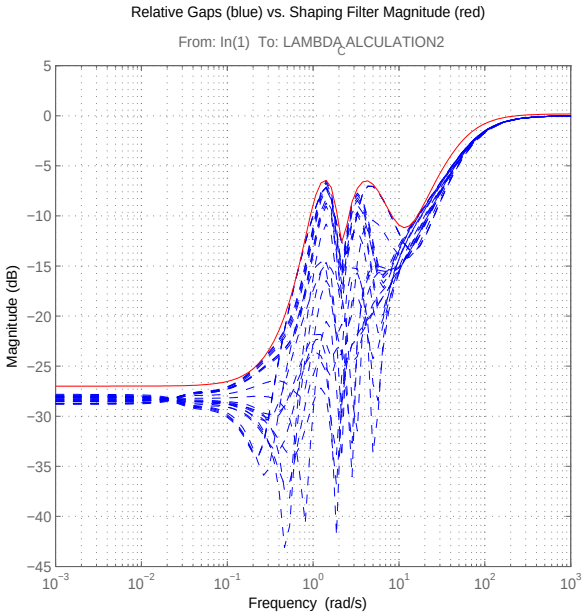

(a) Plant transfer function.

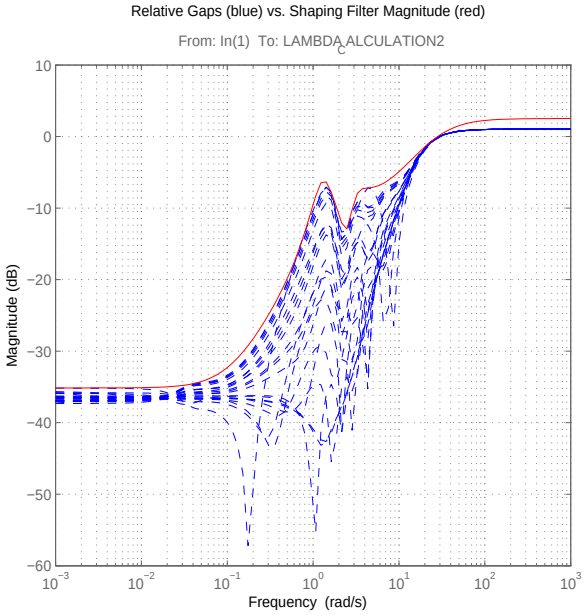

(b) Disturbance transfer function.

Figure 5.4: Bode plot of the uncertainty weight.

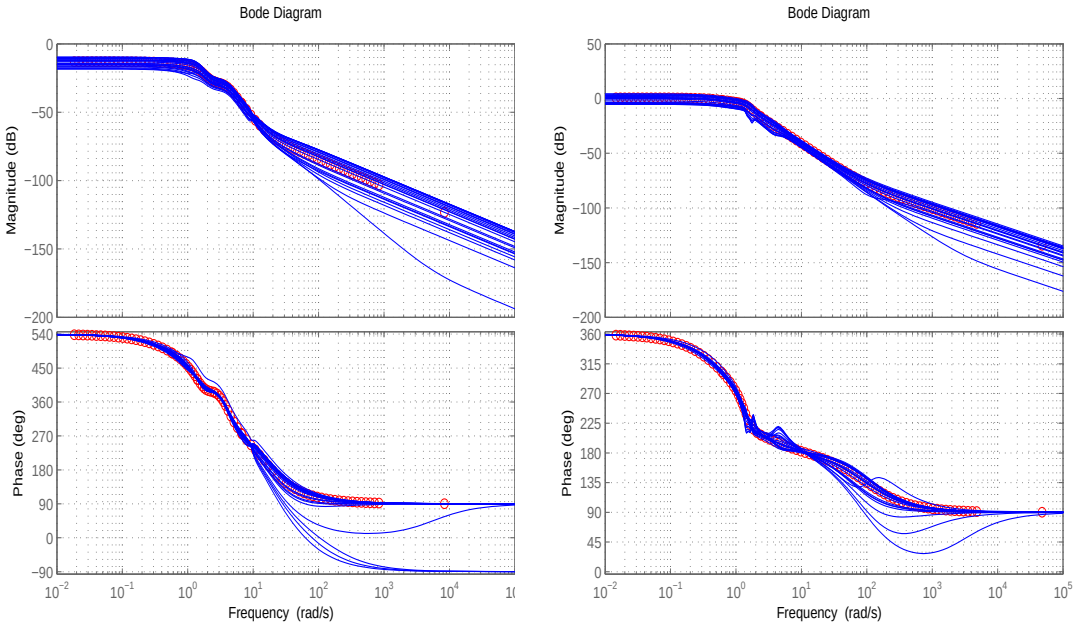

(a) Disturbance transfer function.

(b) Plant transfer function.

Figure 5.5: Bode plot of the uncertain and the reduced transfer functions for propeller load.

more relaxed compared to the step load case.

Table 5.4: Operation Points of Linearisation for Propeller Load

Model No	T_{sp} [Nm]	T_d [Nm]	*cmd* [V]	N_e [RPM]	*Time Instant of Snapshot* [s]
No1	193	25	0.01025	1100	20
No2	270	25	0.01025	1300	20
No3-Nominal	**360**	**25**	**0.01025**	**1500**	**20**
No4	463	25	0.01025	1700	20
No5	577	25	0.01025	1900	20

The bode digram of the uncertain disturbance transfer functions for propeller load-each of them linearised at different operating point-as well as the reduced order nominal transfer function is shown in Fig. 5.5a and the corresponding graph of the uncertain and nominal plant transfer functions is given in Fig. 5.5b.

Chapter 6

Controller Design

In this chapter, a feedback controller is proposed for λ-control during load transients of the hybrid-electric powertrain. The controller is designed based on the linearised models acquired in Chap. 5. Additionally, the robust stability and performance of the controller were evaluated before the implementation of the λ-controller for the experimental hybrid-electric powertrain of the LME, through the computation of the closed loop transfer functions.

6.1 Feedback Control

Controllers can be categorized as one and two degrees of freedom depending on the number of their inputs. The fundamental difference between these two type of controllers is the fact that the one degree of freedom (1 DOF) controller is fed with the measured error while the two degrees (2 DOF) controller is fed both with the measured signal and the reference value. The 1 DOF configuration is presented in Fig. 6.1a and the general scheme of a 2 DOF controller is illustrated in Fig. 6.1b.

As mentioned in the previous paragraph, the controller input in the one degree of freedom case is the measured error $e_m = r - y_m$ where $y_m = y + n$ is the measured signal that includes the noise n which is induced into the system. The disturbances entering the system are symbolized with d and affect the real output of the system through the

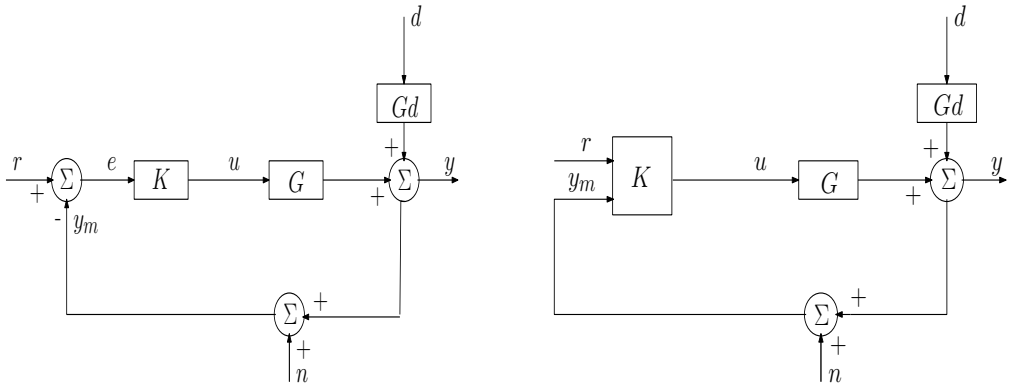

(a) 1 DOF controller (b) 2 DOF controller

Figure 6.1: Block diagram of controllers with different degrees of freedom.

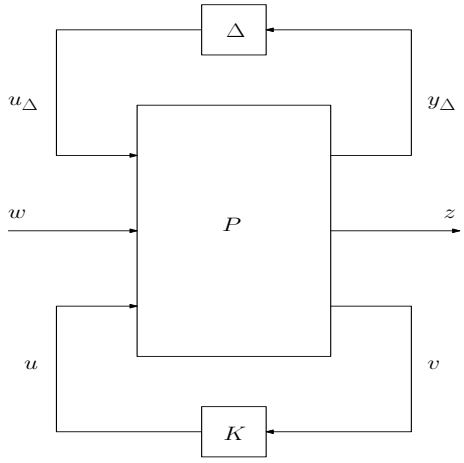

Figure 6.2: General configuration for controller synthesis, P-structure.

function G_d. The actual error is defined is the real output y is subtracted from the reference value r. The same definitions and symbols are used for the 2 DOF controller with the only difference that the controller input is the vector signal $v = \binom{y_m}{r}$.

6.2 Structured Singular Value (SSV) Framework

6.2.1 General control synthesis and performance analysis configurations

The starting point of the controller synthesis is the generalized plant, illustrated in Fig. 6.2, where the uncertainty and the controller have been "pulled out". The uncertain elements are collected in one block diagonal matrix Δ, with a specific structure, and the block of the controller is denoted as K. Additionally, w is the vector of the exogenous inputs and disturbances, z is the vector of the exogenous outputs, u is the input from the controller to the plant and v is the measured signals fed into the controller. Finally, the outputs and the inputs of the uncertain block are denoted as u_Δ and y_Δ respectively.

The generalized plant P can be easily derived if we know the block diagram of the system, only by using available software. In Matlab Robust Control Toolbox there is no need for the user to "pull out" the uncertainty of the plant; therefore, there is a benefit for the user to avoid manual computations.

Alternatively, if the objective of the problem is to analyse the uncertain system that incorporates the controller, the $N\Delta$-structure shown in Fig. 6.3 will be used. The relationship among N, P and K is given by a lower linear fractional transformation

$$N = F_l(P, K) = P_{11} + P_{21}K(I - P_{22}K)^{-1}P_{21} \tag{6.1}$$

Moreover, in order to examine robustness it is essential to know the uncertain closed-loop transfer function, that incorporates both the controller and the uncertainty. This function, defined from w to z, can be computed from the upper linear fractional transformation of N and Δ

$$F = F_u(N, \Delta) = N_{22} + N_{21}\Delta(I - N_{11}\Delta)^{-1}N_{12} \tag{6.2}$$

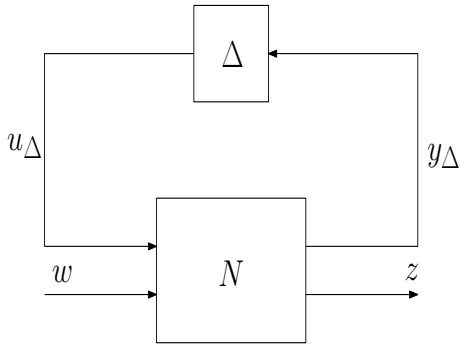

Figure 6.3: General configuration for robustness analysis, $N\Delta$-structure.

6.2.2 Definition of nominal and robust stability and performance

Nominal Stability: The requirement for nominal stability can be satisfied by demanding the whole matrix N be internally stable.

$$N \quad \text{is internally stable} \tag{6.3}$$

Nominal Performance: For nominal performance, $\Delta = 0$, we require for all the normalized disturbances and references w, the normalized errors z to be less than one in magnitude. This requirement can be mathematically formulated as follows

$$\|F\| = \|F_u(N,0)\|_\infty = \|N_{22}\|_\infty < 1 \quad \text{and NS} \tag{6.4}$$

Robust Stability: For robust stability, we require the transfer function $F = F_u(N,\Delta)$ function defined from the normalized disturbances and references w to the normalized errors z be stable for all allowed Δ, $\|\Delta\|_\infty \leq 1$

$$F = F_u(N,\Delta) \quad \text{is stable} \quad \forall \Delta, \|\Delta\|_\infty \leq 1 \quad \text{and NS} \tag{6.5}$$

Robust Performance: Robust performance is guaranteed if the normalized errors z are less than one in magnitude for all the allowed normalized disturbances and references w and Δ, $\|\Delta\|_\infty \leq 1$

$$\|F\|_\infty < 1 \quad \text{is stable} \quad \forall \Delta, \|\Delta\|_\infty \leq 1 \quad \text{and NS} \tag{6.6}$$

The problem with the definition of RS and RP is that they cannot be practically tested, since they involve to check the aforementioned conditions over an infinite set of allowed uncertain elements [42]. For this reason, the structured singular value μ of a matrix M is introduced.

6.2.3 The structured singular value μ

Definition 6.1. Let M be a given complex matrix and $\Delta = diag\{\Delta_i\}$ denote a set of uncertain complex matrices with a given block-diagonal structure (in which some of the blocks may be repeated and some may be restricted to be real). The real non-negative function $\mu(M)$, called structured singular value, is defined by

$$\mu(M) = \frac{1}{\min\{k_m | det(I - k_m M\Delta) \text{ for structured } \Delta, \bar{\sigma}(\Delta) \leq 1\}} \tag{6.7}$$

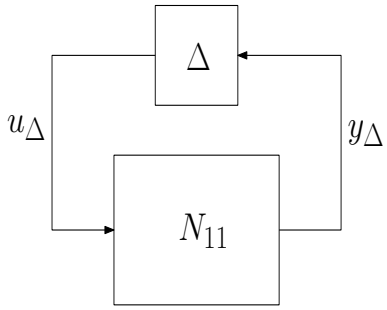

Figure 6.4: Robust stability analysis configuration.

The structured singular value μ, depending on the structure of uncertainty Δ, can be given by different norms. Precisely, the above extreme bounds are valid:

$$\text{If } \Delta \text{ is a full complex matrix, then } \mu(M) = \bar{\sigma}(M) \tag{6.8}$$

and

$$\text{If } \Delta = \delta I,\ \delta \text{ is complex scalar, then } \mu(M) = \rho(M) \tag{6.9}$$

For complex perturbations the lower bound of the structured singular value is the spectral radius while the upper bound is the singular value; thereby, the following inequality is valid

$$\rho(M) \leq \mu(M) \leq \bar{\sigma}(M) \tag{6.10}$$

In [49], the improved-tighter lower and upper bounds of μ are given

$$max_{U \epsilon \mathcal{U}}\{\rho(UM)\} \leq \mu(M) \leq min_{D \epsilon \mathcal{D}}\{\bar{\sigma}(DMD^{-1})\} \tag{6.11}$$

where U is any unitary matrix with the same structure as Δ and D is any matrix that commutes with Δ, that is, $\Delta D = D\Delta$. One should note that the lower bound is always an equality as mentioned in [49].

Having defined the structured singular value μ, the requirement for RS is given by

$$\mu_\Delta(N_{11}) < 1,\ \forall\omega \text{ and NS} \tag{6.12}$$

where N_{11} is the matrix that connects y_Δ with u_Δ and Δ is the block diagonal matrix of the uncertain elements. Moreover, the structure used for the determination of the robust stability is illustrated in Fig. 6.4 where the term N_{11} connects the output y_Δ with the input u_Δ.

Similarly, RP can be tested using the structured singular value as follows

$$\mu_{\tilde{\Delta}}(N) < 1,\ \forall\omega, \tilde{\Delta} = \begin{bmatrix} \Delta & 0 \\ 0 & \Delta_P \end{bmatrix},\ \text{and NS} \tag{6.13}$$

Unlike Δ that has structure specified by the type of uncertain elements, Δ_P is always a full complex matrix and does not have any immediate physical interpretation. Thus the requirement of RP is equivalent to the RS of the structure presented in Fig. 6.5.

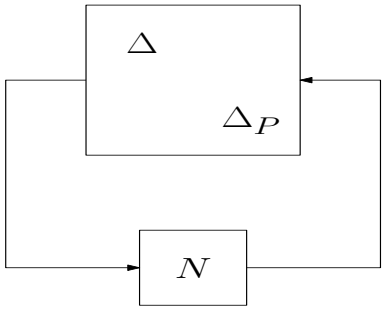

Figure 6.5: Robust performance analysis configuration.

6.2.4 Controller synthesis

It is worth noting that no direct method to synthesize an μ-optimal controller exists [42]. However, for complex perturbations, an approximate method known as DK-iteration is available, with the results obtained from it usually been satisfactory. This method is a combination of the H_∞-synthesis and μ-analysis. The starting point of DK-iteration is the minimization of the upper bound of inequality 6.11 over the whole frequency range. This statement can be mathematically formulated as follows

$$min_K\{min_{D\epsilon\mathcal{D}}\{\bar{\sigma}(DND^{-1})\}\} \tag{6.14}$$

As can be easily seen from Eq. 6.14, the process of controller synthesis involves the following iterative procedure:

1. K-step: Synthesize an H_∞ controller for the scaled problem, $min_K\{\bar{\sigma}(DN(K)D^{-1}\}\}$ with fixed $D(s)$.

2. D-step: Find $D(j\omega)$ to minimize at each frequency $\bar{\sigma}(DN(j\omega)D^{-1})$ with fixed N.

3. D-step: Fit the magnitude of each element of $D(j\omega)$ to a stable and minimum phase transfer function $D(s)$ and go to Step 1.

Some interesting notes have to be made in this point. Although, the lower bound is tight, as it was mentioned in the previous subsection, the quantity $max_{U\epsilon\mathcal{U}}\{\rho(UM)\}$ can have multiple local maxima that are not global [49]. However, one should also take into account that the optimization algorithm can still converge to a suboptimal solution even when the upper bound is minimized. This problem can occur because the combined optimization problem is not convex, despite the fact that each step, treated separately, is convex.

Additionally, the numerical properties of the optimization algorithm are improved by using a low order fit and transfer function. For this reason, low order transfer function and weights are preferred. Finally, the main problem associated with the upper bound is that it is not always equal to μ. Whether the μ and its bound are equal depends on the uncertainty structure.

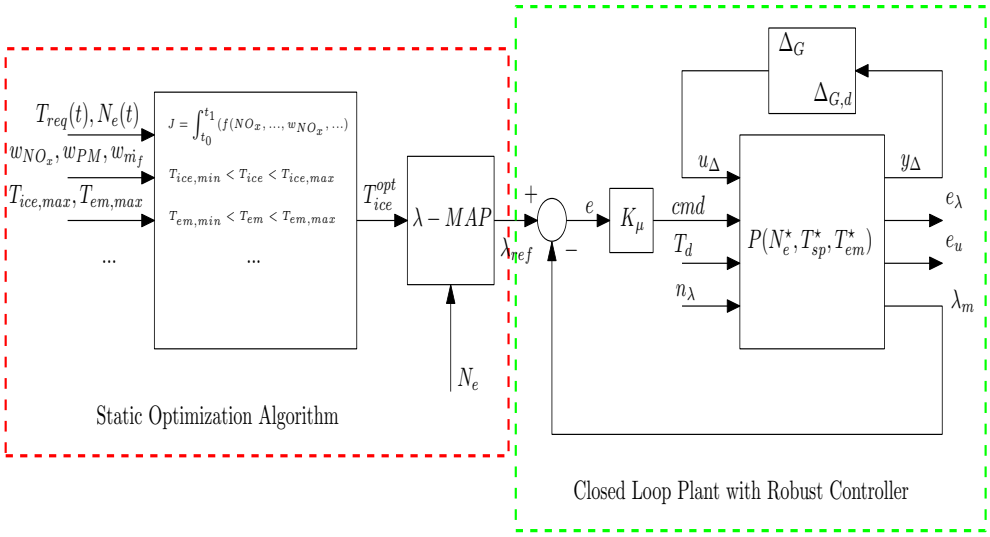

Figure 6.6: Robust controller and static optimization algorithm.

6.3 Reference Signal

The reference signal λ_{ref} is provided by a high level static optimization algorithm. Firstly, the static optimization algorithm splits the torque demand to the internal combustion engine T_{ice} and the electric motor T_{em} so the performance of the hybrid power train is optimal in quasi-static conditions. The optimization problem consists of a cost minimization of appropriately weighted functions of NO_x, PM, fuel consumption $\dot{m}_f$ and battery state of charge SOC under various constraint equations.

The solution to the optimization problem is provided as a [2x1] vector of the optimal internal combustion engine and electric motor torque $[T_{ice}^{opt}, T_{em}^{opt}]^T$. However, even when the static optimization algorithm provides the global optimal solution and not a suboptimal one, the performance of internal combustion engine (ICE) in load transient conditions substantially deviates from acceptable let alone optimal. For this reason, the optimal torque T_{ice}^{opt} and the engine rotational speed N_e are utilized as inputs to a two dimensional map from which the steady state value of $\lambda_{ref}(T_{ice}^{opt}, N_e)$ is derived. Additionally, the difference between the torque produced by the internal combustion engine from the optimal, as specified from the optimization algorithm, for a certain time instant is considered as disturbance acting in the system $T_{dis}(t) = T_{ice}^{opt}(t) - T_{ice}(t)$.

The present thesis deals with the dynamic control and the process of deriving the quasi-static reference is not considered. The control configuration is depicted in Fig. 6.6.

6.4 Controller Implementation

The generalized system P where the uncertainty and the controller have been "pulled out" is illustrated in Fig. 6.7 and a simplified version of this diagram, used for controller synthesis, is depicted in Fig. 6.8. In order to derive the generalized plant P two possible aproaches can be adopted. One approach of computing P is through Matlab either by representing system interconnection in Simulink or source code [4]. Another possible

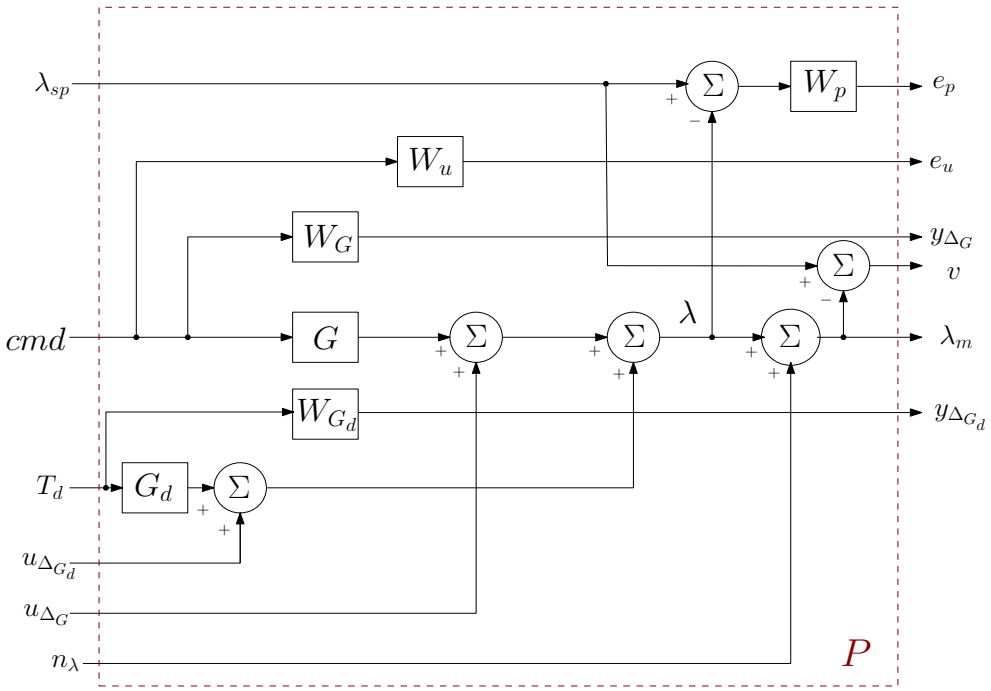

Figure 6.7: Analytic block diagram of the uncertain plant. Uncertainty has been pulled out.

way of dealing with the problem, which applies to less complex cases, is by manual computations. In the latter case the equations of the system can be written down and then the terms are rearranged so the matrix P that connects inputs with outputs can be derived. The interconnection matrix P is as follows

$$\mathbf{P} = \begin{pmatrix} 0 & 0 & 0 & W_{G_d} & 0 & 0 \\ 0 & 0 & 0 & 0 & 0 & W_G \\ -W_p & -W_p & 0 & W_p G_{d,n} & -W_p & W_p G_n \\ 0 & 0 & 0 & 0 & 0 & W_u \\ -1 & -1 & W_n & -G_{d,n} & -1 & G_n \end{pmatrix} \tag{6.15}$$

In the above representation W_p is the performance weight, appropriately chosen so that the closed loop plant match the designer's response specifications. The general representation of the performance weight is given by

$$W_p(s) = \frac{(s/M^{1/n} + \omega_B^\star)^n}{(s + \omega_B^\star A^{1/n})^n} \tag{6.16}$$

where A is the value that $1/W_p(s)$ takes at low frequencies, M is the asymptotic value of $1/W_p(s)$ at high frequencies and $\omega_B^\star$ is the frequency at which the asymptote crosses 1. The parameter n determines the steepness-roll off rate of the weight.

The requirement of a steady state error close to zero is reflected to the choice of the parameter A, which is a sufficiently small quantity. Parameter M is directly related to the overshoot of the system. The higher the magnitude of this factor the higher the overshoot presented in the system. Finally, parameter $\omega_B^\star$ determines the bandwidth

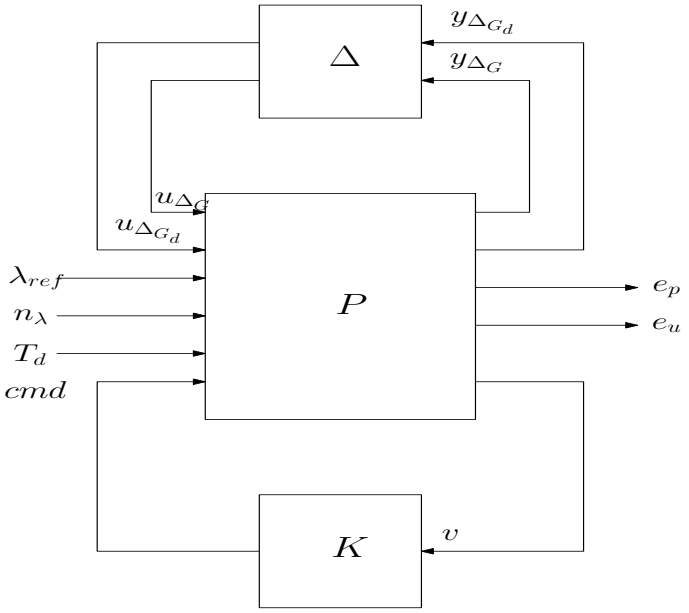

Figure 6.8: Simplified block diagram of the uncertain plant. Uncertainty has been pulled out.

of the closed loop system. Generally speaking, large bandwidth correspond to system with fast response and oscillatory behaviour. On the contrary, small bandwidth is a characteristics of sluggish systems but with small overshoot.

Regarding the input command weight the assumption that it can be represented as W_p is made. However, it is desirable to specify $1/W_u$ to have a value close to zero in high frequencies in order to make controller less sensitive in noise; thereby, in this case M has a large value. On the other hand, the magnitude of A has a large value to allow large commands and tight control in small frequencies.

The following table illustrates the selected parameters of the performance and input weights for the plant and disturbance model derived in :

Table 6.1: Selected Weight Parameters

Weight Symbol	A	M	$\omega_B^\star$	n
W_p	0.07	2	0.17	1
W_u	2	0.175	2	1

The controller is implemented for the plant transfer function derived in Sec. 5.8 with the aid of MATLAB and the value of $\gamma = \|(DND^{-1})\|_\infty$ achieved is 1.3657. This controller correspond to the plant derived for shaft speed 1600 RPM. In Sec. 6.5, the analysis of the controller designed for this plant is presented.

In addition to the aforementioned controller, another controller is also developed for the plant that was obtained for shaft speed 1500 PRM with exactly the same performance requirements. In this case, the value of $\gamma = 1.3955$; thus, it is expected a deterioration in performance; this fact which accords with the discussion presented in Sec. 5.6. The presentation of performance and stability analysis of the latter controller

is omitted from the following section.

6.5 Closed Loop System Analysis

After the controller has been obtained the question that arises is whether the closed loop system achieves the performance requirements determined from the designer. The starting point of closed loop analysis is the $N\Delta$-structure.

6.5.1 Nominal Performance

Nominal performance can be determined, as mentioned in subsection 6.2.2 from the H_∞-norm that connects the input vector $w = [n \quad d \quad r]^T$ with the output vector $z = [e_p \quad e_u]^T$. This matrix can be represented by N_{22} and is given by

$$\mathbf{N}_{22} = \begin{pmatrix} W_p G_n K S_o W_n & -W_p G_{d,n}(1 - G_n K S_o) & -W_p(1 - G_n K S_o) \\ -W_u K S_o W_n & -W_u K S_o G_{d,n} & W_u K S_o \end{pmatrix} \tag{6.17}$$

The nominal performance in terms of disturbance rejection and reference tracking can be formulated by the requirement that the singular values $\sigma_i(\cdot)$ or equivalently the magnitude (since there are scalar quantities) of the terms $G_{d,n}(1 - G_n K S_o)$ and $(1 - G_n K S_o)$ lie below the inverse of the performance weight, $1/W_p$, respectively. This condition is satisfied as can be seen from Fig. 6.9a. Moreover, the magnitude of the controller command should not exceed the specified weight $1/W_u$. As can be seen from Fig. 6.9b this requirement is not fulfilled but the violation of the condition is only marginal.

6.5.2 Robust Stability

In the case of structured uncertainty matrix Δ, stability analysis has to be performed by the computation of the structured singular value $\mu_\Delta(N_{11})$ where

$$\mathbf{N}_{11} = \begin{pmatrix} 0 & 0 \\ -W_G K S_o & -W_G K S_o \end{pmatrix} \tag{6.18}$$

Since no algorithm is available for the exact computation of μ, the robust stability analysis is based of the estimation of the quantity from its upper and lower bound.

The requirement of robust stability has been mathematically formulated in subsection 6.2.2 and it is evident from Fig. 6.10 that RS is achieved, as $\mu < 1$ over the whole frequency range. The lower bound of stability margin, defined as the reciprocal of the maximum μ over the frequency range, is $SM = 12.39$. The physical interpretation of this quantity is that the system remains stable for all uncertainty values smaller than 12.39 and at least one collection of uncertain elements with magnitude equal to 12.39 exists which can cause instability [12].

6.5.3 Robust Performance

For the determination of robust performance the structure that is depicted in Fig. 6.3 which integrates the controller, the uncertainty and the performance weights, specified in the design process to achieve the closed-loop desirable response characteristics, is

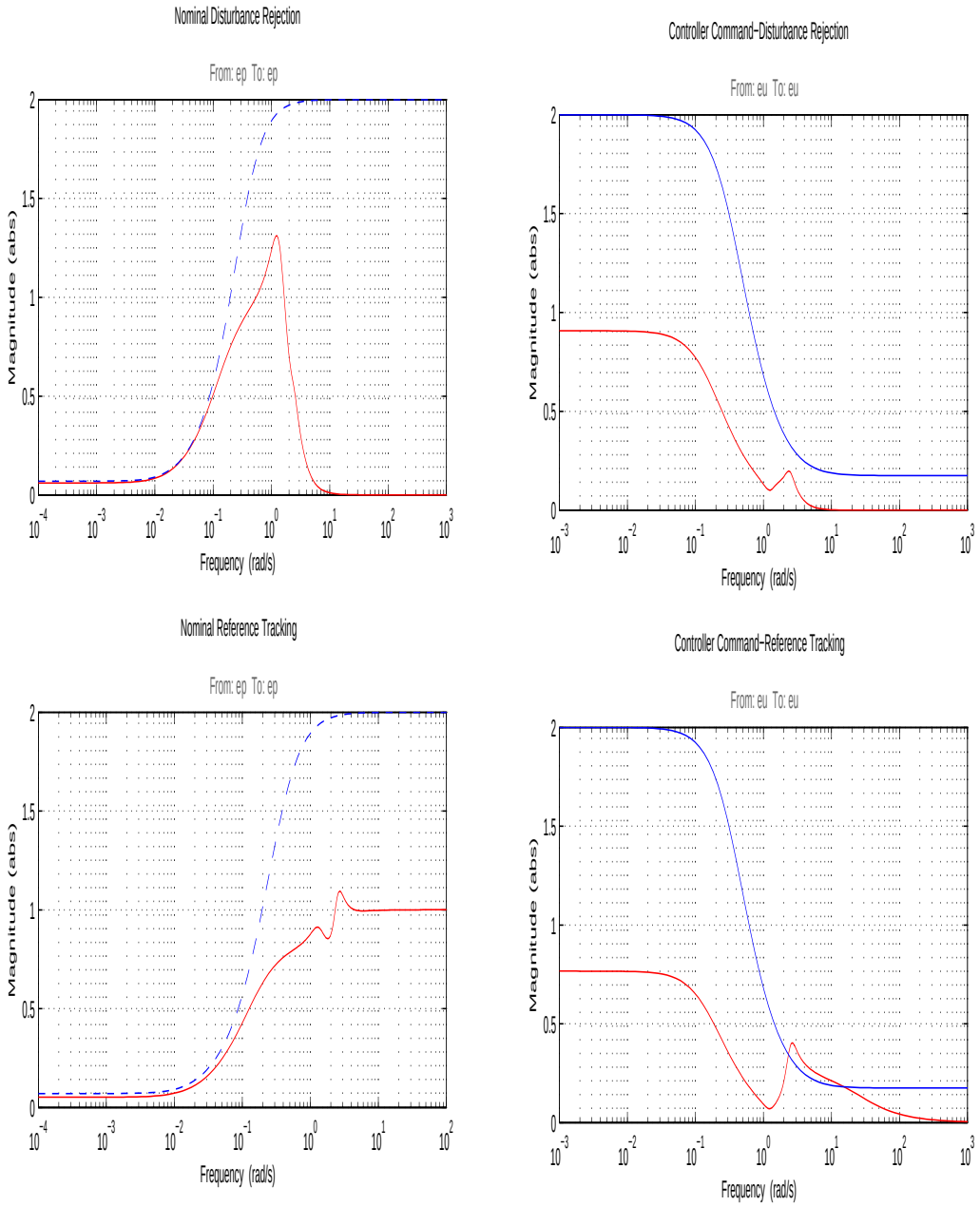

(a) Disturbance rejection and reference tracking performance.

(b) Input command specifications.

Figure 6.9: Nominal performance analysis.

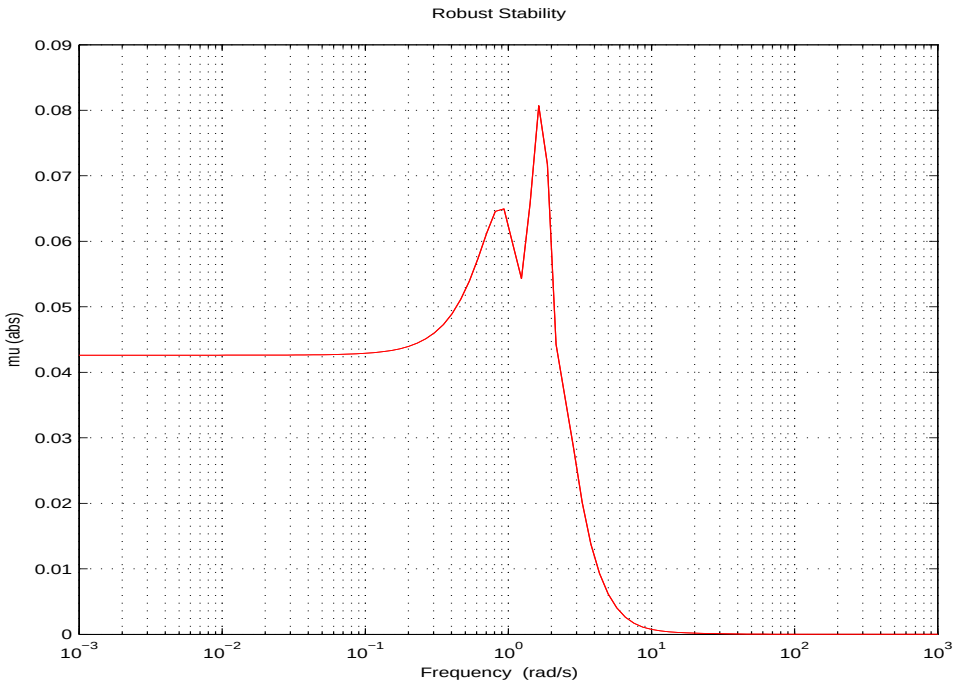

Figure 6.10: Robust stability.

used. In addition, as mentioned in 6.2.2, the requirement of RP can be mathematically determined through the computation of the structured singular value of the matrix N with an augmented uncertainty block $\tilde{\Delta}$. Similarly to the RS case, our conclusions regarding RP are drawn from the computation of the lower and the upper bound of the structured singular value $\mu_{\tilde{\Delta}}$. As can be seen from Fig. 6.11 the robust performance requirement is not satisfied.

In order to analyse thoroughly the system in terms of robust performance the system degradation curve is considered in Fig. 6.12. The performance degradation curve is graphical representation the value of the $\|F_{zw}(\Delta)\|_\infty$, which is the norm of the closed loop function connecting system inputs w and system outputs z, as a function of the uncertainty magnitude $\bar{\sigma}_\Delta$. It can be observed that $\|F_{zw}(\Delta)\|_\infty$ is a monotonically increasing function of $\bar{\sigma}_\Delta$ and at a certain magnitude of the uncertain elements $\bar{\sigma}_\Delta$, the gain becomes infinite and the system losses its stability. The point where this happens is the robust stability margin which has also been specified at the previous subsection.

Additionally, the blue line corresponds to points with the property $\bar{\sigma}_\Delta \cdot \|F_{zw}(\Delta)\|_\infty = 1$. Thus, these points lie in the margin of the acceptable robust performance. The intersection between the performance degradation curve-red line and the blue line correspond to the maximum allowed uncertainty magnitude for marginally acceptable robust performance. In other words, from the definition of μ, the point of intersection between the two lines has x-coordinate the reciprocal of the term $\gamma = max\{\mu_{\tilde{\Delta}}\} = 1.3657$ and $max\{\bar{\sigma}_\Delta\} = 0.7322$. This means that robust performance is guranteed for all the uncertain blocks with magnitude less than 0.7322.

An additional useful information is the sensitivity of the performance margin with

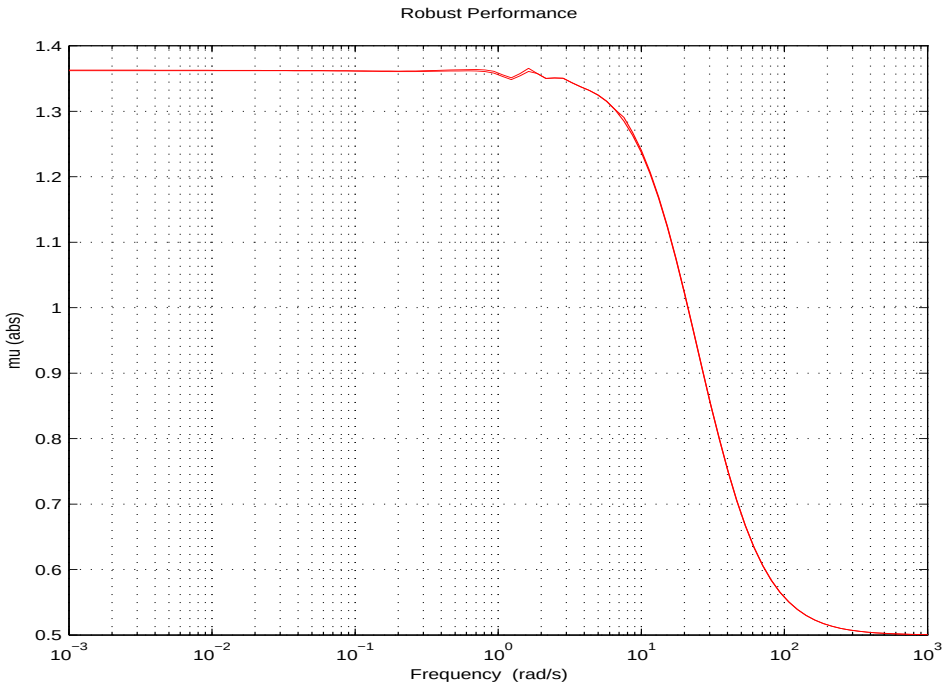

Figure 6.11: Robust performance.

respect to changes in the magnitude of the uncertain elements. Using Matlab Robust Control Toolbox it is possible to obtain that an increase in the magnitude of Δ_G by 25% leads to an decrease in performance "margin" by 1% while an increase in the magnitude of Δ_{G_d} by 25% leads to an decrease in performance "margin" by 4%. Therefore, the effect of the uncertain block $\Delta_{G,d}$ greatly determines performance margin.

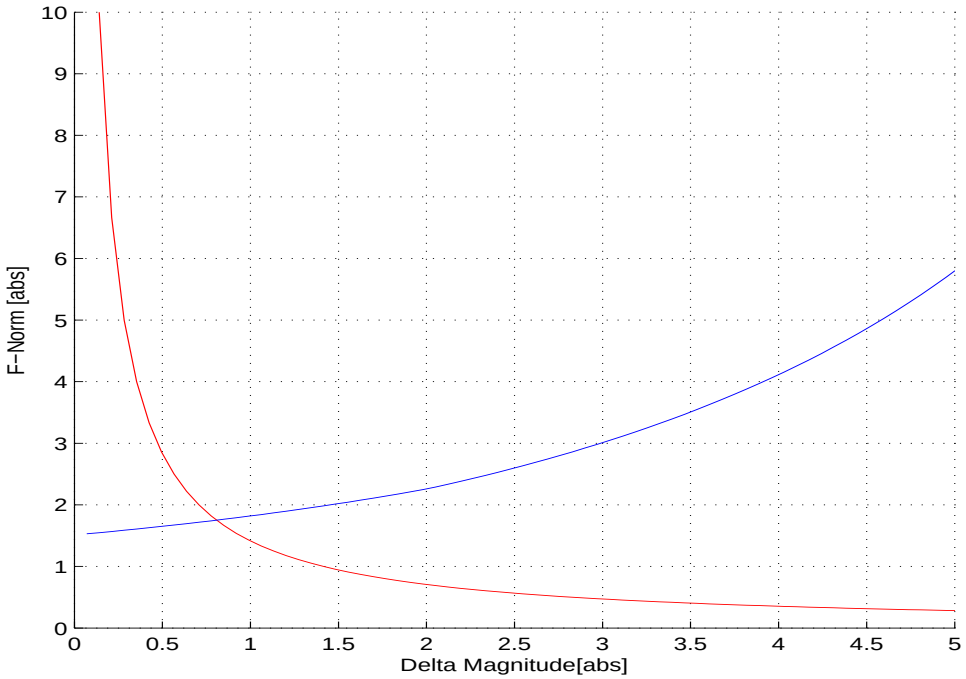

Figure 6.12: Performance degradation curve.

Chapter 7

Experimental Results

This chapter is dedicated to the experimental validation of the controller in the hybrid-electric testbed facility at the LME. The controller stability and performance is evaluated under the presence of exogenous torque disturbances. The results which are illustrated in this chapter aim to verify the soundness of the choice of λ as a controlled variable for emissions reduction and the suitability of the λ estimate provided by the virtual sensor.

7.1 Experiment I

In this experiment the controller designed in Chap. 6, for the plant of Sec. 5.8, is tested; the feedback signal is provided from the virtual sensor.

Initially, the engine operated at 1600 RPM producing 300 Nm torque and when all transient phenomena had declined the required load from the water brake switched from 300 Nm to 400 Nm. Enough time was given until a new equilibrium operating point had been reached and the additional 100 Nm load was removed. The aforementioned process was repeated for a load change from 300 Nm to 500 Nm and the response of the ICE was recorded. The requested torque along with the torque produced by the ICE and the EM are depicted in Fig. 7.1

It can be observed from Fig. 7.2 (top plot) that apart from a relatively small error between the simulated and the estimated on-line value of λ-as obtained from the virtual sensor- during the initial transient phenomenon, the results of the simulation closely match those of the experiment.

In Fig. 7.2 (bottom plot) it is depicted that the measured command of the controller is smooth but simultaneously relatively sluggish. Regarding the comparison between the simulated and the measured command it can be stated that the variations of the measured command are reproduced from the model proposed. However, a steady state deviation between the simulated and the measured command is presented in the first step load.

Figure 7.4 (bottom plot) presents the value of λ as measured from the physical sensor. Observing this figure it is can be deduced that NO_x display a similar dynamic behaviour to the inverse of λ. Unlike NO_x and λ, noise induced bias is presented in the measurement of opacity due to the analogue nature of this sensor. Additionally, the opacity measurement is delayed by approximately 7 sec compared to NO_x and λ.

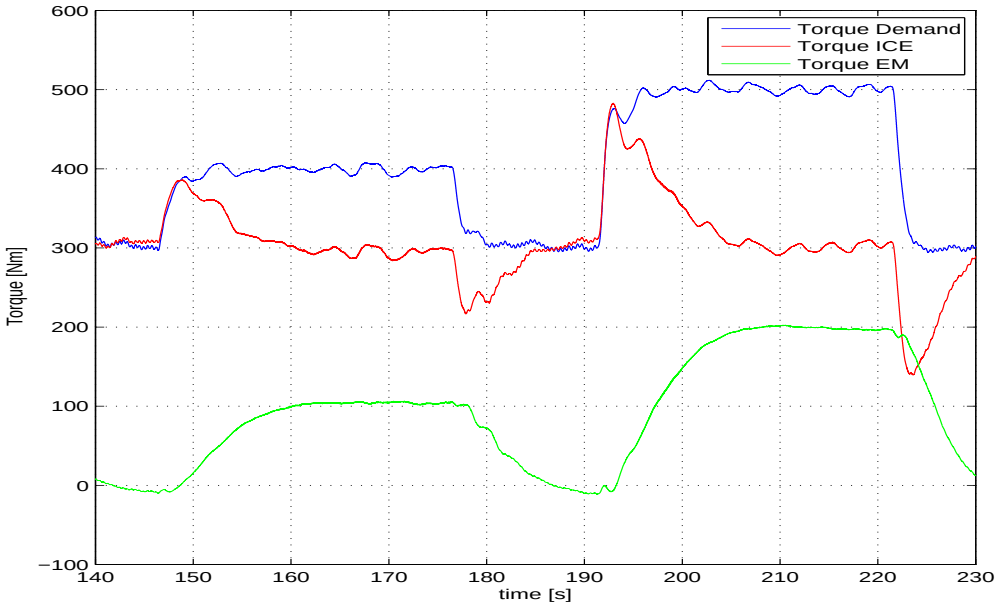

Figure 7.1: Exp I: Toque demand and produced torque by the ICE and EM.

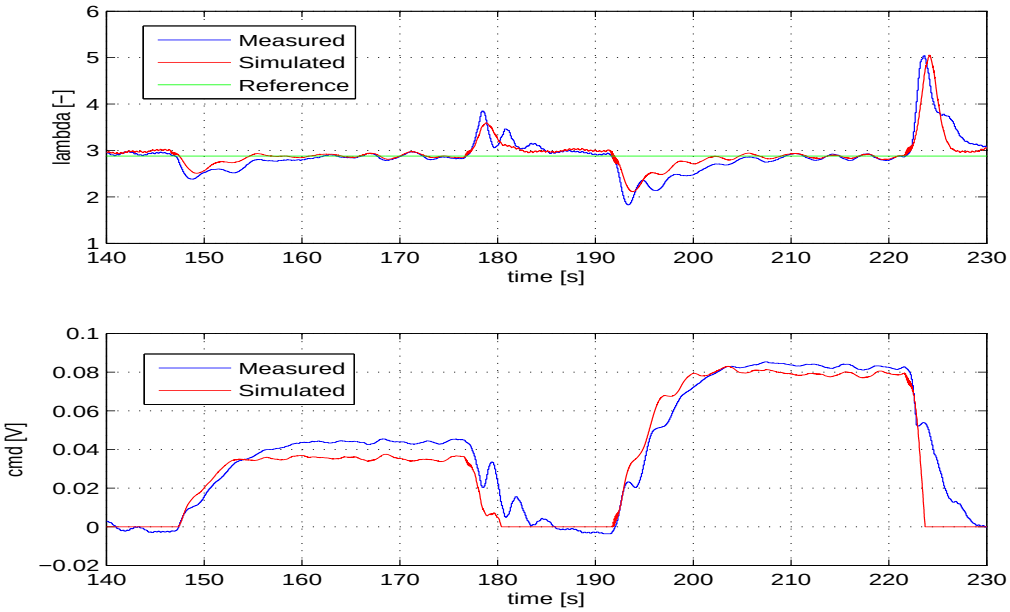

Figure 7.2: Exp I: Top: Simulated and on-line computed lambda from the virtual sensor. Bottom: Simulated and measured controller command.

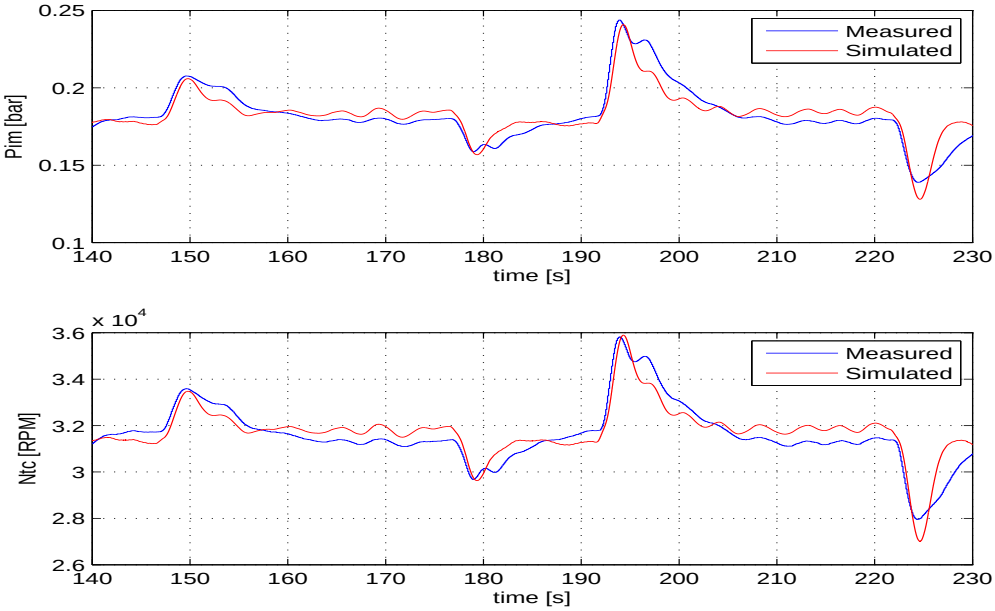

Figure 7.3: Exp I: Top: Simulated and measured pressure in the intake manifold-p_{im}. Bottom: Simulated and measured turbocharger speed-N_{tc}.

7.2 Experiment II

For the second experiment all the operating conditions were as in Experiment I with the only difference that the robust controller was fed with the measured λ of the physical sensor.

For this trial, the results of the simulation are not presented, since the proposed model of Chap. 3 is obtained in order to reproduce the dynamic behaviour of the virtual sensor and not this of the physical sensor. A model of the physical sensor have also to reproduce the transient operation of the ICE during load reductions and include the delay of the measurement due to the exhaust duct length as well as the dynamics associated with the measuring device.

It can be seen from Fig. 7.5 that the command to the frequency inverter of the EM is not smooth and noticeable sharp variations are presented. This result verifies that the undesirable oscillatory behaviour in the controller command is reduced with the virtual sensor implementation.

Moreover, as depicted in Fig. 7.6 no deterioration in the emissions reduction is expected, according to the experimental results, from the replacement of the physical with the virtual sensor. At the same time, opacity experiences a less sharp rise during the second load transient and the variations of λ decline faster when the feedback is provided by the virtual sensor.

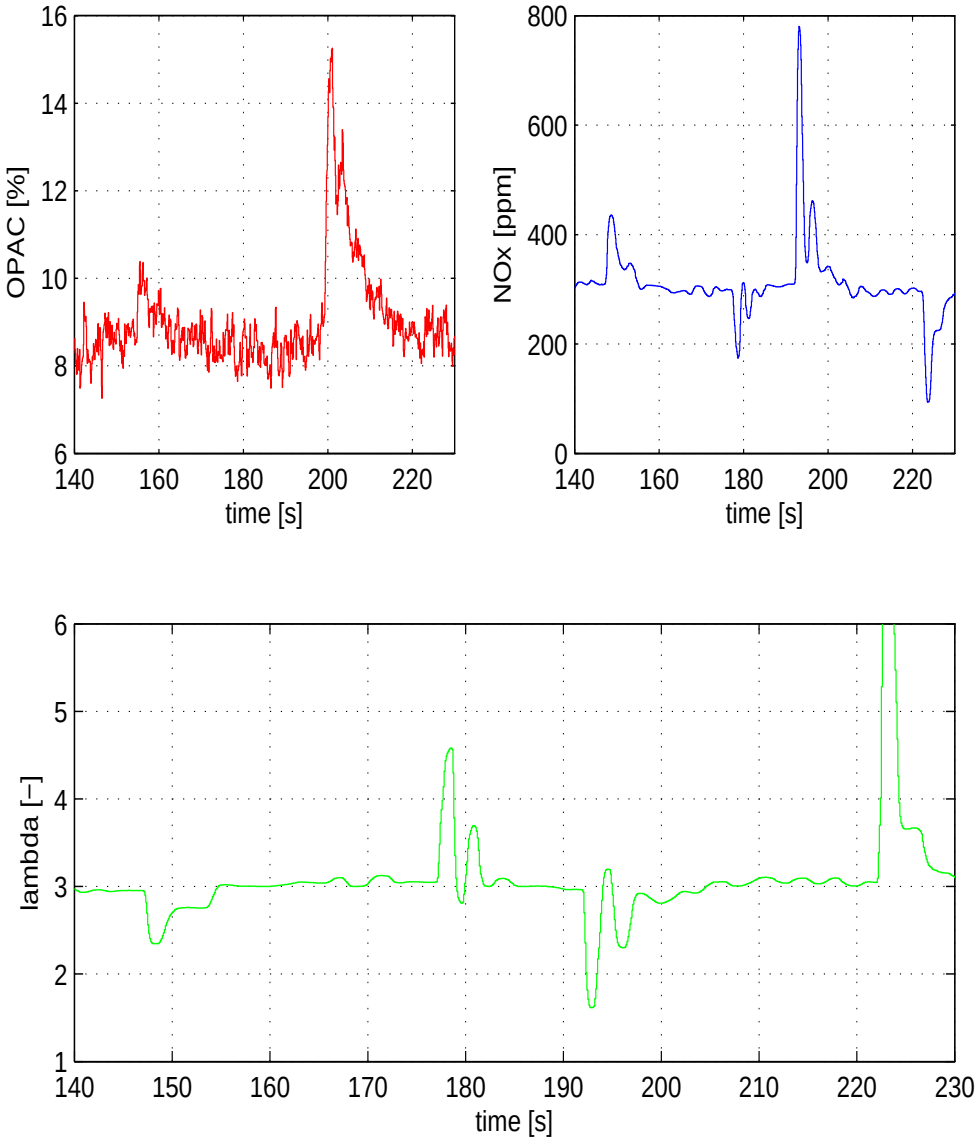

Figure 7.4: Exp I: Top: Opacity and NO_x. Bottom: Lambda as measured from the physical sensor.

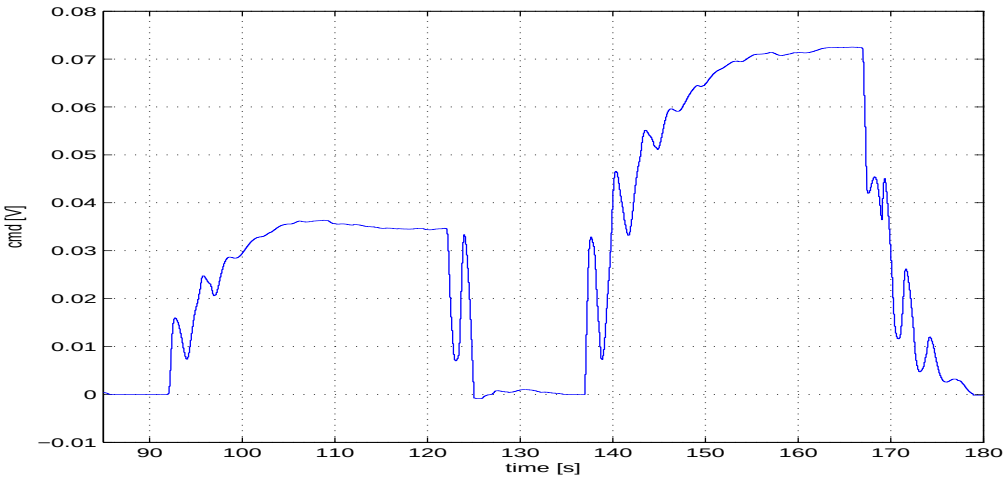

Figure 7.5: Exp II: Controller command with feedback provided by the physical sensor.

7.3 Experiment III

In the final experiment that was carried out in the LME the objective was the investigation of the results obtained in Sec. 5.6 and the parameters of the testing were identical to those of Experiment I with the only difference that the shaft speed was 1500 RPM.

The results obtained provided a sound verification of the theory developed in Sec. 5.6. Precisely, the controller derived for 1500 RPM shaft speed demonstrated substantial oscillatory behaviour for the second step load as can be seen from Fig. 7.7. This phenomenon can neither be attributed to the torque demand which was the same for both the Experiment I and Experiment II nor to the accuracy of the proposed dynamic non-linear model that seems to reproduce the experimental results as shown in Fig. 7.8.

The measured pollutant emissions along with the value of λ as provided by the physical sensor are depicted in Fig. 7.9.

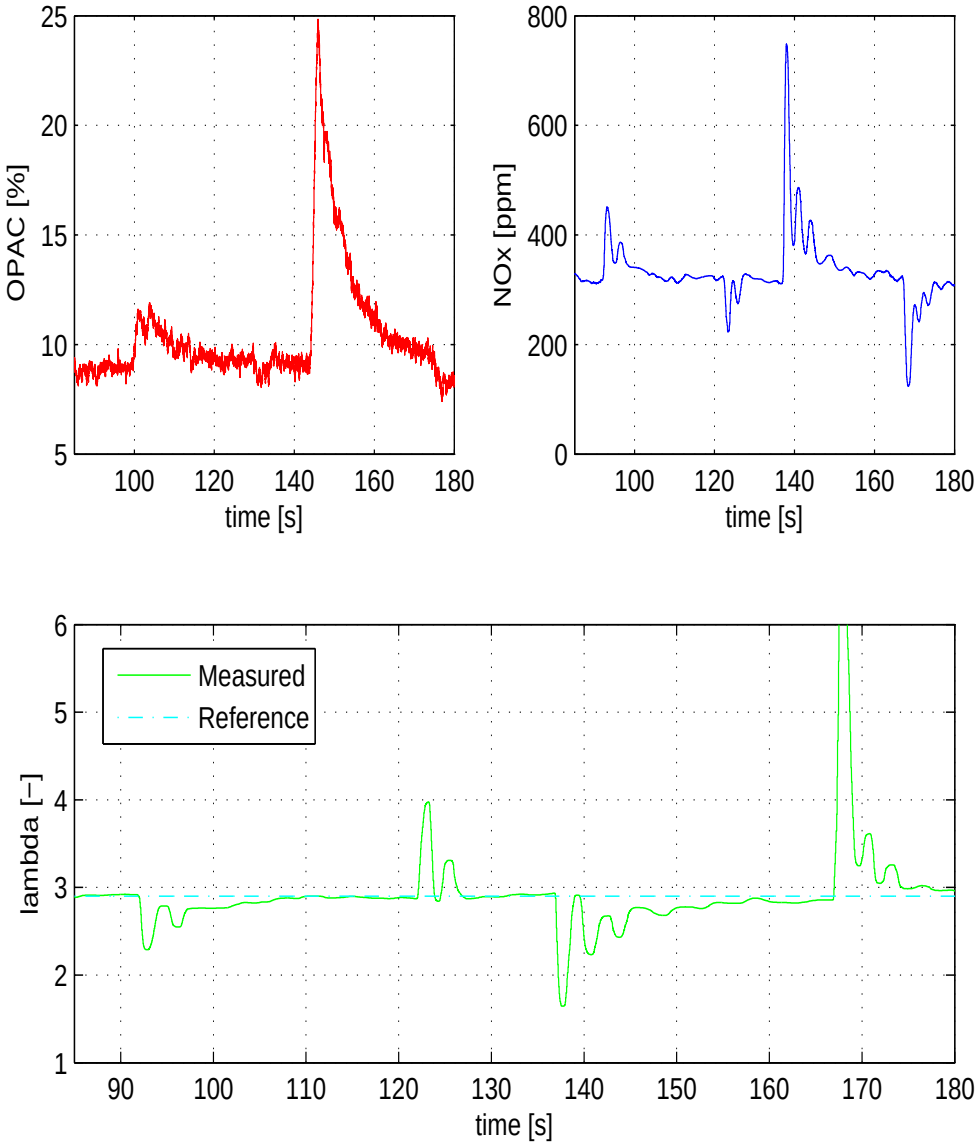

Figure 7.6: Exp II: Top: Opacity and NO_x. Bottom: Lambda as measured from the physical sensor.

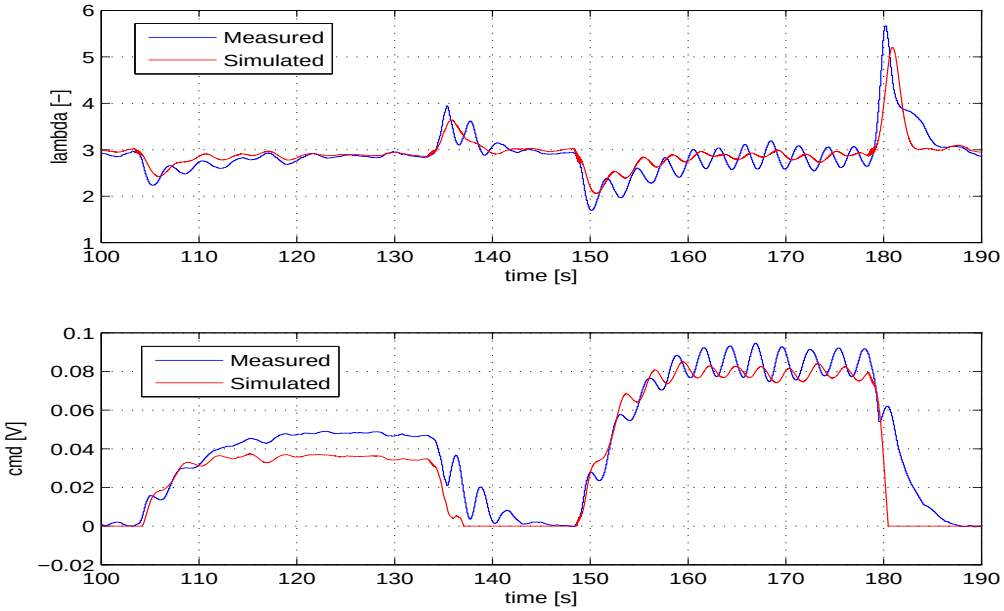

Figure 7.7: Exp III: Top: Simulated and on-line computed lambda from the virtual sensor. Bottom: Simulated and measured controller command.

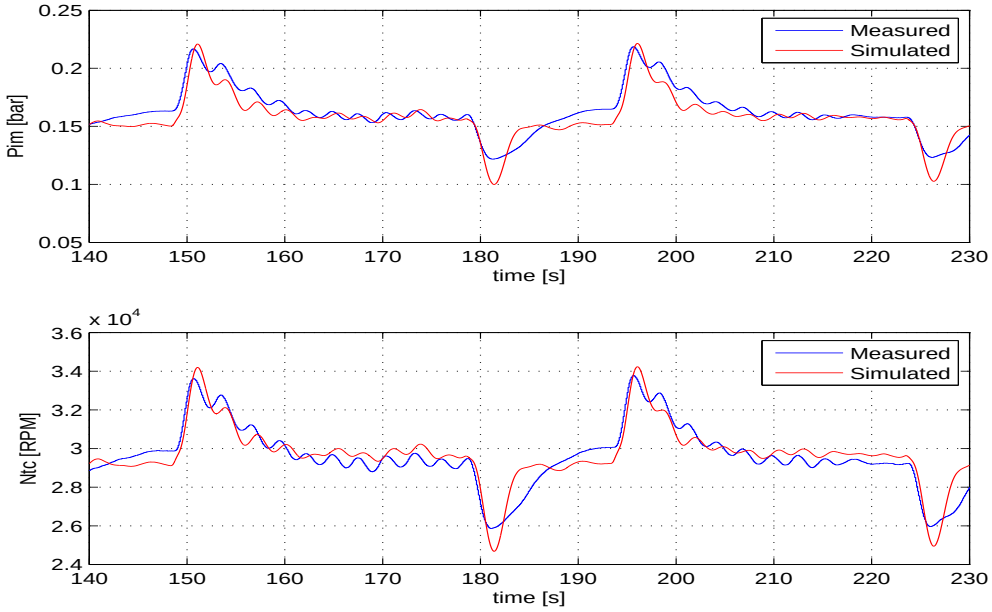

Figure 7.8: Exp III: Top: Simulated and measured pressure in the intake manifold-p_{im}. Bottom: Simulated and measured turbocharger speed-N_{tc}.

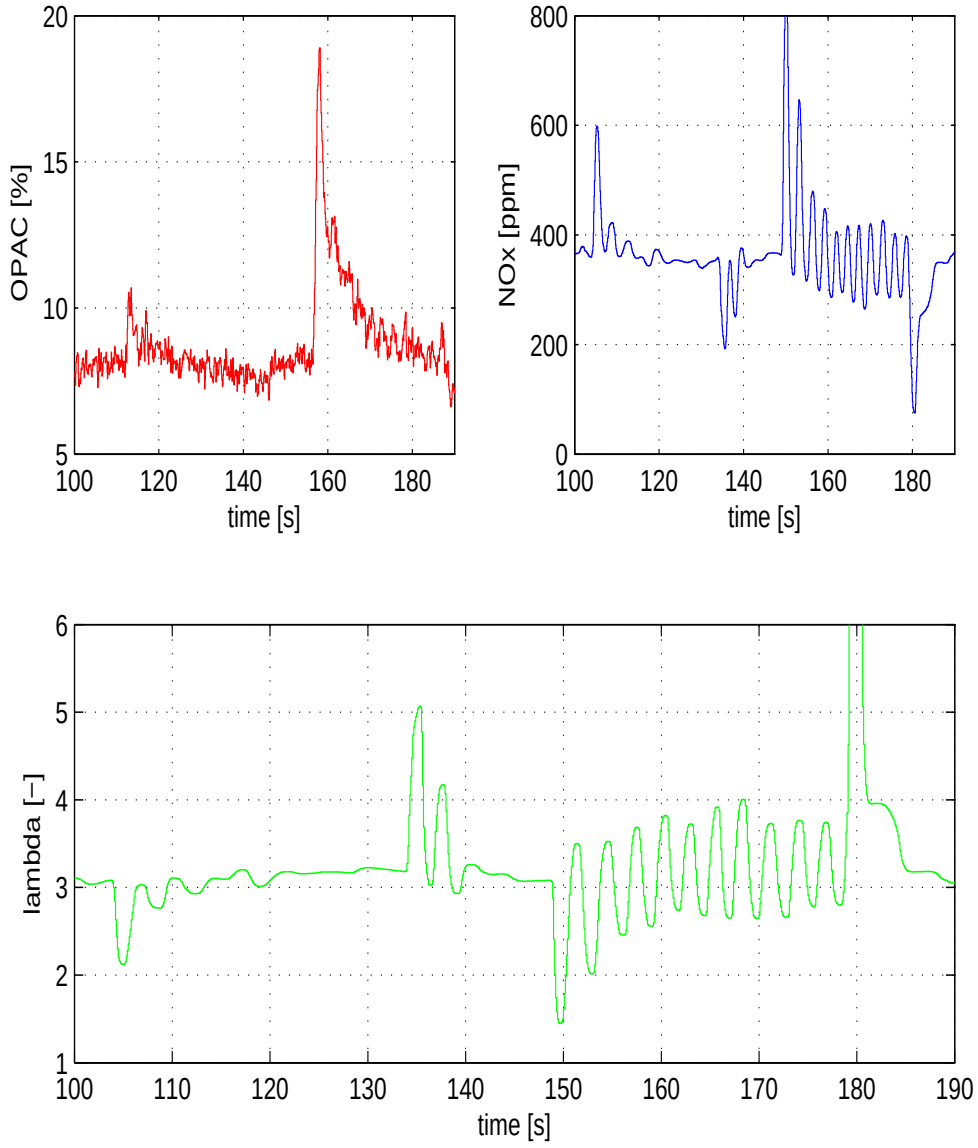

Figure 7.9: Exp III: Top: Opacity and NO_x. Bottom: Lambda as measured from the physical sensor.

Chapter 8

Conclusions and Future Work

8.1 Conclusions

In order to meat the continuously tightening emission standards imposed by legislation authorities on sea-going vessels, a closed-loop control of the main pollutants emissions of a hybrid-electric marine powertrain is proposed. As a first step towards emission reduction in hybrid-electric marine plants, the feasibility of controlling the value of lambda of the exhaust gas only by manipulating the torque produced by the electric motor was examined. The experimental results obtained were satisfactory and verified the soundness of the proposed concept of emission reduction technique in practice.

In fact, the controller, tested under the presence of exogenous disturbances, demonstrated its ability to reduce NO_x and particulate matter (PM) that were emitted by the internal combustion engine in transient loading and verified the choice of lambda as feedback signal. The controller functioned more stable and smooth when the feedback was provided by the virtual sensor compared to the operation with feedback provided by the physical sensor. At the same time, considering the limited availability of the torque measurement as input signal in marine applications, a virtual sensor that made use only of the turbocharger speed was obtained; thus, the applicability of this method in standard-marine plants is widened. Finally, the results from the operation of the experimental plant in the low speed region were useful in developing confidence to the proposed first order transfer function in terms of predicting the operation of the hybrid-electric powertrain in various operating points.

8.2 Future Work

Quasi-Static Optimization Algorithm

An assumption was made in Chap. 6 that the reference value of λ was provided by a high level quasi-static optimization algorithm. On the grounds that only the transient behaviour of the ICE was treated in this thesis, a potential subject of further research could be the optimal energy management of hybrid-electric marine powertrains in steady state condition. Towards this direction, the non-linear dynamic λ-model derived in Chap. 3 could be valuable.

Moreover, the value of λ derived from the dynamic model can also be the input to quasi-static maps in order to obtain PM and NO_x. In this way, knowledge can be

gained about the pollutant emissions of the ICE as a function of the operating point. An additional characteristic variable linked to the battery state of energy/state of charge (SOE/SOC) or a metric of the electric energy consumption has to be developed to make feasible the static energy management of the hybrid power-train.

Finally, the feasibility of the implementation of various energy management algorithms in hybrid-electric marine propulsion plants, currently adopted in automotive powetrains, has to be thoroughly examined. Although fundamental difficulties are presented in this direction, like the lack of knowledge of the exact vessel's load profile and the the absence of energy recovery system during deceleration of the vessel, the present thesis demonstrated that certain benefits associated with emission reduction do exist from the use of hybrid-electric propulsion in marine applications.

Robust Adaptive Controller

In Chap. 5 a first order transfer function $G_{\dot{m}_f \to \lambda}$ was obtained and its parameters were presented in 2D maps as a function of the operating point of the ICE. The variation in the dynamic behaviour of the transfer function when the operating point shifted from the nominal was taken into consideration as uncertainty in modelling and a controller was implemented for the uncertain transfer function.

However, implementing a μ-controller for a wide operating range comes at the expense of a wide uncertainty region in the plant model and of poor performance characteristics. Instead of developing a μ-controller, a robust adaptive controller and identifier can be designed in order to obtain on-line the transfer function and the controller of the plant. In this way the proposed design will be less conservative compared to the μ-controller.

Alternative Fuel Mass Flow Estimation Techniques

The performance of the second virtual sensor derived in Sec. 4.5, which has as single input the turbocharger speed, was not examined on-line. Thus, a possible direction of further research may be the evaluation of the performance of this virtual sensor in λ control applications.

Furthermore, the simulation results of Sec. 4.5 demonstrated slow response of the virtual sensor. The reason for this slow response lies in the fact that fuel mass flow is estimated only from the air path data. The feasibility of another approach of obtaining a fast and accurate fuel flow estimate should be investigated.

Another subject of future work may be the study of a design that integrates both the virtual and the physical sensor. The former will provide an accurate estimate of λ during the initial transient phenomenon while the steady state value of λ will be obtained from the latter sensor.

Multivariable Feedback Control

In the present thesis the controlled variable-λ is manipulated only by the input command that is provided to the frequency inverter of the electric motor. This approach imposes fundamental limitations in the performance that could be achieved and the corresponding emission reduction. Precisely, the electric motor dynamics limit the rate with which the pollutant emissions are reduced during load transients.

If access to the fuel injection command is provided, the response of the internal combustion engine will be substantially improved with λ experience a less sharp drop during load transients. Towards this direction, increasing the degrees of freedom in the powertrain through additional input variables could augments the effectiveness of control. Another benefit that is provided by multiple input variables is the possibility to control more accurately several output signals such as NO_x and λ instead of a single one.

Bibliography

[1] E. Alfiery. *Emissions-Controlled Diesel Engine*. PhD thesis, Swiss Federal Institute of Technology Zurich, 2009.

[2] B. Amin. *Induction Motors, Analysis and Torque Control*. Springer, 2001.

[3] K. J. Astrom and P. Eykhoff. System identification-a survey. *Automatica*, 7:123–162, 1971.

[4] G. J. Balas, J. C. Doyle, K. Glover, A. Packard, and R. Smith. *μ-Analysis and Synthesis Toolbox*, June 1998.

[5] B. M. Baumann, G. N. Washington, B. C. Glenn, and G. Rizzoni. Mechatronic design and control of hybrid electric vehicles. *IEEE/ASME Trans. on Mechatronics*, 5:58–72, 2000.

[6] B. Botha and A. Moolman. Determining the impact of the different losses on centrifugal compressor design. *The SA Mechanical Engineer*, 2005.

[7] S. Dixon. *Fluid Mechanics and Thermodynamics of Turbomachinery*. Elsevier, 5th edition, 1978.

[8] L. Eriksson, L. Nielsen, J. Brugard, J. Bergstrom, F. Pettersson, and P. Andersson. Modeling of a turbocharged si engine. *Annual Reviews in Control*, 26:129–137, 2001.

[9] G. Ripaccioli et al. An application to hybrid electric vehicle energy management. In *Proceeding of the 12th International Conference on Hybrid Systems Computation and Control (HSCC 2009)*, volume 5469, pages 321–335. Springer-Verlag, April 2009.

[10] S. Fekri and F. Assadian. The role and use of robust multivariable control in hybrid electric vehicle energy management. In *2012 IEEE International Conference on Control Applications (CCA)*, October 2012.

[11] J. T. Gravdahl and O. Egeland. Centrifugal compressor surge and speed control. *IEEE Transactions on Control Systems Technology*, 7:567–579, September 1999.

[12] D. W. Gu, P. H. Petkov, and M. M. Konstantinov. *Robust Control Design with MATLAB*. Springer, 2nd edition, 2013.

[13] L. Guzzella and C. Onder. *Introduction to Modeling and Control of Internal Combustion Engine Systems*. Springer, London, 2nd edition, 2004.

[14] J. Heywood. *Internal Combustion Engine Fundamentals*. McGraw-Hill, 1998.

[15] D. Hountalas. Prediction of marine diesel engine performance under fault conditions. *Applied Thermal Engineering*, 20:1753–1783, 2000.

[16] P. Ioannou and J. Sun. *Robust Adaptive Control*. Dover Publications, 2012.

[17] A. T. Karlsen. On modeling of a ship propulsion system for control purposes. Master's thesis, Norwegian University of Science and Technology, June 2012.

[18] P. Kokotovic, R. Omalley, and P. Sannuti. Singular perturbations and order reduction in control theory-an overview. *Automatica*, 12:123–132, 1976.

[19] I. Kolmanovsky, I. Siverguina, and J. L. Stein. Optimization of powertrain operating policy for feasibility assessment and calibration: Stochastic dynamic programming approach. In *Proceedings of the 2002 American Control Conference*, volume 2, pages 1425–1430, May 2002.

[20] C. C. Lin, J. M. Kang, J. W. Grizzle, and H. Peng. Energy management strategy for parallel hybrid electric truck. In *Proceedings of the American Control Conference*, pages 2878–2883, 2001.

[21] C. C. Lin, H. Peng, and J. W. Grizzle. A stohastic control stategy for hybrid electirc vehicles. volume 5, pages 4710–4715, 2004.

[22] L. Ljung. *System Identification, Theory for the User*. Prentice Hall, Upper Saddle River, NJ, 2nd edition, 1999.

[23] L. Ljung. Perspectives on system identification. In *In Plenary talk at the proceedings of the 17th IFAC World Congress, Seoul, South Korea*, 2008.

[24] L. Ljung. Experiments with identification of continuous time models. In *15th IFAC Symposium on System Identification, Saint-Malo, France*, May 2009.

[25] L. Ljung. *System Identification Toolbox*, September 2015.

[26] J. Lygeros and F. Ramponi. *Lecture Notes on Linear System Theory*. Janury 2015.

[27] A. Martyr and M. Plint. *Engine Testing: Theory and Practice*. Butterworth-Heinemann, 3rd edition, 2007.

[28] P. Moraal and I. Kolmanovsky. Turbocharger modeling for automotive control applications. *SAE TECHINCAL PAPER SERIES*, (1999-01-0908), 1999.

[29] P. Moulin, J. Chauvin, and B. Youssef. Modelling and control of the air system of a turbocharged gasoline engine. In *Proceedings of the 17th Word Congress*, volume 17, pages 8487–8494. International Federation of Automatic Control, July 2008.

[30] M. Salman N. Schouten and N. Kheir. Control strategies for parallel hybrid vehicles. 10:460–468, 2002.

[31] P. Pisu, K. Koprubasi, and G. Rizzoni. Energy management and drivability control problems for hybrid electric vehicles. In *44th IEEE Conference on Decision and Control and 2005 European Control Conference*, pages 1824–1830, December 2005.

[32] P. Pisu and G. Rizzoni. h_∞ control for hybrid electric vehicles. In *43rd IEEE Conference on Decision and Control*, volume 4, pages 3497–3502, December 2004.

[33] C. Rakopoulos and E. Giakoumis. Review of thermodynamic diesel engine simulations under transient operating conditions. *SAE 2006 Transactions Journal of Engines*, (2006-01-0884), 2006.

[34] C. Rakopoulos and E. Giakoumis. *Diesel Engine Transient Operation, Principles of Operation and Simulation Analysis*. Springer, London, 2009.

[35] M. Ramsbottom and F. Assadian. Use of approximate dynamic programming for the control of a mild hybrid. In *Proceedings of WMG Hybrid Conference*, December 2006.

[36] G. Rizzoni, L. Guzzella, and B. Baumann. Unified modeling of hybrid electric vehicle drivetrains. *IEEE/ASME Transactions on Mechatronics*, 4:246–257, September 1999.

[37] D. B. Rodriguez. *Modelling and Observation of Exhaust Gas Consentrations for Diesel Engine*. Springer, 2014.

[38] M. Salman, N. J. Schouten, and N. A. Kheir. Control strategies for parallel hybrid vehicles. In *Proceedings of the American Control Conference*, volume 1, pages 524–528, 2000.

[39] A. Sasane. *Hankel Norm Approximation for Infinite-Dimensional Systems*. Springer, 2002.

[40] A. Sciarretta and L. Guzzella. Control of hybrid electric vehicles. pages 60–70, April 2007.

[41] W. Shepherd, L. N. Hulley, and D. T. W. Liang. *Power Electronics and Motor Control*. Cambridge University Press, 2nd edition, 1995.

[42] S. Skogestad and I. Postlethwaite. *Multivariable Feedback Control Analysis and deisgn*. John Wiley and Sons, 2nd edition, 2005.

[43] A. Stefanopoulou and R. Smith. Maneuverability and smoke emission contraints in marine diesel propulsion. *Control Engineering Practice*, pages 1023–1031, 2000.

[44] O. Storset, A. Stefanopoulou, and R. Smith. Adaptive air charge estimation for turbocharged diesel engines without exhaust gas recirculation. *IEEE/ASME Journal of Dynamic Systems, Measurement, and Control*, 126, 2003.

[45] C. F. Taylor. *The Internal Combustion Engine in Theory and Practice*, volume I, Thermodynamics, Fluid Flow, Performance. The M.I.T. Press, 2nd edition, 2004.

[46] T.E.Passenbrunner, M.Sassano, H.Trogmann, L.del Re, M.Paulweber, M.Schmidt, and H.Koka. Inverse torque control of hydrodynamic dynamometers for combustion engine test benches. In *American Control Conference*, pages 4598–4603. IEEE, June 2011.

[47] J. Wahlstrom and L. Eriksson. Modelling diesel engines with a variable-geometry turbocharger and exhaust gas recirculation by optimization of model parameters for capturing non-linear system dynamics. *Proceedings of the Institution of mechanical engineers*, 2011.

[48] J. Wahlstrom, N. Karvosenoja, and P. Porvari. Ship emissions and technical emission reduction potential in the nothern baltic sea. Technical report, Finnish Environment Institute, 2006.

[49] K. Zhou and J. Doyle. *Essentials of Robust Control*. Prentice Hall, 1999.

[50] Y. Zhu. *Multivariable System Identification for Process Control*. Pergamon, 1st edition, 2001.